

UNIVERSITY OF TRENTO - Italy
Department of Civil, Environmental
and Mechanical Engineering



Doctoral School in Civil, Environmental and Mechanical Engineering
Topic 3. Modelling and Simulation - XXXI cycle 2016/2019

Doctoral Thesis - May 2019

Roberto Guarino

Modelling and Simulation in Tribology of Complex Interfaces

Supervisors

Prof. Nicola Pugno, University of Trento
Dr. Ivano Furlan, Bonfiglioli Riduttori SpA

Cover image: graphical abstract of the Doctoral Thesis.
© 2019 Roberto Guarino. All rights reserved.



Except for the parts already published by other publishers, contents on this book are licensed under a Creative Commons Attribution - Non Commercial - No Derivatives 4.0 International License

University of Trento
Doctoral School in Civil, Environmental and Mechanical Engineering
<http://web.unitn.it/en/dricam>
Via Mesiano 77, I-38123 Trento
Tel. +39 0461 282670 / 2611 - dicamphd@unitn.it

to my wife Adele

Acknowledgements

The work carried out during the Doctoral Course has received funding from Bonfiglioli Riduttori SpA, which is gratefully acknowledged.

The author also acknowledges the organisers of the Lorenz Workshop "Micro/Nanoscale Models for Tribology" (Leiden, The Netherlands, 2017) from which part of Chapter 2 has been derived; Prof. J.F. Molinari (EPFL, Switzerland) for discussion on third-body friction; all the coauthors of the publications related to Chapters 3, 5 and 6; Oerlikon Balzers Coating Italy SpA for providing the carbon-coated samples described in Appendix E and Stefania Forleo, Massimo Colliva and Salvatore Terranova (Bonfiglioli Riduttori SpA) for related discussion and the optical microscopy activities.

The author is also extremely grateful to all his friends met in Trento, Italy, during the last years, and his family for the constant support.

Abstract

Tribology is known as the science of surfaces in relative motion and involves complex interactions over multiple length and time scales. Therefore, friction, lubrication and wear of materials are intrinsically highly multiphysics and multiscale phenomena. Several modelling and simulation tools have been developed in the last decades, always requiring a trade-off between the available computational power and the accurate replication of the experimental results. Despite nowadays it is possible to model with extreme precision elastic problems at various scales, further efforts are needed for taking into account phenomena like plasticity, adhesion, wear, third-body friction and boundary and solid lubrication. The situation becomes even more challenging if considering non-conventional nano-, as in the case of polymer surfaces and interfaces, or microstructures, as for the hierarchical organisations observed in biological systems.

Specifically, biological surface structures have been demonstrated to present exceptional tribological properties, for instance in terms of adhesion (e.g., the gecko pad), superhydrophobicity (e.g., the lotus leaf) or fluid-dynamic drag reduction (e.g., the shark skin). This has suggested the study and development of hierarchical and/or bio-inspired structures for applications in

tribology.

Therefore, by taking inspiration from Nature, we investigate the effect of property gradients on the frictional behaviour of sliding interfaces, considering lateral variations in surface and bulk properties. 3D finite-element simulations are compared with a 2D spring-block model to show how lateral gradients can be used to tune the macroscopic coefficients of friction and control the propagation of detachment fronts.

Complex microscale phenomena govern the macroscopic behaviour also of lubricated contacts. An example is represented by solid lubrication or third-body friction, which we study with 3D discrete-element simulations. We show the effects of surface waviness and of the modelling parameters on the macroscopic coefficient of friction.

Many other natural systems present complex interfacial interactions and tribological behaviour. Plant roots, for instance, display optimised performance during the frictional penetration of soil, especially thanks to a particular apex morphology. Starting from experimental investigations of different probe geometries, we employ the discrete-element method to compute the expended work during the penetration of a granular packing, confirming the optimal bio-inspired shape. This has allowed to follow also an integrated approach including image acquisition and processing of the actual geometries, 3D printing, experiments and numerical simulations.

Finally, another interesting example of advanced biological interface with optimised behaviour is represented by biosensing struc-

tures. We employ fluid-structure interaction numerical simulations for studying the response of spiders' trichobothria, which are among the most sensitive biosensors in Nature. Our results highlight the role of the fluid-dynamic drag on the system performance and allow to determine the optimal hair density observed experimentally.

Both the third-body problem and the possibility to tune the frictional properties can be considered as the next grand challenges in tribology, which is going to live a "golden age" in the coming years. We believe the results discussed in this Doctoral Thesis could pave the way towards the design of novel bio-inspired structures with optimal tribological properties, for the future development of smart materials and innovative solutions for sliding interfaces.

List of publications

This Doctoral Thesis is based on the adaptation of the results reported in the following publications:

- Vakis A.I., Yastrebov V.A., Scheibert J., Nicola L., Dini D., Minfray C., Almqvist A., Paggi M., Lee S., Limbert G., Molinari J.F., Anciaux G., Aghababaei R., Echeverri Restrepo S., Papangelo A., Cammarata A., Nicolini P., Putignano C., Carbone G., Stupkiewicz S., Lengiewicz J., Costagliola G., Bosia F., Guarino R., Pugno N.M. Müser M.H., Ciavarella M. Modeling and simulation in tribology across scales: An overview. *Tribology International* **125** (2018) 169-199.
doi.org/10.1016/j.triboint.2018.02.005
- Guarino R., Costagliola G., Bosia F., Pugno N.M. Evidence of friction reduction in laterally graded materials. *Beilstein Journal of Nanotechnology* **9** (2018) 2443-2456.
doi.org/10.3762/bjnano.9.229
- Mishra A.K., Tramacere F., Guarino R., Pugno N.M., Mazzolai B. A study on plant root apex morphology as a model for soft robots moving in soil. *PLoS ONE* **13** (2018) e0197411.
doi.org/10.1371/journal.pone.0197411
- Guarino R., Greco G., Mazzolai B., Pugno N.M. Fluid-structure interaction study of spider's hair flow-sensing system. *Materials Today: Proceedings* **7** (2019) 418-425.
doi.org/10.1016/j.matpr.2018.11.104

Additional results of the Doctoral Course are reported in the following publications:

- Guarino R., Goffredo S., Falini G., Pugno N.M. Mechanical properties of *Chamelea gallina* shells at different latitudes. *Journal of the Mechanical Behavior of Biomedical Materials* **94** (2019) 155-163.
doi.org/10.1016/j.jmbbm.2019.02.032
- Papangelo A., Guarino R., Pugno N.M., Ciavarella M. On unified crack propagation laws. *Engineering Fracture Mechanics* **207** (2019) 269-276.
doi.org/10.1016/j.engfracmech.2018.12.023

Contents

Acknowledgements	vi
Abstract	x
List of publications	xii
1 Introduction	1
2 Modelling and simulation in tribology	5
2.1 Introduction	5
2.2 Dry friction	11
2.2.1 Finite and boundary-element simulations	11
2.2.2 Friction between patterned surfaces	15
2.3 Fluid and solid lubrication	18
2.3.1 Literature review	18
2.3.2 Simulation methods	21
2.4 Diffusion at polymer interfaces	23
2.4.1 Adhesion phenomena	23
2.4.2 Polymer nanotribology	25
2.5 Conclusions	27
References	27

3 Friction between laterally graded materials	44
3.1 Introduction	44
3.2 Methods	46
3.2.1 Introduction	46
3.2.2 2D spring-block model	47
3.2.3 3D finite-element model	49
3.2.4 System parameters	50
3.3 Results and discussion	54
3.3.1 Gradients in the local coefficients of friction	54
3.3.2 Gradients in the material Young's modulus	60
3.4 Conclusions	65
References	67
4 Third-body friction between wavy surfaces	72
4.1 Introduction	72
4.2 Methods	74
4.2.1 The discrete element method	74
4.2.2 Modelling details	75
4.2.3 Geometry and extraction of the coefficient of friction	76
4.3 Results and discussion	79
4.3.1 Forces and kinetic energies	79
4.3.2 Reference simulation case	83
4.3.3 Effect of operational conditions	87
4.3.4 Effect of contact parameters	91
4.4 Conclusions	91
References	93

5	Frictional penetration in granular media	96
5.1	Introduction	96
5.2	Methods	99
5.2.1	Gross morphology of a plant root	99
5.2.2	Seed germination and microscope analysis	101
5.2.3	Morphometric analysis	101
5.2.4	Design and 3D printing of probes	102
5.2.5	Penetration experiments	104
5.2.6	Numerical simulations	105
5.3	Results and discussion	108
5.3.1	Experimental penetration curves	108
5.3.2	Numerical penetration curves	109
5.3.3	Additional comments	111
5.4	Conclusions	113
	References	114
6	Numerical analysis and optimisation of biosensors	119
6.1	Introduction	119
6.2	Methods	121
6.2.1	Morphology and mechanical properties	121
6.2.2	Computational model	122
6.3	Results and discussion	124
6.3.1	Hair properties	124
6.3.2	Effect of a varying flow velocity	125
6.3.3	Effect of a varying hair spacing	128
6.3.4	Estimation of the optimal hair density	132
6.4	Conclusions	134
	References	134

7 Conclusions	138
References	140
A Details of sliding friction simulations	141
B Details of third-body friction simulations	144
C Details of penetration mechanics simulations	152
D Details of spider's hair properties	156
E Carbon-based coatings for industrial power transmission ap- plications	158

Chapter 1

Introduction

The main objective of this Doctoral Thesis is to discuss a set of advanced topics in tribology of complex interfaces, with a particular focus on the modelling and simulation methods employed to provide insights into the involved physical phenomena.

The first part of this Doctoral Thesis is focused on sliding friction in the presence of property gradients or third bodies. Other applications in which tribology plays an essential role, thus providing even more demanding efforts in modelling and simulation, are the penetration mechanics in granular materials and the behaviour of biosensing interfaces found in Nature, presented in the second part of this Doctoral Thesis. In all the cases, the macroscopic behaviour of the system is governed both by complex microscale interactions and by geometry.

In Chapter 2, we summarise recent advances in the area of modelling and simulation in tribology. A particular focus is posed on dry frictional systems, discussing the main modelling methods and a short review on the frictional properties of patterned surfaces, which take inspiration from Nature for offering outstanding adhesive or sliding properties. We discuss also

the main phenomena involved in fluid and solid lubrication, including more advanced themes such as surface texturing and cavitation, together with the related available simulation tools. Finally, we present a short review on the tribology of polymer surfaces and interfaces, where complex multiscale diffusion effects are the main responsible for the observed macroscopic adhesive and frictional properties. The result is a view of tribology as a highly multiphysics and multiscale domain where, despite important achievements in modelling and simulation, significant effort is still required to account for the complementary nonlinear effects of plasticity, adhesion, friction, wear, lubrication and surface chemistry in the available models.

In Chapter 3, we investigate the possibility to modify the frictional and adhesive behaviour of materials by exploiting a grading of the material properties. This takes inspiration from biological structures, whose optimised mechanical properties are obtained through complex structural organisation involving multiple constituents, functional grading and hierarchical geometrical arrangements. Therefore, we consider the frictional sliding of elastic surfaces in the presence of a spatial variation of the Young's modulus and the local friction coefficients. Using finite-element simulations and a two-dimensional spring-block model, we investigate how graded material properties affect the macroscopic frictional behaviour, in particular, static friction values and the transition from static to dynamic friction. The results suggest that the graded material properties can be exploited to reduce static friction with respect to the corresponding non-graded material and to tune it to desired values, opening possibilities for the design of bio-inspired surfaces with tailor-made tribological properties.

In Chapter 4, we carry out a systematic analysis of the effect of surface waviness on third-body friction by means of discrete-element simulations.

We interpose spherical particles between two surfaces with a sinusoidal profile, interacting through the Hertz's contact law. By varying the surface amplitude and wavelength, we fit the trend of the global dynamic coefficient of friction with laws suggested by the Prandtl-Tomlinson's model. The effects of the applied pressure and the sliding velocity, instead, can be well described by the classical Coulomb's law of friction and by a logarithmic law, respectively. In addition, we show that the main contact parameters do not affect significantly the global response of the system.

In Chapter 5, we study the penetration mechanics in granular materials of bio-inspired probes. We propose a method for translating the morphological features of *Zea mays* roots into a new design, based on image acquisition and processing, 3D printing and penetration experiments. Thus, we carry out a comparative analysis between the artificial root-like probe and probes with different tip shapes (i.e., cylindrical, conical, elliptical and parabolic) and diameters. The results show that the energy consumption and the penetration force of the bio-inspired probe are smaller with respect to the other shapes for all the diameters of the developed probes. The penetration performance of the considered tip shapes is evaluated also by means of discrete-element numerical simulations, obtaining a good agreement with the experimental results. This study can bring to breakthrough scenarios in different fields, such as soil exploration, environmental monitoring, geotechnical studies, as well as medical applications, allowing the development of innovative bio-inspired solutions for soft robotics.

In Chapter 6, we employ fluid-structure interaction numerical simulations to study the behaviour of a natural interface represented by spiders' trichobothria, which are extremely interesting for their sensing performance and are inspiring the design of novel sensors. We consider actual spider's hairs geometry and material properties. We study the effect of a varying

flow velocity on the hair response, quantified in terms of maximum displacement and maximum von Mises stress, and we build a simple analytical model to validate the numerical results. In addition, we consider the relative longitudinal and transversal position of two hairs, to verify the optimal geometry found in Nature by a simple analytical model. Our results can be of interest for the future design and development of novel bio-inspired systems and tribological interfaces for smart sensors and robotics.

Finally, in Chapter 7 we conclude this Doctoral Thesis with a brief comment on a recent paper covering the next big challenges in tribology, which is believed to be approaching its "golden age" in the coming years, thanks to the rapid advances in life sciences and in micro- and nanotechnologies. Examples of future challenging topics in tribology of complex interfaces are presented, together with an experimental investigation of high-performance carbon-based coatings for next-generation industrial power transmissions.

Chapter 2

Modelling and simulation in tribology

2.1 Introduction

The word tribology introduced in the famous Jost report of 1966 [1] was apparently coined by David Tabor and Peter Jost, derived from the root *tribo-* (Greek $\tau\rho\iota\beta\omicron\zeta$, meaning "rubbing") and the suffix *-logy* (Greek $\lambda\omicron\gamma\iota\alpha$, meaning "the study of"). The Jost report suggested that problems of lubrication in engineering needed an interdisciplinary approach, including chemistry and materials science, solid mechanics and physics. At that time, Jost suggested that the British industry could have saved £500 million a year "as a result of fewer breakdowns causing lost production; lower energy consumption; reduced maintenance costs; and longer machine life." Fifty years later, frictional losses are often evaluated as costing more than 1% of GDP [2], and tribology is therefore still flourishing.

There is no doubt that tribological interactions have a profound impact on many areas of engineering and everyday life. The widespread significance of these effects has been highlighted in many articles and reports over the

years, which, until recently, have mainly focused on lubrication and friction and wear-related energy and material losses for "traditional" industrial applications, such as manufacturing and automotive. The reader is referred to recent reviews that have, for example, looked at the development of solid lubricant coatings [3], lubrication [4], and the interplay between surfaces and lubricants [5]. Other works have focused on how improvements in friction reduction technologies could significantly reduce frictional energy losses in passenger cars in the short, medium and long term [6]. Reducing wear can also improve long-term efficiency and performance of moving components, as well as reducing the maintenance costs and/or improving the quality of life. Accordingly, much research into means of reducing friction and wear, together with the development of new additives, lubricants and functional materials to improve the performance of interfaces, has taken place, typically in the form of experimental studies for developing improved tribo-materials, topography/textures or lubrication. Most of these activities have been supported and accompanied by fundamental developments in contact mechanics (see, e.g., [7,8]), as well as surface and materials science, (see, e.g., [9]). This has in turn improved our understanding of how surface roughness and surface modifications affect the response of components in various applications [10,11].

More recently, new areas of tribology have emerged, including nanotribology, i.e. the study of friction, wear and lubrication at the nanoscale as applied, for example, to micro- and nano-electromechanical systems (MEMS and NEMS) [12,13] and magnetic storage technologies [14, 15], and biotribology, which deals with human joint prosthetics, dental materials, skin, etc., and ecological aspects of friction, lubrication and wear (e.g., tribology of clean energy sources, green lubricants, biomimetic tribology, etc.) [2,16-19]. Studies of superlubricity, i.e., the mechanisms responsible for extremely

low friction [20-23], have created great expectations in terms of energy savings, and the discovery of graphene is also greatly promising in this direction [24]. The adhesive performance of insects and reptiles inspired numerous studies on adhesive contacts (see, e.g., [25-29]) and resulted in improved understanding and successful mimicking of Nature-made surfaces [30-37]. Massive usage of tactile interfaces triggered multiple studies in understanding sensing through contact and friction [38], and in reproducing interactive haptic feedback to moving fingers [39-42].

In keeping up with and enabling such developments, new knowledge is necessary to describe complex multiscale and multiphysics phenomena within the context of tribology, both in the modeling and experimental domains. In Figure 2.1, we present a map of the computational models currently available, which usually are able to describe only limited ranges in terms of length and time scales. Only more complex models (e.g., atom-to-continuum simulations, hierarchical coupling, etc.) can be extended up to few orders of magnitude of simulated length and time scales, but additional efforts must be done for developing fully multiscale approaches.

All the tribological phenomena happening near interfaces between solids are determined by the atomic interactions within and between solids, as well as those between atoms of the substances present at the interface. Since these interactions give rise to various physics described at the macroscale by different theories and models, the tribological interface can be considered a "paradise" of multiphysics, as schematised in Figure 2.2.

The following types of phenomena may take place in such an interface or in its immediate vicinity: mechanical (solid and fluid), thermal, electromagnetic, metallurgical, quantum and others. Mechanical phenomena can refer to the mechanical deformation of solids and their contact interaction including adhesion and friction. The process of material removal or surface

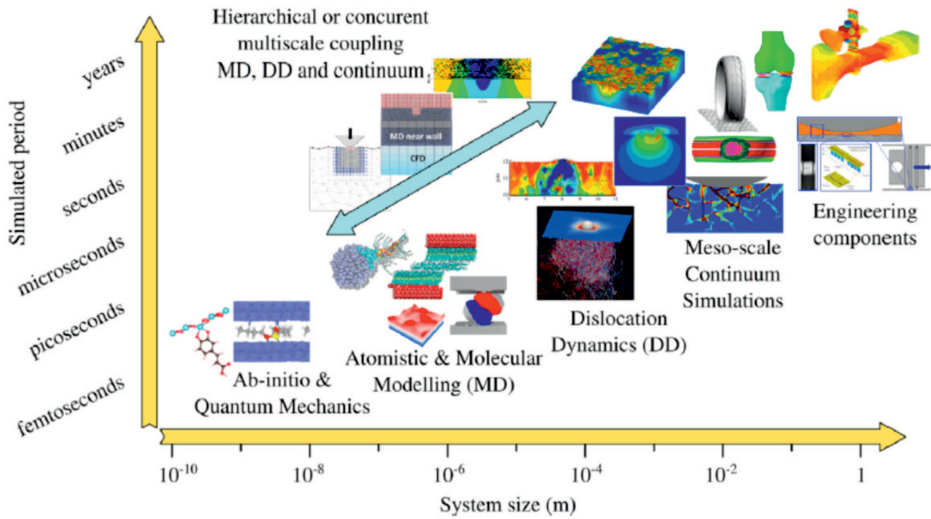


Figure 2.1: A time vs. length scales map of models developed in tribology, highlighting the intrinsic link between multiscale/physics that needs to be captured to provide predictive tools for engineering applications.

deterioration (micro-cracking, abrasive and adhesive wear) can be also included within this type. Thermal phenomena are related to heat transfer from one solid to another, as well as to heat generation due to interfacial friction or due to dissipation in the bulk (viscoelasticity, viscoelastoplasticity, damage accumulation or micro-fractures): heat exchange can be either ballistic or diffusive depending on the size of contact spots [43-45], while radiative and convective heat exchange also contribute considerably to the overall heat conductance [46]. The local heating of contacting asperities up to the point of local melting, recognized in early tribological studies [47] and known as flash-heating, has important implications for friction, especially in dry contacts [48,49]. Metallurgical phenomena happening in near-interface layers span various microstructural changes that are either

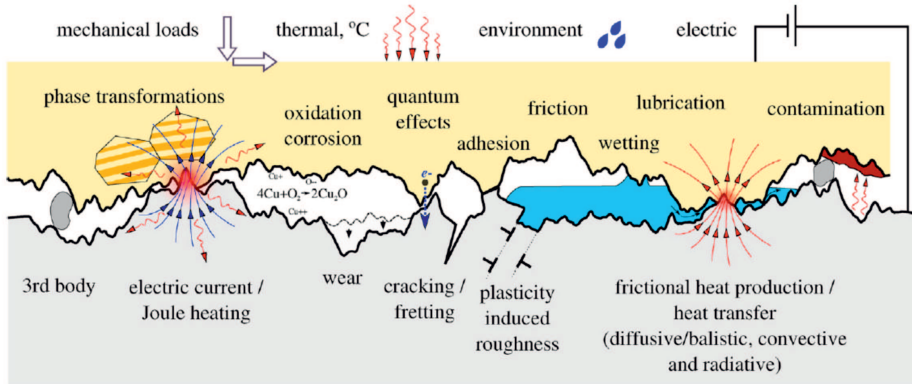


Figure 2.2: A scheme representing the multiphysics nature of tribological interactions, with two different solids with rough surfaces and relevant material microstructures are brought into mechanical contact and exposed to various loads: mechanical, thermal, electric and environmental.

triggered by changes in temperature (e.g., because of Joule or frictional heating) or by severe deformations, and include dynamic recrystallization and various phase transformations; an example is the formation of the so-called "white layer", a fine-grained and rather brittle martensitic layer [50]. For materials experiencing glass transition, the local rise in temperature can be critical for their mechanical performance [51]: in general, the mechanical properties are strongly dependent on the temperature, thus making the thermo-mechanical problem one of the most natural and strongly coupled multiphysics problems in tribology, especially in dry contacts or in the mixed lubrication regime. Because of excessive local heating, the solids can reach their melting or sublimation point and experience phase transition [47]; thus, melting, evaporation and sublimation appear to be important phenomena in dry and lubricated micromechanical interactions. More complicated physics emerge for composite and porous materials; examples of the

latter are rocks experiencing chemical decomposition, water evaporation, pressurization, etc. [52,53]. A complex interaction of the aforementioned physics with a fluid present in the interface is another strongly coupled multiphysics problem, especially for lubrication, sealing applications and saturated fractured media [54-56]. In most situations, the interfacial fluid flow can be considered as a thin flow that can thus be properly described by the Reynolds' equation but, in the case of the fluid viscosity depending on the pressure (piezoviscosity) or temperature, a consistent development of the Navier-Stokes' equations for thin flow should be performed with a priori included pressure dependence in the original equation and not directly into the Reynolds' equation [57].

In addition, tribofilm formation and various tribochemical phenomena taking place at tribological interfaces make them very challenging objects for multiphysics research [58,59]. At the same time, to understand and model such a complex multiphysical problem as a tribological interface, one needs to construct reliable multiphysics models and design appropriate multiphysics tools. Some recent examples of tribology-related modeling applications involving multiphysics coupling include, for example, excitable biological cells, weakly coupled modeling of creeping fluid flow through the contact interface between rough solids [60], and electro-mechanical coupling in contact problems [61]. Because of the complexity of direct experimental measurements and the inseparability of various multiphysics mechanisms in actual interfaces, a big challenge is to construct reliable and precise multiphysics models having predictive power while, at the same time, being verifiable and sufficiently comprehensive.

2.2 Dry friction

2.2.1 Finite and boundary-element simulations

Two major families of methods can be distinguished in continuum mechanics: the finite-element method (FEM) [62] and the boundary-element method (BEM) [63].

The FEM is a versatile method for solving boundary value problems in many fields of science and technology [62,64,65]). In the FEM, an explicit relation between the strain (and possibly strain rate and its history) and the stress can be prescribed, either within infinitesimal or finite strain formulations, enabling this method to consider arbitrary constitutive material models starting from simple linear elasticity up to complex crystal plasticity. The BEM uses in its formulation a fundamental solution for the normal and tangential point forces, which enables linking surface tractions with surface displacements. Equivalently, to formulate a spectral version of the BEM, a fundamental solution linking pressure and vertical displacement for a combination of harmonics in two orthogonal directions should be used [66,67]. Such solutions exist for a limited number of cases and mainly under the assumption that the solid can be locally considered as a flat half-space. These limitations imply a more restrictive field of application for the BEM compared to the FEM, which is a versatile numerical method.

It is worth mentioning that, in general, contact problems are nonlinear even if frictionless and non-adhesive contact is considered between linearly elastic solids. This is because the contact area is *a priori* unknown, apart from simple cases such as the rigid flat stamp problem or the case of full contact. In analogy, a full stick frictional condition (i.e., infinite friction) makes the frictional problem much easier to handle than a problem with a finite friction.

Detailed descriptions of numerical methods within the FEM formulation can be found in the literature, e.g., [68-70], while details on the application of the BEM in rough surface contact mechanics can be found in a comparative analysis of BEM formulations [71]. There are also many instances in which FEM and BEM can be coupled into FEM-BEM solvers for the solution of three-dimensional contact problems [72] or can be combined to achieve different levels of refinement in the solution to the problem under investigation (see, e.g., [73]).

The application of the FEM to tribological problems involves the discretization of the volumes of contacting bodies and an appropriate treatment of their contact interaction. The arbitrariness of material models, as well as the geometries of contacting solids and their heterogeneity that can be reached in the treatment of contact interfaces, make this method a multipurpose engineering tool. However, this is all at the cost of a higher computational complexity than in the BEM, which has less versatility but a much higher efficiency in the treatment of interfacial problems, since it requires solving the problem only for surface degrees of freedom and does not require any discretization in the volume. On the other hand, the BEM results in dense systems of linear algebraic equations, on the contrary of the FEM, which renders sparse systems of equations. Thus, the BEM has to rely on iterative solvers, whereas the FEM can successfully use either iterative or direct solvers based on the sparse matrix storage.

When interested in near-surface stress fields, which are crucial in the reliable analysis of surface deterioration (e.g., fretting fatigue and wear) and microscopic contact at the roughness scale, imprecise integration and/or discretization may result in huge errors in local fields and, thus, in realistic estimations. To properly capture the stress field in the vicinity of a contact zone, and especially near its edges (which, in most problems, is unknown),

a very dense spatial discretization is usually required. The accuracy of the integration technique is especially crucial when a conformal mesh cannot be ensured on the contacting parts (e.g., large-deformation or large-sliding contact systems) and if two deformable solids of comparable stiffness are brought into contact, i.e., when one of the solids cannot be considered as rigid. In addition, the path-dependence of frictional problems requires that the load increment should be chosen properly, as the temporal discretization plays a crucial role even in quasi-static problems. As an example, for the shear tractions in normal Hertzian cylindrical contact with friction in the interface, the self-similar character of the solution, as argued by Spence [74], can be obtained with one hundred load steps with the displacement increment proportional to the time squared, but not within one single load step.

In tribology, due to its computational cost, application of the FEM is justified if the problem at hand cannot be solved within the assumptions of the BEM, namely the existence of a fundamental solution and the local flatness of the surface (i.e., small slope). A broad family of systems falls within this context: large-deformation, large-sliding contact of soft bodies, which can be observed in various biological systems (e.g., oral food processing, contact of skin, etc.), but also in engineering applications (e.g., contact of tires, polymeric seals and many others) or contacts involving strongly nonlinear material behavior which is hard to represent within the BEM framework, such as indentation involving strong finite-strain plastic deformations or fracture in the interface.

Concerning the applications to microcontacts and microtribology, both the FEM and the BEM are used extensively. At the scale of roughness, the macroscopic shape of the contacting solids can be usually neglected and, since the roughness slope is in general rather small, the problem satisfies the

main assumption of the BEM, which can be successfully used for its solution. The evolution of the true contact area, interface permeability, electric and thermal contact resistance can all be resolved in the framework of the BEM for linear material laws. Regarding material nonlinearities, elasto-plastic [75-77] and viscoelastic [78,79] material behavior can be incorporated in the BEM framework by assuming that deformations and slopes remain small, otherwise the FEM would be needed [80,81]. It should be remarked that most contact systems involving elasto-plastic materials operate mainly in the elastic regime both at the micro- and macroscales; hence, depending on the level of stress and the type of loading, considering plastic deformation may be important during the first loading cycles but may not be needed in subsequent ones.

The BEM framework can consider homogeneous nonlinear material behavior, but can also account for heterogeneous inclusions in the bulk, see e.g., [82], which is computationally much more expensive. Accounting for heterogeneous materials is often critical for microscale analyses in which the material microstructure might play an important role. This is the case, for instance, in contact problems involving functionally graded interfaces [83], and metallic polycrystalline [84] or monocrystalline [85] microstructures, whose accurate treatment requires the FEM. Concerning multiphysics (or multi-field) problems, both methods are comparable at the scale of roughness, with the same limitations and advantages: simple but fast BEM versus slow FEM but with capabilities to account for arbitrary complexity. Examples of applications include: lubrication problems [86-88], electro-elastic contact modeling [61,89], thermo-mechanical coupling [90], and many others.

Using BEM-type formulations has also been used to treat elasto-dynamic

frictional problems [91,92], whereas complex geometries and boundary conditions would still require usage of FEM or equivalent formulations [93,94].

In summary, both the FEM and BEM are well developed and able to solve most micro-tribological problems involving both material nonlinearities and multiphysical couplings with the FEM being more versatile and more easily accessible for a general researcher and engineer (numerous commercial and open software are available) but computationally costly, and the BEM being less available and versatile, but still capable of solving most problems under reasonable assumptions and for very moderate computational costs. The main challenge here for the researchers and engineers would be to promote both methods within the homologue communities and to enable them to use one or the other based on the needs of the target application.

2.2.2 Friction between patterned surfaces

In many practical applications, the emergent frictional behavior is not only determined by microscopic degrees of freedom or surface roughness, but also by other mesoscopic or macroscopic length scales characterising the material surfaces. The hierarchical structure of the gecko paw is one of the most cited examples to illustrate the role of a complex contact structure, and many research efforts have been devoted to understand the origin of its properties of adhesion and friction [13, 95-98].

In general, many biological materials are characterized by a non-uniform complex surface structure, e.g., insect legs [99], lotus leaves [100,101], nacre [102], as well as animal [103-105] and human skin [106-108], -whose hierarchical scheme of contact splitting has been described as a way to optimise surface adaptability, self-cleaning and self-healing abilities, and to avoid self-bunching [96]-, and are therefore difficult to model in a single framework.

The exceptional mechanical properties of these systems have attracted a lot of interest, and led to attempts to reproduce their behaviors artificially with specific geometric features of the surfaces. The main focus of research in bio-inspired materials is to design new materials by mimicking nature, aiming to manipulate the mechanical properties of a system through a complex organization of microscopic components rather than introducing new chemical and physical features [31, 109-113]. Understanding and optimising friction in these bio-inspired complex surfaces is an open challenge.

Recently, experimental results have been obtained for the friction of specific textured surfaces, e.g., honeycomb structures [114,115], periodic regular grooves both in dry and wet conditions [38,116-119], as well as pillars and dimples [120-123]. Molecular Dynamics (MD) simulations have been adopted to investigate the effect of patterning in the presence of lubricants [124], but the theoretical and numerical modeling of dry friction in these systems shares the difficulties inherent to that of the friction of rough surfaces: how to take into account within a unified framework concurrent length scales spanning orders of magnitude and involving many physical mechanisms. For this reason, much work remains to be done on this topic. Some results have been obtained by means of a simplified approach based on numerical simulations of the spring-block model [125], aiming to investigate the qualitative frictional behavior of patterned surfaces [126-129]. In order to study the role of specific surface structures, it is not necessary to include into a model the details of all microscopic interactions, since they can be taken into account with an effective description at the mesoscale, where the system is discretized into elementary components whose interactions are described in terms of forces within the framework of classical mechanics. Thus, surface structures are introduced by means of the arrangement of elementary components, and the effects on the macroscopic friction coefficient

are deduced from the numerical solution of the overall equations of motion of the system. With this procedure, some versions of the spring-block model have been successfully used to model and understand the existence of slow detachment fronts [130-133], crack-like precursors of sliding [134-137], and stick-slip sliding [138,139], consistent with experimental observations [140-144].

Despite the approximations and apparent simplicity of the model, the spring-block approach can provide a qualitative understanding of relevant phenomena with computationally inexpensive numerical simulations. The results of these studies show how static friction can be tuned and optimised by means of a specific arrangement of surface structures. In particular, it has been demonstrated that the static friction coefficient is reduced by means of large surface grooves [126] and that a hierarchical organization of grooves with different length scales can be used to tune it to a desired value [127]. Also, it has been proved that a remarkable reduction of the global static friction of a surface can be obtained by means of a hierarchical organization of regions with different local static friction coefficients [128]. Recently, a two-dimensional version of the spring-block model has been adopted to simulate the effect of surface patterns like pillars or cavities [129] and the frictional behaviour of graded materials, as shown in Chapter 3. A natural development based on this research is to improve the spring-block model by relaxing some of its approximations, for example, by simulating more realistic three-dimensional surfaces; furthermore, variations of the surface roughness after the onset of sliding or other long-term effects during the dynamic phase can be incorporated.

2.3 Fluid and solid lubrication

2.3.1 Literature review

Everyday experience shows that interposing a fluid between two contacting bodies dramatically drops the friction force. Lubrication has, then, a paramount importance in engineering and applied science research since it is clearly related to an improved energy efficiency, to a better durability of components and systems, and, ultimately, to economic savings.

Theoretical investigations take their origin in the pioneering studies made by Reynolds in the 19th century [145]: the Reynolds' equations enable the analysis, in terms of velocity and pressure distribution, of flow in a lubrication channel. In the last fifty years, a lot of approaches, mainly numerical [146], have been developed to address the solution of this set of equations: nowadays, it is even possible to account for a variety of non-Newtonian effects, ranging from piezo-viscosity to shear thinning. For a more comprehensive overview, the reader is also referred to Hamrock's classical book [147].

In recent years, textured surfaces for the optimisation of hydrodynamically lubricated contacts have been developed (see, e.g., [148], also inspired by Nature [149]). The main effect of the presence of dimples, pockets or asperities is an increase in the load-carrying capacity of the bearing and eventually a reduction in the coefficient of friction. The main challenge in modeling the hydrodynamic lubrication between textured surfaces remains the description of the cavitation, for which many models have been proposed (e.g., finite-difference algorithms [150,151] based on the well-accepted JFO boundary conditions [152,153]). In addition, multiphase computational fluid dynamics (CFD) simulations have been used to model cavitation but,

given the complexity of the problem and the coupling with appropriate turbulence models, it is still a challenging task [154]. Multiscale approaches should be developed in order to capture both the macroscopic tribological characteristics of a lubricated contact and the micro-hydrodynamics, with the related phenomena of roughness-induced cavitation and turbulence.

Furthermore, in order to completely assess the problem, the solution of the lubricant fluid dynamics has to be coupled with the analysis of the mechanics of the contacting solids: in elasto-hydrodynamic lubrication, the fluid pressure is high enough to entail an elastic deformation of the lubricated bodies. Consequently, the pressure field has to satisfy, at the same time, the Reynolds' equation and the elasticity constitutive relations. The intricacy of the problem surges when the roughness of the contacting solids is accounted for. Indeed, the mathematical form of the problem does not change, but the number of elements required to find a numerical solution and, in particular, to explicitly resolve the effects of rough contact cannot be handled with the computational resources currently available. Consequently, a deterministic approach which accounts for the contact interactions at all relevant roughness scales is unfeasible; instead, various homogenization methods have been developed to overcome these limitations. The most commonly used approach solves the Reynolds' equation as if the surfaces were smooth and uses "flow factors" as statistically corrective terms for the surface roughness [155]. This approach was pioneered by Patir and Cheng [156], and then further developed by Elrod [157] and Tripp [158] to account for anisotropic effects. Furthermore, recent investigations have shown that more accurate estimations may be performed by employing, instead of scalar coefficients, flow factor tensors, which are functions of the surface roughness and, specifically, of the anisotropy roughness tensor [159].

When the contact or environmental conditions do not permit fluid film lubrication, e.g., when extreme temperatures and/or pressures are present, as in aerospace applications [160], solid lubricants are generally employed. It should be noted that, in the literature, a distinction is made between powder and granular lubricants, on the basis of the particle characteristics and their load-carrying capacity generation mechanisms [161]. Many analytical models of solid lubrication have been developed over the years, starting from analogies with fluid mechanics and the conservation laws for mass, momentum and energy [162,163]. The kinetic theory of gases, instead, has been the basis for the development of the granular kinetic lubrication theory [164,165]. Both continuum and discrete models are available for the description of solid lubrication or, more in general, of third body friction [166].

Continuum modeling approaches are based on rheological laws describing the third body, originally introduced by Heshmat [167]. Discrete simulations, instead, allow the precise computation of particle dynamics and take into account individual particle-particle and particle-wall interactions [168]. Solid lubrication is intrinsically a multiscale and multiphysics problem. Therefore, an effective modeling approach should be able to include the microscopic physical (e.g., surface roughness), chemical (e.g., tribo-corrosion [169]) and thermal interactions, and to link them to the frictional characteristics of the tribo-contact. Hence, discrete approaches and particle-based methods seem more promising, despite necessitating further efforts to make the micro-to-macro correlation.

In addition, recently novel lubricants have been developed, e.g., using additives to improve anti-wear properties, allowing to extend the life of tribo-contacts. Nanolubricants, for instance, display exceptional thermal and

tribological properties and are obtained by adding nanometer-sized particles to a base fluid. The development and study of the response of additive molecules and nanoparticles, and the effect they have on friction reduction and boundary lubrication, is usually achieved through detailed atomistic modelling. A detailed overview of modeling methods used in this area is provided in [170].

2.3.2 Simulation methods

Hydrodynamic lubrication (HL) and elastohydrodynamic lubrication (EHL) are lubrication regimes where a thin lubricant film is formed between two surfaces in relative motion. HL takes place in conformal contacts, when low pressures are established between the two surfaces, while EHL takes place when pressures are significant enough to cause considerable elastic deformation of the surfaces. EHL usually occurs in non-conformal contacts and many machine elements, including rolling bearings and gears, rely on EHL in their operation. Existence of a fluid film sufficient to separate two surfaces under hydrodynamic conditions, such as in a journal bearing, has been known since the work of Tower in 1883 [171]; however, it was not until 1949 that Grubin predicted that a thin fluid film can also separate surfaces in high pressure, non-conformal contacts [172]. Formation of such a film is possible due to high pressure having two beneficial effects: firstly, it increases lubricant viscosity in the contact inlet and, secondly, it elastically deforms and flattens the contacting surfaces, hence the term elasto-hydrodynamic lubrication.

Classical solutions of HL and EHL contact problems use the Reynolds' equation [145] to describe the behavior of the lubricant, while elastic deformation is traditionally calculated using the Hertz's theory of elastic contact, although nowadays BEM or FEM solvers are also routinely used. Reynolds's

equation is a simplification of the full Navier-Stokes' equations, derived by assuming a Newtonian lubricant with constant density and constant pressure and viscosity across the film thickness. Cameron and Wood [173] developed the first Reynolds-based computerised numerical solutions for hydrodynamic lubrication and in 1959 Dowson and Higginson [174] produced the first full numerical solution for EHL. Subsequently, Dowson and co-workers, also proposed regression equations for prediction of the EHL film thickness based on their numerical solutions and a number of other improvements including the consideration of material properties and thermal effects (e.g., [175-177]).

In the last fifty years, many numerical approaches [146,147,178-180] have been developed to address the solution of this set of equations: nowadays, it is possible to account for a variety of non-Newtonian effects, ranging from piezo-viscosity to shear thinning. The majority of these approaches uses a Finite Difference (FD) scheme, although the use of the FEM and Finite Volume (FV) methodologies has recently been proposed especially to overcome some of the limitations of FD when dealing with complex domains in the presence of micro-textured surfaces and cavitation using mass-conserving algorithms [181-183], but also to extend a Reynolds-type solver to full CFD studies looking at the fluid flow outside the contact, overcoming the limitations of the Reynolds' assumptions in specific extreme contact conditions [184-187]. The development of fully-coupled solid-fluid interactions (SFI) solvers [188] constitutes the new frontier of this particular area of research, with the promise that advances in computational power may lead to a more comprehensive study of the multiphysics phenomena governing three-dimensional contact problems considering full field deformations, thermal and multi-field effects, and the complex rheologies of the fluids and the solids under investigation. Hybrid techniques (e.g., the element-based

finite volume method - EbFVM [189-190]) have also been recently developed to combine the flexibility of finite elements in terms of studying complex domains and using unstructured meshes, and the use of finite volumes to accurately solve the fluid-dynamic problem at hand.

2.4 Diffusion at polymer interfaces

2.4.1 Adhesion phenomena

Diffusivity of species across polymer interfaces is one of the most important parameters governing adhesion, which affects, e.g., the strength of polymer-matrix composites. Almost all the numerical research works investigating adhesion on polymer interfaces are based on MD simulations. In general, it is found that inter-diffusion of polymer-polymer interfaces is controlled more by the short (i.e., fast) chains than by the long (i.e., slow) chains: a deeper diffusion leads to improved ductility of the interface, enabling a higher resistance to mechanical strains [191].

When one of the two polymers at the interface has a crystalline phase, its surface structure can influence heavily the adhesive properties. As shown by Quddus *et al.*, the work of adhesion of oleic acid on crystalline cellulose is higher for the [010] plane, due to the higher surface area and the larger density of H-bonding sites available. In this case, the diffusion of oleic acid molecules is crucial for accessing the underlying cellulose plane and thus new H-bonding sites [192]. In another study, the adhesion process of a fluoropolymer on different 1,3,5-triamino-2,4,6-trinitrobenzene surfaces is investigated. In this case, adhesion results significantly enhanced onto the [100] plane rather than onto the [001] plane [193], probably due to the higher accessible surface area and free volume for inter-diffusion.

Sometimes functionalised surfaces are exploited to enhance adhesion, especially for increasing the mechanical performance of composite materials, and MD studies are successfully employed to describe these effects [194,195]. In this case, the main mechanism is only slightly dependent on diffusion, because the presence of functional groups affects adhesion primarily by changing the van der Waals interactions at the interface.

When the interface is between a polymer and a metal, diffusion processes become negligible and the adhesive strength of the interface depends on the non-bonded interactions. Some research works employed full-atom molecular dynamics simulation or coarse-grained models to investigate the effect of a metal surface on the polymer structure, whose chain length and flexibility affects adhesion energy and the extent of the interphase [196,197]. More in general, there is a competition between the transport of polymers towards an interface and the subsequent spreading, which can reduce the adsorbed amount [198].

MD simulations of adhesive interfaces are employed also to study self-healing mechanisms, which are driven by the self-diffusion of molecules across a crack interface and are strongly time-dependent. For instance, self-healing in asphalt binder was investigated by MD simulations [199,200] and the main properties affecting diffusion across the interface, e.g. polymer chain length and branching, have been highlighted. The self-healing process results improved when the same conditions leading to higher and faster diffusion are met, e.g., an increased temperature. MD simulations were employed also by Liu *et al.* [201], who evaluated the performance of carbon nanotubes as containers in self-healing materials, thanks to their suitability in releasing polymer molecules. In other cases, numerical models have been purposely developed to describe the multiscale nature of self-healing processes and the properties of the resulting healed materials. Aliko-Benítez *et al.* [202] and

Bluhm *et al.* [203] followed different approaches to implement self-healing into the 3D FEM. In both cases, healing was decoupled from material damage and its effect was measured by monitoring the time evolution of diffusive species or the recovery in mechanical strength by a cracked specimen. Additional theoretical studies were focused on developing multiscale models for the extraction of the macroscopic properties of the material as a function of a healing rate [204-206]. The results highlighted that significant improvements in the material strength and fracture toughness if self-healing can take place at the smallest possible scale.

2.4.2 Polymer nanotribology

When two polymer surfaces are in relative motion, diffusion process can heavily impact their tribological properties. Simulation in tribology has a high level of complexity due to the intrinsically multiscale and multiphysics nature of the involved phenomena, and this is further complicated by the complex structure of polymers. In a recent review by Myshkin and Kovalev, the adhesion mechanisms leading to the main tribological properties observed in polymers are highlighted and, as discussed before, they are strictly related to inter-diffusion [207].

Only few numerical research works are available on this topic and are based on MD simulations. Brostow *et al.* performed some scratching simulations on computer-generated polymeric materials, finding that the spatial structure of the chains affects significantly the scratch resistance. Specifically, when a chain segment on the scratching path is bonded to a segment immediately below it on the scratching layer, a reduced penetration depth (i.e., an increased wear resistance) is measured [208]. Yew *et al.* found that the sliding friction of a polymer-polymer interface is found to be lower for materials with higher molecular weight, since the inter-diffusion of long chains

is more difficult [209]. This behaviour can be observed in Figure 2.4: the interpenetration of the ends of chains is strongly dependent on the molecular weight of the polymer, thus affecting the contact area and the coefficient of friction.

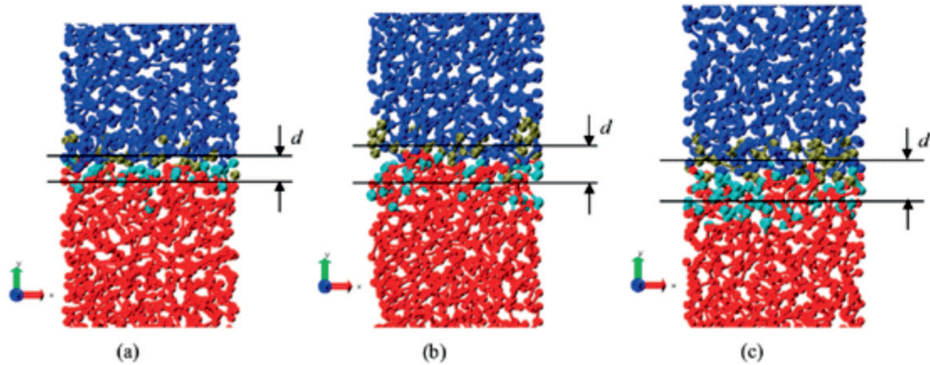


Figure 2.3: Snapshots of MD simulations of two polymer blocks in contact, with different molecular weights: (a) 14000, (b) 3500, (c) 700. Cyan and green atoms represent the ends of chains belonging to the lower (red) and to the upper block (blue), respectively. From [209].

In recent years, the use of organic friction modifiers has acquired a growing interest in industry. Their effect on the macroscopic tribological properties is usually investigated with atomistic simulations [210-212] and the system can be further complicated through the introduction of the lubricant molecules. The diffusion and mobility of a lubricant within the organic friction modifier can have a fundamental effect on the coefficient of friction, but these phenomena have not been deeply investigated so far.

2.5 Conclusions

Despite it is nowadays possible to model elastic contact problems of great complexity at various scales, significant effort is still required to account for effects like plasticity, adhesion, friction, wear, lubrication and surface chemistry in tribological models. Although many systems do involve two or more of those phenomena at various scales, multiscale and multiphysics models are still challenging to develop and use as they require multidisciplinary expertise and collaborative effort. Nevertheless, a few successful examples are provided in the text. Breakthroughs are thus expected from the future development of versatile and efficient multiscale and multiphysics tools dedicated to tribology. On the other hand, tribologists still need to identify key elementary processes specific to rough contacts under shear, and associated, for example, to crack nucleation and propagation, chemical reactions, or fluid-solid interactions. In order to keep a clear physical understanding of the outcome of complex models, those processes will preferably be first studied on their own, before introducing the related behavior laws in more comprehensive tools. Only by pursuing simultaneously both research avenues the tribology community will have a chance (i) to advance on the fundamental understanding of frictional interfaces and (ii) to propose simple but comprehensive models useful to optimise and control industrial processes.

References

- [1] Jost H.P., 1966. *Lubrication (Tribology): Education and research - Report on the Present Position and Industry's Needs*. Department of Education and Science by the Lubrication Engineering and Research Working Group, HM Stationery Office.

- [2] Tzanakis I., Hadfield M., Thomas B., Noya S., Henshaw I., Austen S., 2012. Future perspectives on sustainable tribology. *Renewable & Sustainable Energy Reviews* 16, 4126.
- [3] Donnet C., Erdemir A., 2004. Solid lubricant coatings: recent developments and future trends. *Tribology Letters* 17, 389.
- [4] Spikes H., 2006. Sixty years of EHL. *Lubrication Science* 18, 265.
- [5] Neville A., Morina A., Haque T., Voong M., 2007. Compatibility between tribological surfaces and lubricant additives how friction and wear reduction can be controlled by surface/lube synergies. *Tribology International* 40, 1680.
- [6] Holmberg K., Andersson P., Erdemir A., 2012. Global energy consumption due to friction in passenger cars. *Tribology International* 47, 221.
- [7] Greenwood J.A., Williamson J.B.P., 1966. Contact of nominally flat surfaces. *Proceedings of the Royal Society of London A: Mathematical, Physical and Engineering Sciences* 295, 300.
- [8] Persson B.N.J., 2001. Theory of rubber friction and contact mechanics. *Journal of Chemical Physics* 115, 3840.
- [9] Carpick R.W., Salmeron M., 1997. Scratching the surface: fundamental investigations of tribology with atomic force microscopy. *Chemical Reviews* 97, 1163.
- [10] Persson B.N.J., Albohr O., Tartaglino U., Volokitin A., Tosatti E., 2004. On the nature of surface roughness with application to contact mechanics, sealing, rubber friction and adhesion. *Journal of Physics: Condensed Matter* 17, R1.
- [11] Morales-Espejel G.E., 2014. Surface roughness effects in elastohydrodynamic lubrication: a review with contributions. *Proceedings of the Institution of Mechanical Engineers, Part J: Journal of Engineering Tribology* 228, 1217.
- [12] Kim S.H., Asay D.B., Dugger M.T., 2007. Nanotribology and MEMS. *Nano Today* 2, 22.
- [13] Bhushan B., 2007. Nanotribology and nanomechanics of MEMS/NEMS and BioMEMS/ BioNEMS materials and devices. *Microelectronics Engineering* 84, 387.
- [14] Canchi S.V., Bogy D.B., 2011. Thermal fly-height control slider instability and dynamics at touchdown: explanations using nonlinear systems theory. *Journal of Tribology, Transactions ASME* 133, 021902.
- [15] Vakis A.I., Hadjicostis C.N., Polycarpou A.A., 2012. Three-DOF dynamic model with lubricant contact for thermal fly-height control nanotechnology. *Journal of Physics D* 45, 135402.

- [16] Cann P., Wimmer M., 2015. Welcome to the first issue of Biotribology. *Biotribology* 1-2, 1.
- [17] van Kuilenburg J., Masen M.A., van der Heide E., 2015. A review of fingerpad contact mechanics and friction and how this affects tactile perception. *Proceedings of the Institution of Mechanical Engineers, Part J: Journal of Engineering Tribology* 229, 243.
- [18] Ma S., Scaraggi M., Wang D., Wang X., Liang Y., Liu W., Dini D., Zhou F., 2015. Nanoporous substrate infiltrated hydrogels: a bioinspired regenerable surface for high load bearing and tunable friction. *Advanced Functional Materials* 25, 7366.
- [19] Rashid H., 2014. The effect of surface roughness on ceramics used in dentistry: a review of literature. *European Journal of Dentistry* 8, 571.
- [20] Martin J., Donnet C., Le Mogne T., Epicier T., 1993. Superlubricity of molybdenum disulphide. *Physical Review B* 48, 10583.
- [21] Dienwiebel M., Verhoeven G.S., Pradeep N., Frenken J.W., Heimberg J.A., Zandbergen H.W., 2004. Superlubricity of graphite. *Physical Review Letters* 92, 126101.
- [22] Hirano M., Shinjo K., 1993. Superlubricity and frictional anisotropy. *Wear* 168, 121.
- [23] Urbakh M., 2013. Friction: towards macroscale superlubricity. *Nature Nanotechnology* 8, 893.
- [24] Berman D., Deshmukh S.A., Sankaranarayanan S.K., Erdemir A., Sumant A.V., 2015. Friction. Macroscale superlubricity enabled by graphene nanoscroll formation. *Science* 348, 1118.
- [25] Carbone G., Pierro E., Gorb S.N., 2011. Origin of the superior adhesive performance of mushroom-shaped microstructured surfaces. *Soft Matter* 7, 5545.
- [26] Afferrante L., Carbone G., Demelio G., Pugno N.M., 2013. Adhesion of elastic thin films: double peeling of tapes versus axisymmetric peeling of membranes. *Tribology Letters* 52, 439.
- [27] Kim T.W., Bhushan B., 2008. The adhesion model considering capillarity for gecko attachment system. *Journal of the Royal Society Interface* 5, 319.
- [28] Persson B.N.J., Gorb S., 2003. The effect of surface roughness on the adhesion of elastic plates with application to biological systems. *Journal of Chemical Physics* 119, 11437.

- [29] Papangelo A., Ciavarella M., 2017. A Maugis-Dugdale cohesive solution for adhesion of a surface with a dimple. *Journal of the Royal Society Interface* 14, 20160996.
- [30] Geim A.K., Dubonos S., Grigorieva I., Novoselov K., Zhukov A., Shapoval SY., 2003. Microfabricated adhesive mimicking gecko foot-hair. *Nature Materials* 2, 461.
- [31] Zhou M., Pesika N., Zeng H., Tian Y., Israelachvili J.N., 2013. Recent advances in gecko adhesion and friction mechanisms and development of gecko-inspired dry adhesive surfaces. *Friction* 1, 114.
- [32] Huber G., Mantz H., Spolenak R., Mecke K., Jacobs K., Gorb S.N., Arzt E., 2005. Evidence for capillarity contributions to gecko adhesion from single spatula nanomechanical measurements. *Proceedings of the National Academy of Sciences of the United States of America* 102, 16293.
- [33] Ma S., Scaraggi M., Lin P., Yu B., Wang D., Dini D., Zhou F., 2017. Nanohydrogel brushes for switchable underwater adhesion. *Journal of Physical Chemistry C* 121, 8452.
- [34] Kappl M., Kaveh F., Barnes W.J.P., 2016. Nanoscale friction and adhesion of tree frog toe pads. *Bioinspiration & Biomimetics* 11, 035003.
- [35] Gorb S.N., Sinha M., Peressadko A., Daltorio K.A., Quinn R.D., 2007. Insects did it first: a micropatterned adhesive tape for robotic applications. *Bioinspiration & Biomimetics* 2, S117.
- [36] Autumn K., Sitti M., Liang Y.A., Peattie A.M., Hansen W.R., Sponberg S., Kenny T.W., Fearing R., Israelachvili J.N., Full R.J., 2002. Evidence for van der Waals adhesion in gecko setae. *Proceedings of the National Academy of Sciences of the United States of America* 99, 12252.
- [37] Cho K., Koh J., Kim S., Chu W., Hong Y., Ahn S., 2009. Review of manufacturing processes for soft biomimetic robots. *International Journal of Precision Engineering and Manufacturing* 10, 171.
- [38] Scheibert J., Leurent S., Prevost A., Debregeas G., 2009. The role of fingerprints in the coding of tactile information probed with a biomimetic sensor. *Science* 323, 1503.
- [39] Hayward V., 2011. Is there a 'plenhaptic' function? *Philosophical Transactions of the Royal Society of London B: Biological Sciences* 366, 3115.
- [40] Prescott T.J., Diamond M.E., Wing A.M., 2011. Active touch sensing. *Philosophical Transactions of the Royal Society of London B: Biological Sciences* 366, 2989.

- [41] Klocker A., Wiertlewski M., Theate V., Hayward V., Thonnard J., 2013. Physical factors influencing pleasant touch during tactile exploration. *PLoS ONE* 8, e79085.
- [42] Johnson M.T., Sluis V.D., Brokken D., 2013. User interface with haptic feedback. US patent 13/879,420.
- [43] Schwab K., Henriksen E., Worlock J., Roukes M.L., 2000. Measurement of the quantum of thermal conductance. *Nature* 404, 974.
- [44] Chen G., 2001. Ballistic-diffusive heat-conduction equations. *Physical Review Letters* 86, 2297.
- [45] Anciaux G., Molinari J.F., 2013. A molecular dynamics and finite elements study of nanoscale thermal contact conductance. *International Journal of Heat and Mass Transfer* 59, 384.
- [46] Madhusudana C., 1996. *Thermal contact conductance*. Springer, Berlin, Germany.
- [47] Bowden F.P., Tabor D., 2001. *The friction and lubrication of solids*. Oxford University Press, Oxford, United Kingdom.
- [48] Rice J.R., 2006. Heating and weakening of faults during earthquake slip. *Journal of Geophysical Research B* 111, B05311.
- [49] Goldsby D.L., Tullis T.E., 2011. Flash heating leads to low frictional strength of crustal rocks at earthquake slip rates. *Science* 334, 216.
- [50] Ramesh A., Melkote S.N., 2008. Modeling of white layer formation under thermally dominant conditions in orthogonal machining of hardened AISI 52100 steel. *International Journal of Machine Tools and Manufacture* 48, 402.
- [51] Ward I., Hine P., 2004. The science and technology of hot compaction. *Polymer* 45, 1413.
- [52] Dieterich J.H., 1972. Time-dependent friction in rocks. *Journal of Geophysical Research* 77, 3690.
- [53] Collettini C., Viti C., Tesi T., Mollo S., 2013. Thermal decomposition along natural carbonate faults during earthquakes. *Geology* 41, 927.
- [54] Dresel W., 2007. *Lubricants and lubrication*. John Wiley & Sons, New York, United States of America.
- [55] Muller H.K., Nau B.S., 1998. *Fluid sealing technology: principles and applications*. Marcel Dekker, New York, United States of America.

- [56] Power W., Durham W., 1997. Topography of natural and artificial fractures in granitic rocks: implications for studies of rock friction and fluid migration. *International Journal of Rock Mechanics and Mining Sciences* 34, 979.
- [57] Rajagopal K., Szeri A., 2003. On an inconsistency in the derivation of the equations of elastohydrodynamic lubrication. *Proceedings of the Royal Society of London A: Mathematical, Physical and Engineering Sciences* 459, 2771.
- [58] De Barros-Bouchet M.I., Righi M.C., Philippon D., Mamingo-Doumbe S., Le-Mogne T., Martin J.M., Bouffet A., 2015. Tribochemistry of phosphorus additives: experiments and first-principles calculations. *RSC Advances* 5, 49270.
- [59] Zilibotti G., Corni S., Righi M.C., 2013. Load-induced confinement activates diamond lubrication by water. *Physical Review Letters* 111, 146101.
- [60] Dapp W.B., Lucke A., Persson B.N.J., Muser M.H., 2012. Self-affine elastic contacts: percolation and leakage. *Physical Review Letters* 108, 244301.
- [61] Rodriguez-Tembleque L., Saez A., Buroni F.C., Aliabadi F.M., 2016. Quasi-static electroelastic contact modeling using the boundary element method. *Key Engineering Materials* 681, 185.
- [62] Zienkiewicz O.C., Taylor R.L., 2000. *The finite element method: solid mechanics*. Butterworth-Heinemann, New York, United States of America.
- [63] Banerjee P.K., Butterfield R., 1981. *Boundary element methods in engineering science*. McGraw-Hill, London, United Kingdom.
- [64] Hrennikoff A., 1941. Solution of problems of elasticity by the framework method. *Journal of Applied Mechanics, Transactions of ASME* 8, 169.
- [65] Courant R., 1943. Variational methods for the solution of problems of equilibrium and vibrations. *Bulletin of the American Mathematical Society* 49, 1.
- [66] Johnson K.L., Greenwood J.A., Higginson J.G., 1985. The contact of elastic regular wavy surfaces. *International Journal of Mechanical Sciences* 27, 383.
- [67] Stanley H.M., Kato T., 1997. An FFT-based method for rough surface contact. *Journal of Tribology, Transactions of ASME* 119, 481.
- [68] Laursen T.A., 2002. *Computational Contact and Impact Mechanics*. Springer, Berlin, Germany.
- [69] Wriggers P., 2006. *Computational Contact Mechanics*. Springer, Berlin, Germany.

- [70] Yastrebov V.A., 2013. *Numerical Methods in Contact Mechanics*. John Wiley & Sons, New York, United States of America.
- [71] Bemporad A., Paggi M., 2015. Optimization algorithms for the solution of the frictionless normal contact between rough surfaces. *International Journal of Solids and Structures* 69-70, 94.
- [72] Rodriguez-Tembleque L., Abascal R.A., 2010. 3D FEMBEM rolling contact formulation for unstructured meshes. *International Journal of Solids and Structures* 47, 330.
- [73] Zografos A., Dini D., Olver A.V., 2009. Fretting fatigue and wear in bolted connections: a multi-level formulation for the computation of local contact stresses. *Tribology International* 42, 1663.
- [74] Spence D.A., 1975. The Hertz contact problem with finite friction. *Journal of Elasticity* 5, 297.
- [75] Jacq C., Nelias D., Lormand G., Girodin D., 2002. Development of a three-dimensional semi-analytical elastic.plastic contact code. *Journal of Tribology, Transactions of ASME* 124, 653.
- [76] Sahlin F., Larsson R., Almqvist A., Lugt P.M., Marklund P., 2010. A mixed lubrication model incorporating measured surface topography. Part 1: theory of flow factors. *Proceedings of the Institution of Mechanical Engineers, Part J: Journal of Engineering Tribology* 224, 335.
- [77] Sahlin F., Larsson R., Marklund P., Almqvist A., Lugt P.M., 2010. A mixed lubrication model incorporating measured surface topography. Part 2: roughness treatment, model validation, and simulation. *Proceedings of the Institution of Mechanical Engineers, Part J: Journal of Engineering Tribology* 224, 353.
- [78] Carbone G., Putignano C., 2013. A novel methodology to predict sliding and rolling friction of viscoelastic materials: theory and experiments. *Journal of the Mechanics and Physics of Solids* 61, 1822.
- [79] Bugnicourt R., Sainsot P., Lesaffre N., Lubrecht A.A., 2017. Transient frictionless contact of a rough rigid surface on a viscoelastic half-space. *Tribology International* 113, 279.
- [80] Yastrebov V.A., Durand J., Proudhon H., Cailletaud G., 2011. Rough surface contact analysis by means of the Finite Element Method and of a new reduced model. *CR Mecanique* 339, 473.
- [81] Scaraggi M., Comingio D., Al-Qudsi A., De Lorenzis L., 2016. The influence of geometrical and rheological non-linearity on the calculation of rubber friction. *Tribology International* 101, 402.

- [82] Leroux J., Fulleringer B., Nelias D., 2010. Contact analysis in presence of spherical inhomogeneities within a half-space. *International Journal of Solids and Structures* 47, 3034.
- [83] Paggi M., Zavarise G., 2011. Contact mechanics of microscopically rough surfaces with graded elasticity. *European Journal of Mechanics of Solids* 30, 696.
- [84] Dick T., Cailletaud G., 2006. Fretting modelling with a crystal plasticity model of Ti6Al4V. *Computational Materials Science* 38, 113.
- [85] Casals O., Forest S., 2009. Finite element crystal plasticity analysis of spherical indentation in bulk single crystals and coatings. *Computational Materials Science* 45, 774.
- [86] Yang B., Laursen T.A., 2009. A mortar-finite element approach to lubricated contact problems. *Computational Methods in Applied Mechanics and Engineering* 198, 3656.
- [87] Nanbu T., Ren N., Yasuda Y., Zhu D., Wang Q.J., 2008. Micro-textures in concentrated conformal-contact lubrication: effects of texture bottom shape and surface relative motion. *Tribology Letters* 29, 241.
- [88] Stupkiewicz S., Lengiewicz J., Sadowski P., Kucharski S., 2016. Finite deformation effects in soft elastohydrodynamic lubrication problems. *Tribology International* 93, 511.
- [89] Yastrebov V.A., Cailletaud G., Proudhon H., Mballa F.S.M., Noel S., Teste P., 2015. Three-level multi-scale modeling of electrical contacts sensitivity study and experimental validation. In: Electrical Contacts (Holm), 2015 IEEE 61st Holm Conference.
- [90] Zhu D., Hu Y., 2001. A computer program package for the prediction of EHL and mixed lubrication characteristics, friction, subsurface stresses and flash temperatures based on measured 3-D surface roughness. *Tribology Transactions* 44, 383.
- [91] Geubelle P.H., Rice J.R., 1995. A spectral method for three-dimensional elastodynamic fracture problems. *Journal of the Mechanics and Physics of Solids* 43, 1791.
- [92] Ranjith K., 105. Spectral formulation of the elastodynamic boundary integral equations for bi-material interfaces. *International Journal of Solids and Structures* 59, 29.
- [93] Kammer D.S., Yastrebov V.A., Spijker P., Molinari J.F., 2012. On the propagation of slip fronts at frictional interfaces. *Tribology Letters* 48, 27.

- [94] Yastrebov V.A., 2016. Sliding without slipping under Coulomb friction: opening waves and inversion of frictional force. *Tribology Letters* 62, 1.
- [95] Autumn K., Liang Y.A., Hsieh S.T., Zesch W., Chan W.P., Kenny T.W., Fearing R., Full R.J., 2000. Adhesive force of a single gecko foot-hair. *Nature* 405, 681.
- [96] Arzt E., Gorb S.N., Spolenak R., 2003. From micro to nano contacts in biological attachment devices. *Proceedings of the National Academy of Sciences of the United States of America* 100, 10603.
- [97] Varenberg M., Pugno N.M., Gorb S.N., 2010. Spatulate structures in biological fibrillar adhesion. *Soft Matter* 6, 3269.
- [98] Filippov A., Popov V.L., Gorb S.N., 2011. Shear induced adhesion: contact mechanics of biological spatula-like attachment devices. *Journal of Theoretical Biology* 276, 126.
- [99] Labonte D., Williams J.A., Federle W., 2014. Surface contact and design of fibrillar 'friction pads' in stick insects (*Carausius morosus*): mechanisms for large friction coefficients and negligible adhesion. *Journal of the Royal Society Interface* 11, 20140034.
- [100] Barthlott W., Neinhuis C., 1997. Purity of the sacred lotus, or escape from contamination in biological surfaces. *Planta* 202, 1.
- [101] Burton Z., Bhushan B., 2006. Surface characterization and adhesion and friction properties of hydrophobic leaf surfaces. *Ultramicroscopy* 106, 709.
- [102] Stempfle P., Brendle M., 2006. Tribological behaviour of nacre influence of the environment on the elementary wear processes. *Tribology International* 39, 1485.
- [103] Baum M.J., Kovalev A.E., Michels J., Gorb S.N., 2014. Anisotropic friction of the ventral scales in the snake *Lampropeltis getula californicae*. *Tribology Letters* 54, 139.
- [104] Dean B., Bhushan B., 2010. Shark-skin surfaces for fluid-drag reduction in turbulent flow: a review. *Philosophical Transactions of the Royal Society of London A: Mathematical, Physical and Engineering Sciences* 368, 4775.
- [105] Federle W., Barnes W.J., Baumgartner W., Drechsler P., Smith J.M., 2006. Wet but not slippery: boundary friction in tree frog adhesive toe pads. *Journal of the Royal Society Interface* 3, 689.
- [106] Prevost A., Scheibert J., Debregeas G., 2009. Effect of fingerprints orientation on skin vibrations during tactile exploration of textured surfaces. *Communicative & Integrative Biology* 2, 422.

- [107] Derler S., Gerhardt L., 2012. Tribology of skin: review and analysis of experimental results for the friction coefficient of human skin. *Tribology Letters* 45, 1.
- [108] Leyva-Mendivil M.F., Lengiewicz J., Page A., Bressloff N.W., Limbert G., 2017. Skin microstructure is a key contributor to its friction behaviour. *Tribology Letters* 65, 12.
- [109] Lakes R., 1993. Materials with structural hierarchy. *Nature* 361, 511.
- [110] Fratzl P., Weinkamer R., 2007. Nature's hierarchical materials. *Progress in Materials Science* 52, 1263.
- [111] Yurdumakan B., Raravikar N.R., Ajayan P.M., Dhinojwala A., 2005. Synthetic gecko foothairs from multiwalled carbon nanotubes. *Chemical Communications* 0, 3799.
- [112] Lee J., Bush B., Maboudian R., Fearing R.S., 2009. Gecko-inspired combined lamellar and nanofibrillar array for adhesion on nonplanar surface. *Langmuir* 25, 12449.
- [113] Singh A., Suh K., 2013. Biomimetic patterned surfaces for controllable friction in microand nanoscale devices. *Micro and Nano Systems Letters* 1, 6.
- [114] Murarash B., Itovich Y., Varenberg M., 2011. Tuning elastomer friction by hexagonal surface patterning. *Soft Matter* 7, 5553.
- [115] Li N., Xu E., Liu Z., Wang X., Liu L., 2016. Tuning apparent friction coefficient by controlled patterning bulk metallic glasses surfaces. *Scientific Reports* 6, 39388.
- [116] Borghi A., Gualtieri E., Marchetto D., Moretti L., Valeri S., 2008. Tribological effects of surface texturing on nitriding steel for high-performance engine applications. *Wear* 265, 1046.
- [117] Gualtieri E., Borghi A., Calabri L., Pugno N.M., Valeri S., 2009. Increasing nanohardness and reducing friction of nitride steel by laser surface texturing. *Tribology International* 42, 699.
- [118] Baum M.J., Heepe L., Fadeeva E., Gorb S.N., 2014. Dry friction of microstructured polymer surfaces inspired by snake skin. *Beilstein Journal of Nanotechnology* 5, 1091.
- [119] Maegawa S., Itoigawa F., Nakamura T., 2016. Effect of surface grooves on kinetic friction of a rubber slider. *Tribology International* 102, 326.
- [120] He B., Chen W., Wang Q.J., 2008. Surface texture effect on friction of a microtextured poly (dimethylsiloxane)(PDMS). *Tribology Letters* 31, 187.

- [121] Tay N.B., Minn M., Sinha S.K., 2011. A tribological study of SU-8 micro-dot patterns printed on Si surface in a flat-on-flat reciprocating sliding test. *Tribology Letters* 44, 167.
- [122] Greiner C., Schafer M., Popp U., Gumbsch P., 2014. Contact splitting and the effect of dimple depth on static friction of textured surfaces. *ACS Applied Materials and Interfaces* 6, 7986.
- [123] Giraud L., Bazin G., Giasson S., 2017. Lubrication with soft and hard two-dimensional colloidal arrays. *Langmuir* 33, 3610.
- [124] Capozza R., Fasolino A., Ferrario M., Vanossi A., 2008. Lubricated friction on nanopatterned surfaces via molecular dynamics simulations. *Physical Review B* 77, 235432.
- [125] Burridge R., Knopoff L., 1967. Model and theoretical seismicity. *Bulletin of the Seismological Society of America* 57, 341.
- [126] Capozza R., Pugno N.M., 2015. Effect of surface grooves on the static friction of an elastic slider. *Tribology Letters* 58, 35.
- [127] Costagliola G., Bosia F., Pugno N.M., 2016. Static and dynamic friction of hierarchical surfaces. *Physical Review E* 94, 063003.
- [128] Costagliola G., Bosia F., Pugno N.M., 2017. Hierarchical spring-block model for multiscale friction problems. *ACS Biomaterials Science and Engineering* 3, 2845.
- [129] Costagliola G., Bosia F., Pugno N.M., 2018. A 2-D model for friction of complex anisotropic surfaces. *Journal of the Mechanics and Physics of Solids* 112, 50.
- [130] Tromborg J.K., Sveinsson H.A., Scheibert J., Thogersen K., Amundsen D.S., Malthé-Sorensen A., 2014. Slow slip and the transition from fast to slow fronts in the rupture of frictional interfaces. *Proceedings of the National Academy of Sciences of the United States of America* 111, 8764.
- [131] Braun O.M., Barel I., Urbakh M., 2009. Dynamics of transition from static to kinetic friction. *Physical Review Letters* 103, 194301.
- [132] Amundsen D.S., Tromborg J.K., Thogersen K., Katzav E., Malthé-Sorensen A., Scheibert J., 2015. Steady-state propagation speed of rupture fronts along onedimensional frictional interfaces. *Physical Review E* 92, 032406.
- [133] Tromborg J.K., Sveinsson H.A., Thogersen K., Scheibert J., Malthé-Sorensen A., 2015. Speed of fast and slow rupture fronts along frictional interfaces. *Physical Review E* 92, 012408.

- [134] Maegawa S., Suzuki A., Nakano K., 2010. Precursors of global slip in a longitudinal line contact under non-uniform normal loading. *Tribology Letters* 38, 313.
- [135] Amundsen D.S., Scheibert J., Thogersen K., Tromborg J., Malthe-Sorensen A., 2012. 1D model of precursors to frictional stick-slip motion allowing for robust comparison with experiments. *Tribology Letters* 45, 357.
- [136] Braun O.M., Scheibert J., 2014. Propagation length of self-healing slip pulses at the onset of sliding: a toy model. *Tribology Letters* 56, 553.
- [137] Tromborg J., Scheibert J., Amundsen D.S., Thogersen K., Malthe-Sorensen A., 2011. Transition from static to kinetic friction: insights from a 2D model. *Physical Review Letters* 107, 074301.
- [138] Capozza R., Rubinstein S.M., Barel I., Urbakh M., Fineberg J., 2011. Stabilizing stick-slip friction. *Physical Review Letters* 107, 024301.
- [139] Pugno N.M., Yin Q., Shi X., Capozza R., 2013. A generalization of the Coulomb's friction law: from graphene to macroscale. *Meccanica* 48, 1845.
- [140] Rubinstein S.M., Cohen G., Fineberg J., 2004. Detachment fronts and the onset of dynamic friction. *Nature* 430, 1005.
- [141] Ben-David O., Rubinstein S.M., Fineberg J., 2010. Slip-stick and the evolution of frictional strength. *Nature* 463, 76.
- [142] Rubinstein S.M., Cohen G., Fineberg J., 2007. Dynamics of precursors to frictional sliding. *Physical Review Letters* 98, 226103.
- [143] Ben-David O., Cohen G., Fineberg J., 2010. The dynamics of the onset of frictional slip. *Science* 330, 211.
- [144] Svetlizky I., Fineberg J., 2014. Classical shear cracks drive the onset of dry frictional motion. *Nature* 509, 205.
- [145] Reynolds O., 1886. On the theory of lubrication and its application to Mr. Beauchamp Tower's experiments, including an experimental determination of the viscosity of olive oil. *Proceedings of the Royal Society of London* 40, 191.
- [146] Venner C.H., Lubrecht A.A., 2000. *Multi-Level Methods in Lubrication*. Elsevier, Amsterdam, The Netherlands.
- [147] Hamrock B.J., Schmid S.R., Jacobson B.O., 2004. *Fundamentals of Fluid Film Lubrication*. CRC Press, Cambridge, United Kingdom.
- [148] Gropper D., Wang L., Harvey T.J., 2016. Hydrodynamic lubrication of textured surfaces: a review of modeling techniques and key findings. *Tribology International* 94, 509.

- [149] Greiner C., Schafer M., 2015. Bio-inspired scale-like surface textures and their tribological properties. *Bioinspiration & Biomimetics* 10, 044001.
- [150] Elrod H.G., Adams M.L., 1974. A computer program for cavitation and starvation problems. Elsevier, Amsterdam, The Netherlands.
- [151] Elrod H.G., 1981. A cavitation algorithm. *Journal of Lubrication Technology, Transactions of ASME* 103, 350.
- [152] Jakobsson B., Floberg L., 1957. The finite journal bearing considering vaporization. *Transactions of Chalmers University of Technology* 90, 1.
- [153] Olsson K., 1957. Cavitation in dynamically loaded bearing. *Transactions of Chalmers University of Technology* 308, 1.
- [154] Braun M., Hannon W., 2010. Cavitation formation and modelling for fluid film bearings: a review. *Proceedings of the Institution of Mechanical Engineers, Part J: Journal of Engineering Tribology* 224, 839.
- [155] Sahlin F., Almqvist A., Larsson R., Glavatskih S., 2007. Rough surface flow factors in full film lubrication based on a homogenization technique. *Tribology International* 40, 1025.
- [156] Patir N., Cheng H., 1978. An average flow model for determining effects of threedimensional roughness on partial hydrodynamic lubrication. *Journal of Lubrication Technology, Transactions of ASME* 100, 12.
- [157] Elrod H., 1979. A general theory for laminar lubrication with Reynolds roughness. *Journal of Lubrication Technology, Transactions of ASME* 101, 8.
- [158] Tripp J., 1983. Surface roughness effects in hydrodynamic lubrication: the flow factor method. *Journal of Lubrication Technology, Transactions of ASME* 105, 458.
- [159] Scaraggi M., Carbone G., Persson B.N.J., Dini D., 2011. Lubrication in soft rough contacts: a novel homogenized approach. Part I-Theory. *Soft Matter* 7, 10395.
- [160] Miyoshi K., 2001. *Solid Lubrication - Fundamentals and Applications*. CRC Press, Cambridge, United Kingdom.
- [161] Wornyoh E.Y., Jasti V.K., Higgs C.F., 2007. A review of dry particulate lubrication: powder and granular materials. *Journal of Tribology, Transactions of ASME* 129, 438.
- [162] Jang J., Khonsari M., 2005. On the granular lubrication theory. *Proceedings of the Royal Society of London A: Mathematical, Physical and Engineering Sciences* 461, 3255.

- [163] Haff P., 1983. Grain flow as a fluid-mechanical phenomenon. *Journal of Fluid Mechanics, Transactions of ASME* 134, 401.
- [164] Lun C., Savage S.B., Jeffrey D., Chepurny N., 1984. Kinetic theories for granular flow: inelastic particles in Couette flow and slightly inelastic particles in a general flowfield. *Journal of Fluid Mechanics, Transactions of ASME* 140, 223.
- [165] Lun C., Savage S.B., 1987. A simple kinetic theory for granular flow of rough, inelastic, spherical particles. *Journal of Applied Mechanics, Transactions of ASME* 54, 47.
- [166] Iordanoff I., Berthier Y., Descartes S., Heshmat H., 2002. A review of recent approaches for modeling solid third bodies. *Journal of Tribology, Transactions of ASME* 124, 725.
- [167] Heshmat H., 1991. The rheology and hydrodynamics of dry powder lubrication. *Tribology Transactions* 34, 433.
- [168] Cundall P.A., Strack O.D.L., 1979. A discrete numerical model for granular assemblies. *Geotechnique* 29, 47.
- [169] Neukirchner J., 1980. Tribocorrosion and ways of prevention. *Maschinenbautechnik* 29, 313.
- [170] Ewen J.P., Heyes D.M., Dini D., 2018. Advances in nonequilibrium molecular dynamics simulations of lubricants and additives. *Friction* 6, 349.
- [171] Tower B., 1883. First report on friction experiments. *Proceedings of the Institution of Mechanical Engineers* 34, 632.
- [172] Grubin A., 1949. Fundamentals of the hydrodynamic theory of lubrication of heavily loaded cylindrical surfaces. In *Investigation on the Contact of Machine Components* 2, 115.
- [173] Cameron A., Wood W., 1949. The full journal bearing. *Proceedings of the Institution of Mechanical Engineers* 161, 59.
- [174] Dowson D., Higginson G., 1959. A numerical solution to the elasto-hydrodynamic problem. *Journal of Mechanical Engineering Sciences* 1, 6.
- [175] Dowson D., Higginson G., 1960. The effect of material properties on the lubrication of elastic rollers. *Journal of Mechanical Engineering Sciences* 2, 188.
- [176] Dowson D., Higginson G., Whitaker A., 1962. Elasto-hydrodynamic lubrication: a survey of isothermal solutions. *Journal of Mechanical Engineering Sciences* 4, 121.

- [177] Dowson D., Ehret P., 1999. Past, present and future studies in elastohydrodynamics. *Proceedings of the Institution of Mechanical Engineers, Part J: Journal of Engineering Tribology* 213, 317.
- [178] Hooke C. A review of the paper 'A numerical solution to the elastohydrodynamic problem' by D. Dowson and GR Higginson. *Proc Inst Mech Eng Part C* 2009;223: 4963.
- [179] Conry T., Wang S., Cusano C., 1987. A Reynolds-Eyring equation for elastohydrodynamic lubrication in line contacts. *Journal of Tribology, Transactions of ASME* 109, 648.
- [180] Gohar R., 2001. *Elastohydrodynamics*. World Scientific, London, United Kingdom.
- [181] Giacomini M., Fowell M.T., Dini D., Strozzi A., 2010. A mass-conserving complementarity formulation to study lubricant films in the presence of cavitation. *Journal of Tribology, Transactions of ASME* 132, 041702.
- [182] Bertocchi L., Dini D., Giacomini M., Fowell M.T., Baldini A., 2013. Fluid film lubrication in the presence of cavitation: a mass-conserving two-dimensional formulation for compressible, piezoviscous and non-Newtonian fluids. *Tribology International* 67, 61.
- [183] Woloszynski T., Podsiadlo P., Stachowiak G.W., 2015. Efficient solution to the cavitation problem in hydrodynamic lubrication. *Tribology International* 58, 18.
- [184] Tucker P., Keogh P., 1996. On the dynamic thermal state in a hydrodynamic bearing with a whirling journal using CFD techniques. *Journal of Tribology, Transactions of ASME* 118, 356.
- [185] Almqvist T., Larsson R., 2002. The NavierStokes approach for thermal EHL line contact solutions. *Tribology International* 35, 163.
- [186] Hartinger M., Dumont M., Ioannides S., Gosman D., Spikes H., 2008. CFD modeling of a thermal and shear-thinning elastohydrodynamic line contact. *Journal of Tribology, Transactions of ASME* 130, 041503.
- [187] Bruyere V., Fillot N., Morales-Espejel G.E., Vergne P., 2012. Computational fluid dynamics and full elasticity model for sliding line thermal elastohydrodynamic contacts. *Tribology International* 46, 3.
- [188] Hajishafiee A., Kadiric A., Ioannides S., Dini D., 2017. A coupled finite-volume CFD solver for two-dimensional elasto-hydrodynamic lubrication problems with particular application to rolling element bearings. *Tribology International* 109, 258.

- [189] Profito F.J., Giacomini M., Zachariadis D.C., Dini D., 2015. A general finite volume method for the solution of the Reynolds lubrication equation with a mass-conserving cavitation model. *Tribology Letters* 60, 18.
- [190] Profito F.J., Vladescu S., Reddyhoff T., Dini D., 2017. Transient experimental and modelling studies of laser-textured micro-grooved surfaces with a focus on piston-ring cylinder liner contacts. *Tribology International* 113, 125.
- [191] Deng M., Tan V., Tay T., 2004. Atomistic modeling: interfacial diffusion and adhesion of polycarbonate and silanes. *Polymer* 45, 6399.
- [192] Quddus M.A., Rojas O.J., Pasquinelli M.A., 2014. Molecular dynamics simulations of the adhesion of a thin annealed film of oleic acid onto crystalline cellulose. *Biomacromolecules* 15, 1476.
- [193] Gee R.H., Maiti A., Bastea S., Fried L.E., 2007. Molecular dynamics investigation of adhesion between TATB surfaces and amorphous fluoropolymers. *Macromolecules* 40, 3422.
- [194] Nikkhah S.J., Moghbeli M.R., Hashemianzadeh S.M., 2015. A molecular simulation study on the adhesion behavior of a functionalized polyethylene-functionalized graphene interface. *Physical Chemistry Chemical Physics* 17, 27414.
- [195] Xiaoqun W., Awan I.S., Guiyong C., Pengcheng H., Shanyi D., 2013. Molecular dynamics simulations of interfacial adhesion between carbon fibers and various epoxies/hardeners and its calorimetric validation. *Journal of Composite Materials* 47, 1011.
- [196] Suarez J., Miguel S., Pinilla P., Lopez F., 2008. Molecular dynamics simulation of polymermetal bonds. *Journal of Adhesion Science and Technology* 22, 1387.
- [197] Johnston K., Harmandaris V., 2013. Hierarchical multiscale modeling of polymersolid interfaces: atomistic to coarse-grained description and structural and conformational properties of polystyrenegold systems. *Macromolecules* 46, 5741.
- [198] Van Eijk M., Stuart M.C., Rovillard S., De Coninck J., 1998. Adsorption and spreading of polymers at plane interfaces; theory and molecular dynamics simulations. *The European Physical Journal B* 1, 233.
- [199] Bhasin A., Bommavaram R., Greenfield M.L., Little D.N., 2010. Use of molecular dynamics to investigate self-healing mechanisms in asphalt binders. *Journal of Materials in Civil Engineering* 23, 485.

- [200] Sun D., Lin T., Zhu X., Tian Y., Liu F., 2016. Indices for self-healing performance assessments based on molecular dynamics simulation of asphalt binders. *Computational Materials Science* 114, 86.
- [201] Liu W., Liu Y., Wang R., 2011. MD simulation of single-wall carbon nanotubes employed as container in self-healing materials. *Polymers & Polymer Composites* 19, 333.
- [202] Aliko-Benitez A., Doblare M., Sanz-Herrera J., 2015. Chemical-diffusive modeling of the self-healing behavior in concrete. *International Journal of Solids and Structures* 69, 392.
- [203] Bluhm J., Specht S., Schroder J., 2015. Modeling of self-healing effects in polymeric composites. *Archive of Applied Mechanics* 85, 1469.
- [204] Balazs A.C., 2007. Modeling self-healing materials. *Materials Today* 10, 18.
- [205] Bosia F., Abdalrahman T., Pugno N.M., 2014. Self-healing of hierarchical materials. *Langmuir* 30, 1123.
- [206] Bosia F., Merlino M., Pugno N.M., 2015. Fatigue of self-healing hierarchical soft nanomaterials: the case study of the tendon in sportsmen. *Journal of Materials Research* 30, 2.
- [207] Myshkin N., Kovalev A., 2018. Adhesion and surface forces in polymer tribology A review. *Friction* 6, 143.
- [208] Brostow W., Hinze J.A., Simoes R., 2004. Tribological behavior of polymers simulated by molecular dynamics. *Journal of Materials Research* 19, 851.
- [209] Yew Y.K., Minn M., Sinha S.K., Tan V.B.C., 2011. Molecular simulation of the frictional behavior of polymer-on-polymer sliding. *Langmuir* 27, 5891.
- [210] Davidson J.E., Hinchley S.L., Harris S.G., Parkin A., Parsons S., Tasker P.A., 2006. Molecular dynamics simulations to aid the rational design of organic friction modifiers. *Journal of Molecular Graphics and Modelling* 25, 495.
- [211] Ewen J.P., Echeverri Restrepo S., Morgan N., Dini D., 2017. Nonequilibrium molecular dynamics simulations of stearic acid adsorbed on iron surfaces with nanoscale roughness. *Tribology International* 107, 264.
- [212] Ewen J.P., Kannam S.K., Todd B.D., Dini D., 2018. Slip of alkanes confined between surfactant monolayers adsorbed on solid surfaces. *Langmuir* 34, 3864.

Chapter 3

Friction between laterally graded materials

3.1 Introduction

Materials with a gradient in their physical or elastic properties are widely found in Nature. Several known biological systems have developed specialized functionalities due to stiffness, density or composition gradients. Beetles, for instance, display setae with a graded stiffness that optimises the adhesive performance on rough surfaces [1]. Hardness and stiffness gradients are of fundamental importance in the biomechanics of contact, since they allow increased resistance against wear, impact, penetration and crack propagation [2-7]. Bio-inspired solutions have thus been proposed for the design of advanced materials that mimic the hierarchical and graded structures found in Nature, for use in engineering applications [8,9].

Functionally graded materials (FGMs) display a gradient in their elastic properties along one or more directions and have recently acquired great interest in technology [10]. Several authors have studied standard solid mechanics problems considering FGMs, for example, in the case of vari-

ous loading conditions [11-13], and in problems involving fracture [14-17] or fatigue [18].

Recently, FGMs have also been applied to tribological studies, where it is well known that the behaviour of a system is governed by multiphysics and multiscale interactions [19]. The first application of graded materials to contact mechanics was proposed by Giannakopoulos and Suresh, who presented an analytical study of the indentation of materials with an exponential or power law variation of the Young's modulus through the depth [20,21]. The same analysis was then extended to 2D [22]. Graded substrates have also been considered in elastohydrodynamic lubrication problems [23]. More recently, the method of dimensionality reduction [24,25] has been applied to the axisymmetric frictionless contact of elastically graded materials [26], and solutions are also provided in the presence of adhesion [27]. In all these cases, the elastic gradients are considered with respect to the depth, with an exponential or a power law variation of the Young's modulus, i.e., $E(z) = E_1 e^{\alpha z}$ or $E(z) = E_2 z^\beta$, respectively, where z is the depth coordinate and E_1 , E_2 , α and β are constants. The first extension to a lateral elastic gradient, to the best of our knowledge, was by Dag *et al.* who studied the problem both analytically, by reducing the equation describing the contact of a rigid flat punch to a singular integral equation, and numerically, through the finite-element method (FEM) [28,29].

In this Chapter, we extend a previous work on 1D composite surfaces [30] to 2D geometries to show how it is possible to tune the macroscopic tribological properties through local variations of material and surface properties, i.e., Young's moduli and friction coefficients, reducing static friction compared to the non-graded case. The results also allow the predictions of a discrete approach like the spring-block model [31,32] to be compared to those derived by explicit finite-element simulations. This provides useful

insights to understand the frictional properties of graded materials, with the aim of designing smart tribo-materials and innovative solutions for sliding interfaces.

3.2 Methods

3.2.1 Introduction

The system taken into consideration is composed of an elastic plate, with a square base of side L and height $H \ll L$, which is driven from the top surface at constant velocity over a rigid substrate and subjected to friction. We study this system by means of two numerical methods: a 2D spring-block model (SBM) and 3D FEM simulations. The two methods are complementary in many aspects, so that by using both it is possible to cross-check the results and obtain interesting insights from different approaches.

The SBM is a two-dimensional approximation of the real system, so that effects due to the thickness of the layer are neglected. Specifically, any effect due to the vertical stress distribution cannot be captured. While these can be minimized in the case $H \ll L$, it is still useful to compare the results with FEM simulations, which can model this thin layer while maintaining a 3D approach. As we will show later, the comparison between the two methods will allow some concurrent effects to be disentangled that govern the global frictional behaviour. On the other hand, different formulations of SBM have been used in many recent studies to describe aspects of the transition from static to dynamic friction, the nucleation of rupture wave fronts, and the effects of patterning [32-36]. The SBM method is usually computationally faster than FEM, thus it is more practical for a qualitative understanding of these phenomena, but also includes approximations that must be verified to check whether all effects are correctly described. Thus, in each Section, we

will consider the two models with the same setup, that is, by choosing the closest conditions and parameter sets for the two approaches, and we will describe the effects predicted by them in the presence of graded materials.

3.2.2 2D spring-block model

We adopt the formulation of the 2D SBM introduced in Costagliola *et al.* [32]. The sliding surface is discretised with $N_b = 120$ blocks in both the x and y directions, placed at a distance $l = L/N_b$. The thickness of the layer is set to l_z , so that the block mass is $m = \rho l_z l^2$, where ρ is the density of the material. The spring mesh is arranged as shown in Figure 3.1. In order to obtain the equivalent of a homogeneous elastic material with Young's modulus E and Poisson's ratio $1/3$, the stiffness of the springs along the axis is set to $K_{int} = 3/4 E l_z$, and of the diagonal springs to $K_{int}/2$ [37]. Thus, the internal elastic force exerted on the generic block i by its neighbour j is $\mathbf{F}_{int}^{(ij)} = k_{ij} (r_{ij} l_{ji}) (\mathbf{r}_j - \mathbf{r}_i) / r_{ij}$, where \mathbf{r}_i and \mathbf{r}_j are the position vectors of blocks i and j , respectively, r_{ij} is the modulus of their distance, l_{ij} is their rest distance and k_{ij} is the stiffness of the spring linking them.

All the blocks are connected to a slider, moving at constant velocity \mathbf{v} , through a spring with stiffness K_s . The force exerted on the block i by the slider is $\mathbf{F}_s^{(i)} = K_s (\mathbf{v}t + \mathbf{r}_i^0 - \mathbf{r}_i)$, where \mathbf{r}_i^0 is the initial position of the block and \mathbf{v} the velocity vector of the slider, e.g., $\mathbf{v} = (v, 0)$ when sliding is along the x axis. Therefore, the total driving force acting on the block i is $\mathbf{F}_{mot}^{(i)} = \mathbf{F}_s^{(i)} + \sum_j \mathbf{F}_{int}^{(ij)}$.

A damping force $\mathbf{F}_d^i = -m\gamma\dot{\mathbf{r}}_i$ is added to avoid artificial block oscillations, where γ is the damping coefficient and $\dot{\mathbf{r}}_i$ is the velocity vector of the block. γ is an arbitrary parameter and the results are independent of its value provided it is fixed in the underdamped regime, i.e., $\gamma < \sqrt{K_{int}/m}$ [34]. A pressure p is applied on the whole system, so that on each block there is

normal force $F_n^{(i)} = pl^2$. Hence, the total normal force is $F_n = pL^2$.

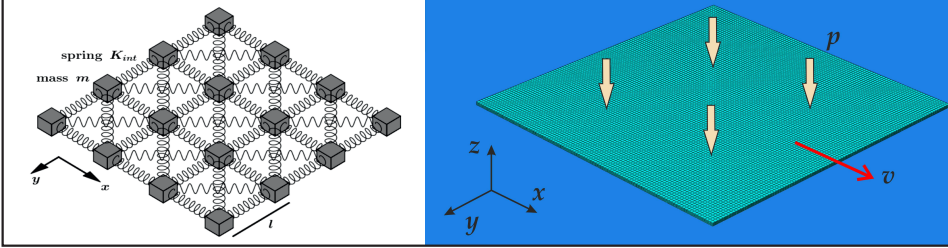


Figure 3.1: Schematic of the numerical models used in this work. Left: 2D discretization in springs and masses used in the SBM approach. Right: 3D discretization of a deformable plate (green) sliding on a rigid surface (blue), with applied normal pressure and velocity, used in the FEM approach.

The interaction between blocks and substrate is modelled through the classical Amontons-Coulomb's friction force: each block has a static $\mu_s^{(i)}$ and dynamic $\mu_k^{(i)}$ friction coefficient, randomly assigned at the beginning of the simulation from a Gaussian statistical distribution (to account, e.g., for surface roughness) with mean values denoted with $\mu_s^{(m)}$ and $\mu_k^{(m)}$, respectively. The standard deviation on the local coefficients of friction are denoted with σ_{μ_s} and σ_{μ_k} , respectively.

If the block i is at rest, the static friction force $\mathbf{F}_{fr}^{(i)}$ opposes the total driving force, so that $\mathbf{F}_{fr}^{(i)} = -\mathbf{F}_{mot}^{(i)}$, up to the threshold value $F_{fr}^{(i)} = \mu_s^{(i)} F_n^{(i)}$. When this threshold is exceeded, a constant dynamic friction force with modulus $F_{fr}^{(i)} = \mu_k^{(i)} F_n^{(i)}$ opposes the motion.

Thus, Newton's equation of motion for the block i can be written as:

$$m\ddot{\mathbf{x}}_i = \mathbf{F}_{mot}^{(i)} + \mathbf{F}_d^{(i)} + \mathbf{F}_{fr}^{(i)} \quad (3.1)$$

The overall system of equations is solved with a fourth-order Runge-Kutta algorithm. The simulation is repeated many times, extracting each time

new friction coefficients from the statistical distributions, for statistical reliability. An integration time step of 10^{-8} s is sufficient to reduce the time integration error under the statistical variability. Various observables can be calculated from the solution, for example, the total tangential force, which is the modulus of the sum of the forces exerted by the slider and corresponds to the macroscopic friction force $\mathbf{F}_{fr} = |\sum_i \mathbf{F}_s^{(i)}|$.

For further information and the discussions of the influence of the parameters, we refer the reader to the previous work [32].

3.2.3 3D finite-element model

3D explicit FEM simulations are carried out for a deformable plate sliding on a rigid flat surface. Each simulation is performed in two steps: first, a constant pressure is applied to the top surface of the block, increasing linearly from zero to the nominal value, in order to create the nominal area of contact; then, a constant velocity is applied instantaneously to the same top surface of the block. The rigid surface is fixed with a 3D clamp in order to constrain all its degrees of freedom. The complete setup is schematised in the same Figure 3.1.

The sliding block is discretised with 100 elements both in x and in y directions, and with 5 elements along the thickness, for a total of 50000 hexahedral elements. The simulations are performed using Abaqus[®] (version 6.13, Dassault Systèmes SE, France) and employing C3D8I elements, which are 8-node bricks with 8 points of integration and incompatible modes. The choice of this element type allows a good representation of the stress singularities at the edges (see Appendix A). A convergence study is carried out by monitoring the total strain energy of the system, to choose a sufficiently fine discretization.

We assign a velocity-dependent coefficient of friction to the contact surfaces, evolving as:

$$\mu(v) = \mu_{k,i} + (\mu_{s,i} - \mu_{k,i}) e^{-v/v_c} \quad (3.2)$$

where $\mu_{s,i}$ and $\mu_{k,i}$ are the static and dynamic local friction coefficients, respectively, v is the sliding velocity, and v_c is the critical velocity for the transition [38]. This expression ensures that the value of the dynamic coefficient of friction is reached only when the sliding velocity is sufficiently high (i.e., $v \gg v_c$). The static friction threshold is retrieved for $v = 0$, so that the friction force approximates the classical Amontons-Coulomb's friction force adopted in the SBM model. The contact between the block and the rigid surface is implemented through a surface-to-surface formulation using the penalty contact method [39]. Here, as opposed to the SBM, the local coefficient of friction is constant over the corresponding contact area and no statistical dispersion is introduced. The global coefficients of friction are finally calculated by dividing the resulting total lateral force by the applied normal force.

3.2.4 System parameters

We consider an elastic plate sliding on a rigid flat surface. The block has a square area of side $L = 5$ mm and thickness $H = 0.05$ mm. We consider a linear elastic material, with density $\rho = 1.2$ g cm⁻³, Poisson's ratio 1/3 and a reference Young's modulus $E = 10$ MPa (i.e., the reference value around which the gradients are implemented). We adopt typical values for the applied pressure of $p = 10$ kPa and for the sliding velocity $v = 1$ mm s⁻¹, keeping their value constant for all the simulations.

The reference values of the local static and dynamic coefficients of friction

are $\mu_{s,i} = 1.0$ and $\mu_{k,i} = 0.6$, respectively. In the SBM model, these are the mean values of the Gaussian distribution, i.e., $\mu_s^{(m)}$ and $\mu_k^{(m)}$, respectively.

In Figure 3.2, we show the typical time evolution of the tangential force obtained with the SBM for various σ_{μ_s} . The maximum of the friction force decreases when increasing the statistical dispersion, as in the case of the 1D formulation [30]. The time evolution obtained with FEM is also shown. In this case, the behaviour is strongly dependent on the thickness of the block. The time interval Δt_s needed to reach the static friction peak can be estimated starting from the shear stress $\tau = G\gamma$, where G is the shear modulus. If the shear deformation is $\gamma = v\Delta t_s/H$, the static friction peak is reached when $\tau L^2 = \mu_s p L^2$, i.e., after a time interval:

$$\Delta t_s = \mu_s p \frac{H}{Gv} \quad (3.3)$$

Simulations indicate that with a standard deviation of $\sigma_{\mu_s} = 2.8\%$ a thickness $l = 0.057$ mm and $H = 0.05$ mm, SBM and FEM results coincide in the case of a uniform non-graded surface. This parameter set is the reference case for the following comparisons.

We thus investigate the effects due to a grading of the material properties. Denoting a generic material property with ϕ , the corresponding linear gradient is described by:

$$\phi(x) = \phi_0 \left[1 + \Delta \left(\frac{2x}{L} - 1 \right) \right] \quad (3.4)$$

where ϕ_0 is the reference value (i.e., relative to the non-graded system) and Δ is the maximum variation at the edge. Discretizing the length into N homogeneous parts, Equation (3.4) can be written as:

$$\phi_i = \phi_0 \left[1 + \Delta \left(\frac{2i}{N-1} - 1 \right) \right] \quad (3.5)$$

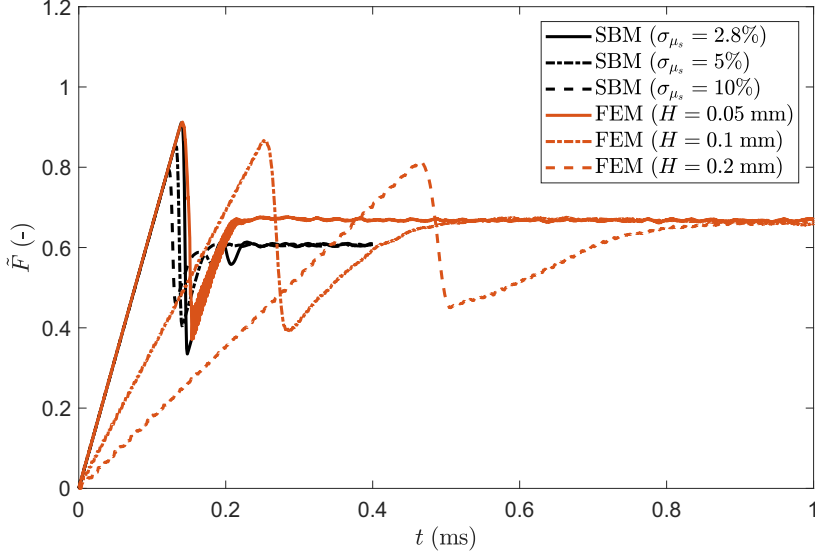


Figure 3.2: Dimensionless friction force as function of time for the non-graded material: SBM solution for different values of dispersion σ_{μ_s} of the local static coefficient of friction (black lines) and FEM solution for different block thicknesses H (red lines).

Therefore, the linear gradient is approximated with a stepwise function. For simplicity, we study a linear gradient instead of the power-law variation usually considered in the literature (see, e.g., [20,22]). This does not entail any loss of generality, since, as discussed below, the macroscopic frictional behaviour is determined mainly by the overall variation in the considered property between the edges and the centre of the plate.

In addition, we also consider triangular gradients, which are described by:

$$\phi_i = \phi_0 \left[1 + \Delta \left(1 - 2 \left| \frac{2i}{N-1} - 1 \right| \right) \right] \quad (3.6)$$

This gradient is therefore positive when ϕ is larger at the centre and negative when ϕ is larger at the borders. Figure 3.3 shows examples of the considered

stepwise linearly increasing and triangular property gradients.

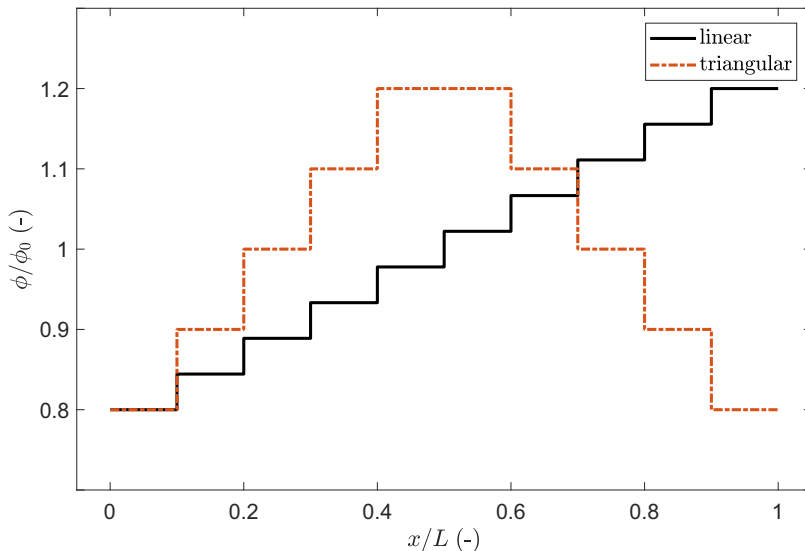


Figure 3.3: Examples of stepwise linearly increasing and triangular property gradients considered in this work for the case $\Delta = 0.2$.

For convenience, the gradients are implemented for $N = 10$, so that the surface is actually divided into bands perpendicular to the x axis. Simulations with the SBM indicate that the results were relatively insensitive to N , including in the case $N = N_b$, since small variations due to a very fine discretization are concealed by the statistical dispersion of the local friction coefficients. A reduced influence of N is also found in the FEM simulations, which are much more sensitive to the variation of the overall gradient (i.e., Δ), than to the discretization step. Thus, in each region of the gradient discretization, the value ϕ_i is assumed constant and the model parameters are defined according the general definitions given above.

3.3 Results and discussion

3.3.1 Gradients in the local coefficients of friction

We first consider a gradient in the local friction coefficients. In real systems, this can be realised in two ways. First, the surface can be polished in a spatially variable manner or using different processes in order to have a varying roughness and thus varying local friction coefficients. Secondly, a surface with a gradient in the frictional properties can be obtained by appropriately fabricating and arranging microscopic structures of variable geometries or sizes, giving rise to variable local friction coefficients [40,41]. In order to compare the results, we report the variations of the global static coefficient of friction as function of a grading distribution Δ in the local coefficient of friction, with respect to the value of the non-graded surface, using both SBM and FEM. The variation is computed as $\tilde{\mu}_s = (\mu_s - \mu_{s,0}) / \mu_{s,0}$, where $\mu_{s,0}$ corresponds to the case $\Delta = 0$. The absolute values of μ_s are reported in Appendix A.

The results are shown in Figure 3.4 for both SBM and FEM simulations. In general, in the presence of a gradient, the global static coefficient of friction of the surfaces in contact decreases with respect to the non-graded surface, although the mean values of the local friction coefficients are the same.

The reason for this lies in the progressive detachment of the contact surfaces, always starting from the side where the critical value of the local shear stress is reached (i.e., the static friction threshold). The first detachment of the sliding surface produces a detachment avalanche propagating towards the region with larger static friction threshold, as shown in Figure 3.5. Analogous effects on the propagation of detachment fronts have also been studied

experimentally [42]. Consequently, an increasing absolute value of Δ reduces the global static coefficient of friction with respect to the non-graded surface, up to an asymptotic value corresponding to the dynamic friction coefficient value. Thus, the gradient can completely remove the force peak observed at the transition from static to dynamic friction (see Figure 3.2). This is schematically shown in Figure 3.6, where the time evolution of the friction force is reported for two different values of Δ . An additional effect is the deviation from linearity when approaching the static friction threshold, observed for the largest value of the gradient (i.e., $\Delta = 0.4$) and similarly highlighted by both the SBM and the FEM simulations.

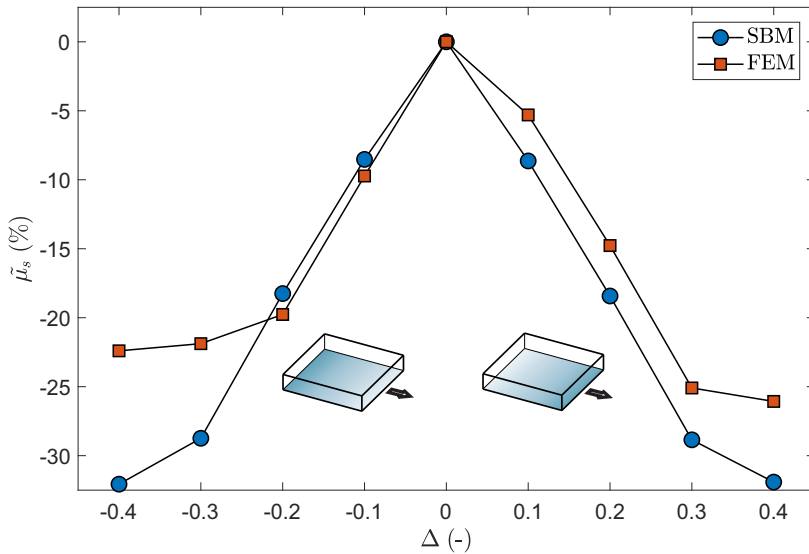


Figure 3.4: Effect of a gradient in the local coefficients of friction on the global static coefficient of friction, expressed as percentage variation as a function of Δ . The shaded blocks schematically represent the values of the local coefficients of friction, which are larger for a darker shading.

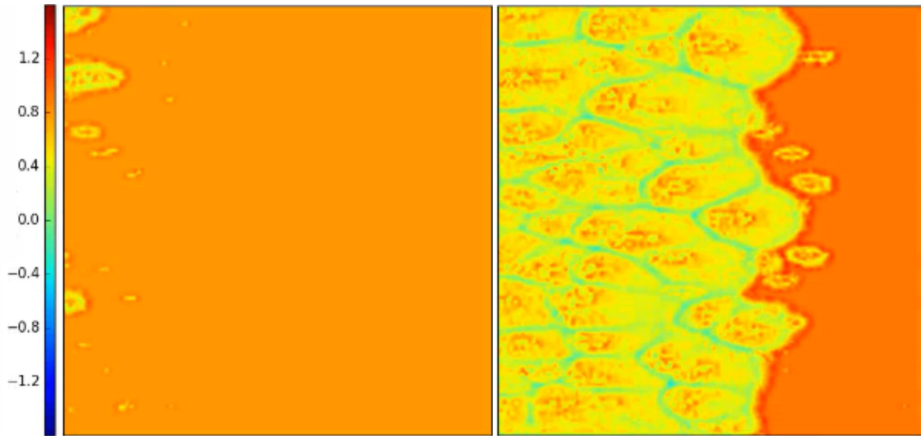


Figure 3.5: Propagation of the detachment front at the static friction threshold (left) and immediately after (right), in units of the dimensionless longitudinal stress σ_x/p , for a surface with a gradient in the local coefficients of friction, computed using the SBM method for the case $\Delta = 0.1$. The irregularities of the detachment front are due to the statistical dispersion of the local coefficients of friction introduced in the SBM formulation.

Unlike the SBM simulations, which give symmetric results with respect to the case $\Delta = 0$ since they are insensitive to the vertical stress distribution, FEM simulations display an anisotropic behaviour when considering a positive or a negative gradient. This is equivalent to considering the same sign of the gradient but with an opposite sliding direction. This result can be attributed to the vertical stress distribution at the contact interface: when friction is present, the normal pressure is reduced at the leading edge of the sliding plate and increased at the trailing edge [28,43,44]. Since the static friction thresholds depend not only on the local μ_s but also on the local value of the normal pressure, due to this effect, a gradient of detach-

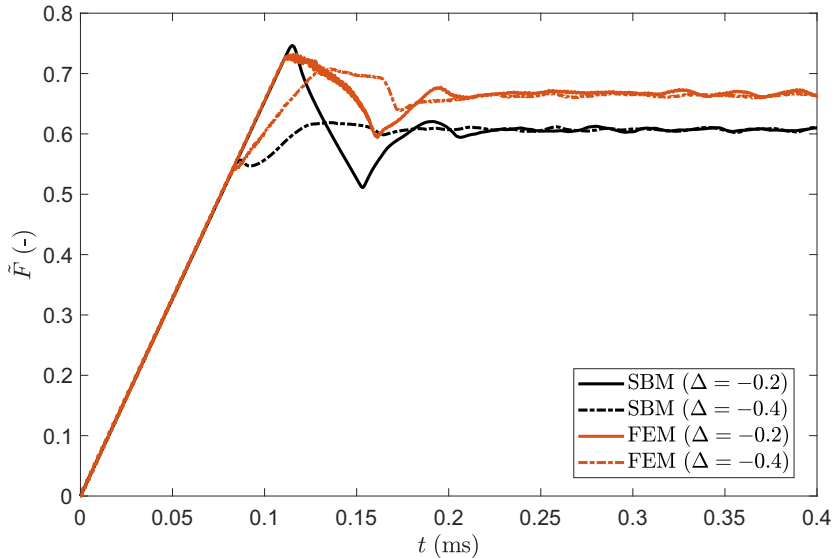


Figure 3.6: Dimensionless friction force as function of time for two values of Δ , calculated using the SBM and FEM methods. In both cases a larger value of Δ leads to the reduction or elimination of the initial force peak.

ment threshold already exists. This must be added to the gradient of the local coefficients of friction. As an example, for $\Delta > 0$, the static friction thresholds are increased at the leading edge of the surface, so that the effect of the vertical stress acts as a counterbalance, and the effective gradient is smaller than Δ . Conversely, for $\Delta < 0$, the vertical stress accumulates with the gradient. For this reason, with the same absolute value but different sign of Δ , we can expect a different behaviour; in particular, that for a positive Δ value, the global static friction is greater than for the case of a negative Δ value.

From the results of the FEM simulations, this is reproduced correctly at least for $\Delta < 0.3$, as can be seen in Figure 3.4. For higher values of the gra-

dient, the results are opposite due to the large difference of friction between the edges. For $\Delta < 0$ at the leading edge of the surface, static friction is already weak so that the effect of normal pressure reduction is less influential, while at the trailing edge, static friction is large due to the combination of a large local friction coefficient and increased pressure. The result is that the detachment process is inhibited with respect to the same positive Δ value.

The effect of larger values of Δ on the detachment process is also investigated through the SBM method. As previously explained, the detachment front nucleates from the edge where the weakest thresholds are, and the maximum of the friction force during the time evolution occurs shortly after the detachment begins. However, when the gradient increases, the time necessary for the detachment front to propagate across the surface increases as well (see Figure 3.6). For larger values of Δ , the contribution to the total friction force from the region with higher thresholds is more influential, so that the maximum of the friction force occurs later during the detachment process and not shortly after its beginning.

Thus, while SBM cannot capture anisotropic behaviour emerging from 3D deformation effects occurring in the materials in contact, it is still useful to disentangle the effects of the gradient and the vertical stress distribution.

The global dynamic friction coefficient μ_k does not display any appreciable variation when calculated with FEM or SBM if compared to the flat surface, i.e., its variation is limited to within 1% as shown in Figure 3.7. Again, the FEM results are anisotropic with respect to Δ , for the reasons explained above. However, the effect of the gradient on the dynamic friction cannot be fully captured by a formulation only based on the Amontons-Coulomb's friction law, as in the case of the SBM. Therefore, a good match between the two methods cannot be achieved here and further investigations are needed.

We have also investigated the effect of changing the sliding direction with respect to the direction of the gradient, as shown in Figure 3.8. Both the SBM and the FEM predict a greater global static coefficient of friction when switching from the 0° to the 90° direction, and this is evident especially for large values of Δ . The dependence of μ_s on the angle, instead, is more complex for $\Delta < 0.3$, especially for the 3D FEM, where the interaction with the vertical stress distribution must also be taken into account, as discussed previously.

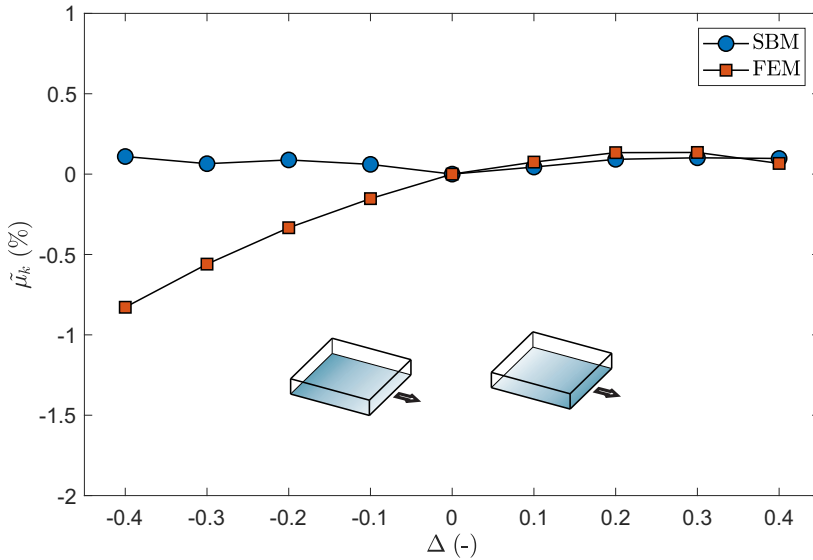


Figure 3.7: Effect of a gradient in the local coefficients of friction on the global dynamic coefficient of friction, expressed as percentage variation as a function of Δ . The shaded blocks schematically represent the value of the local coefficients of friction, which are larger for darker shading.

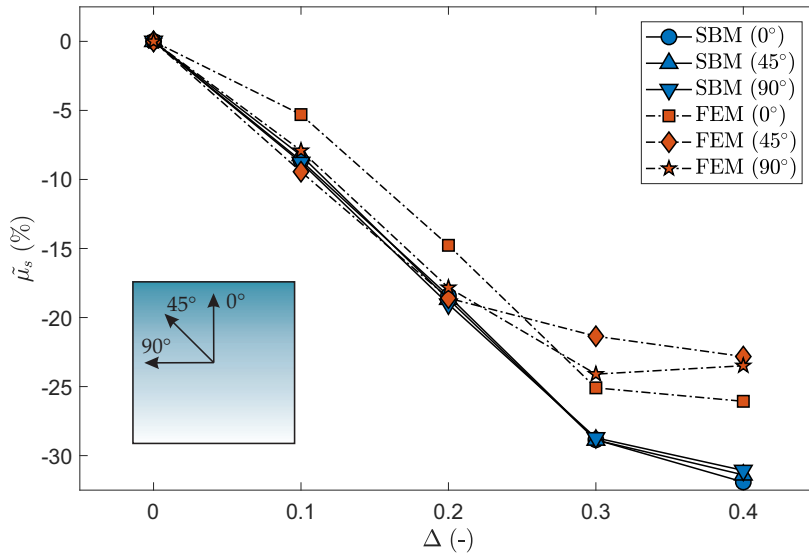


Figure 3.8: Effect of a gradient in the local coefficients of friction on the global static coefficient of friction, expressed as percentage variation as a function of Δ and for three sliding directions. The shaded square schematically represents the value of the local coefficients of friction, which are larger for a darker shading, and the considered sliding directions.

3.3.2 Gradients in the material Young's modulus

The effect of a gradient in the Young's modulus is qualitatively similar to that of the graded coefficient of friction discussed above. As can be seen in Figure 3.9, the global μ_s for the graded material is smaller than that for the case $\Delta = 0$. However, while in the previous case, the reason for the modification of the global friction coefficient can be found in a smaller static friction threshold, in this case, a given lateral strain produces a corresponding tangential force that is greater on the side of the material with greater local Young's modulus. Therefore, in this case, the static friction threshold

is reached first where the Young's modulus is greater. The detachment of the contact surfaces starts from this side and proceeds towards the region with smaller E , with a propagation similar to that already shown in Figure 5, but in the opposite direction. Thus, the material portion of the sliding plate is in tension for $\Delta > 0$ and in compression for $\Delta < 0$. Qualitatively speaking, a positive gradient in the Young's modulus is equivalent to a negative gradient in the local coefficients of friction.

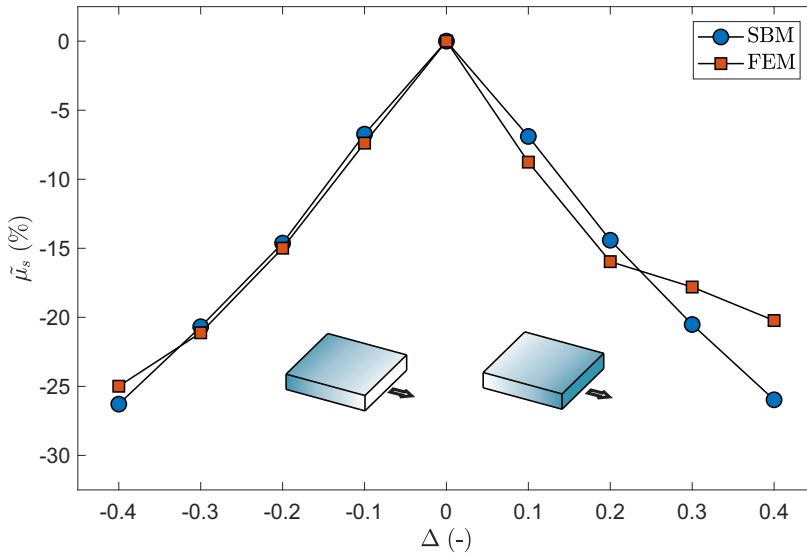


Figure 3.9: Effect of a gradient in the Young's modulus on the global static coefficient of friction, expressed as variation as function of Δ . The shaded blocks schematically represent the value of the local Young's modulus, which is larger for darker shading.

Again, FEM simulations produce anisotropic results with respect to positive and negative gradients, for the reasons discussed above. The redistribu-

bution of normal stresses is again related to the static friction threshold: when $\Delta > 0$, the tangential force is greater at the leading edge of the slider, where E is higher and the thresholds are reduced due to smaller p values, so that the effective gradient is larger than Δ . Conversely, for $\Delta < 0$ the gradient of the Young's modulus is counterbalanced by the effect due to the vertical stress. Thus, for small values of $|\Delta|$, a larger global μ_s is observed for $\Delta < 0$, while for larger values of $|\Delta|$, this trend is inverted due to the mechanism described previously.

It is remarkable that for $\Delta < 0$, the FEM and SBM simulations predict a very similar behaviour, suggesting that, in this case, two opposite effects are almost cancelled, so that the 2D SBM results provide a good approximation of real values. Although in the previous case the interplay of effects produced a nontrivial behaviour by varying the gradient, in this case, for $\Delta < 0$, the agreement between FEM and SBM simulations suggests that the reduction of the global static friction with the gradient is approximately linear.

The interplay of effects between the grading and the vertical stress distribution, which are both asymmetric with respect to the sliding direction, causes a non-trivial behaviour of the static friction as a function Δ . The effect of the vertical stress distribution can be reduced by designing a triangular grading, according to Equation 5, so that for $\Delta > 0$ the detachment begins at the centre of the surface and propagates towards the edges, and *vice versa* for $\Delta < 0$.

As in the previous case, no appreciable variation in the dynamic coefficient of friction is predicted, as shown in Figure 3.10. One difference is that both the SBM and the FEM simulations predict a larger global μ_k with respect to the case of non-graded materials. Again, the FEM results are slightly anisotropic as function of Δ and, as in Figure 3.7, a smaller global dynamic

coefficient of friction is obtained for $\Delta < 0$.

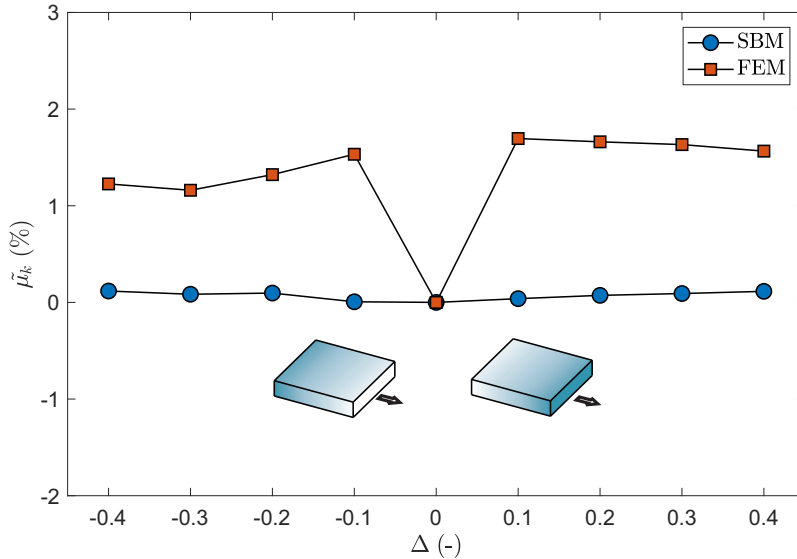


Figure 3.10: Effect of a gradient in the Young's modulus on the global dynamic coefficient of friction, expressed as percentage variation as a function of Δ . The shaded blocks represent schematically the value of the Young's modulus, which is larger for a darker shading.

The results presented in Figure 3.11 show the effect of a triangular gradient in the Young's modulus on the global static coefficient of friction calculated via SBM and FEM. The SBM results display a symmetric behaviour. The corresponding detachment process is shown, as example, in Figure 3.12. The FEM simulations predict a smaller μ_s in the case of $\Delta < 0$ because the effect due to the grading is superimposed on the effect of the vertical stress, so that the static friction thresholds are exceeded earlier compared to the case $\Delta > 0$. However, in both cases, the static friction

decreases approximately linearly with Δ .

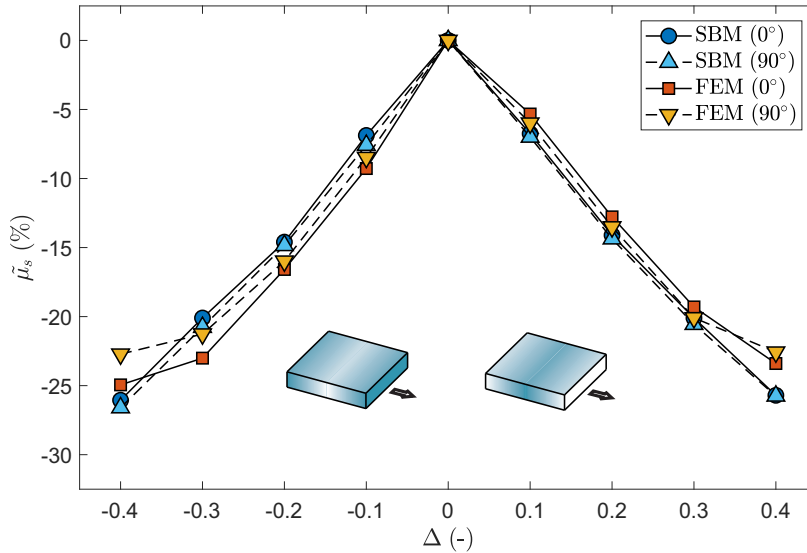


Figure 3.11: Effect of a triangular gradient in the Young's modulus on the global static coefficient of friction, expressed as variation as function of Δ and for two sliding directions (0° , i.e., parallel, and 90° , i.e., perpendicular to the gradient). The shaded blocks represent schematically the value of the local Young's modulus, which is larger for darker shading.

When considering the 90° sliding direction, i.e., orthogonal to the grading, the results of the SBM and the FEM simulations are in good agreement. In this case, the effects due to the vertical stress are influential, since the detachment process is symmetric with respect to the sliding direction. This suggests that with a proper combination of grading and sliding direction, it is possible to obtain a linear reduction of the static friction with the grading level, which would allow the global static friction of a surface to be conve-

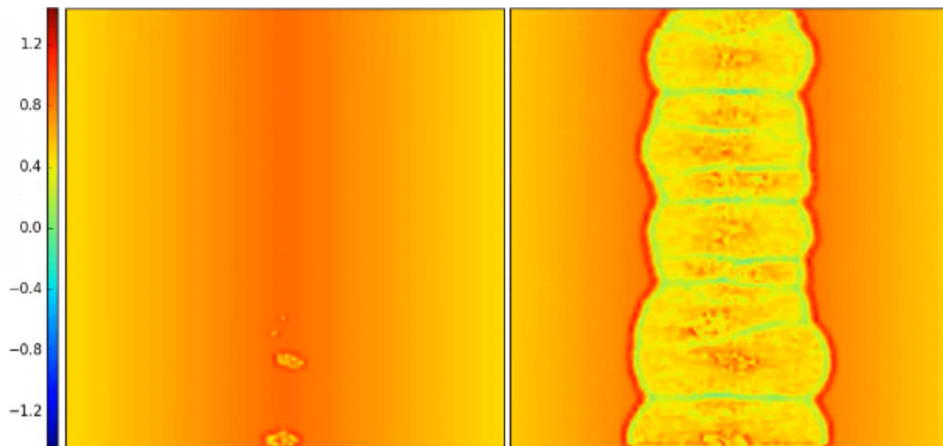


Figure 3.12: Propagation of the detachment front at the static friction threshold (left) and immediately after (right), in units of the dimensionless longitudinal stress σ_x/p , for a material with a triangular gradient in the Young's modulus, computed using the SBM method for the case $\Delta = 0.2$. The irregularities of the detachment front are due to the statistical dispersion of the local coefficients of friction introduced in the SBM formulation.

niently tuned to a chosen value, reduced with respect to the corresponding non-graded surface.

3.4 Conclusions

In this Chapter, we have considered the frictional sliding over a rigid substrate of an elastic material characterized by a grading of selected mechanical properties (i.e., the Young's modulus and the local coefficients of friction), focusing on the effects on the global static friction and the detachment process at the onset of sliding. The system has been investigated by means of numerical simulations using 2D SBM and 3D FEM to verify the results and to exploit additional insights provided by the two different approaches, after having tuned the SBM parameters in order to have a precise match

of the frictional force curve obtained by FEM, in terms of slope and static friction threshold.

The results show that grading of the mechanical properties can reduce the global static friction with respect to a non-graded material, due to an anticipated detachment process. In the case of a graded distribution of local friction coefficients, detachment begins from the region where thresholds on static friction are smaller, while in the case of a graded Young's modulus distribution, detachment begins from the regions where it is larger. In both cases, the 2D SBM predicts a linear decrease of the global coefficient of friction as a function of the relative grading variation and symmetry with respect to the sliding direction. In contrast, FEM simulations display an anisotropic behaviour due to the effect of the vertical stress distribution, which can either enhance or counterbalance the effect of the grading. Thus, a greater reduction of static friction can be expected when the grading on local friction decreases along the sliding direction, or when a grading of Young's modulus increases along the sliding direction. The effect on the global dynamic coefficient of friction, instead, appears to be underestimated numerically, and should be the object of further investigations.

These results are not valid when the relative grading variation is greater than 30% with respect to the average. In this case, the time evolution of the tangential force changes radically. The time duration of the detachment phase increases due to the large variation between edges so that the force peak in the transition from static to dynamic friction can disappear completely.

This interplay of effects produces a nonlinear reduction of static friction with the grading. A quasi-linear decrease can be obtained in the case of a triangular grading, which is symmetric with respect to the two edges, so that the anisotropy of the vertical stress distribution is less influential. In

particular, this outcome can be achieved by setting this type of grading along the orthogonal direction with respect to the sliding direction.

We have thus found that the SBM can capture the main effects of gradings on the static friction coefficient and describe the detachment process at the interface, with a much smaller computational cost than that required by FEM simulations. Therefore, it can be adopted for a rapid, initial estimation of static friction values.

These results suggest that it is possible to realize bio-inspired materials with a gradient in the mechanical properties, imitating the graded Young's moduli found in Nature, or in the local frictional properties, e.g., by controlling the roughness or the microstructure, for the design of advanced sliding interfaces. A reduction in the static friction up to almost 30%, with respect to the corresponding non-graded material, can thus be achieved.

References

- [1] Peisker H., Michels J., Gorb S.N., 2013. Evidence for a material gradient in the adhesive tarsal setae of the ladybird beetle *Coccinella septempunctata*. *Nature Communications* 4, 1661.
- [2] Matsumura Y., Kovalev A.E., Filippov A.E., Gorb S.N., 2017. Surface-contacts during mating in beetles: Stiffness gradient of the beetle penis facilitates propulsion in the spiraled female spermathecal duct. In: Gorb S.N., Gorb E. (eds) *Functional Surfaces in Biology III. Biologically-Inspired Systems*, vol. 10 Springer, Cham, Germany.
- [3] Bar-On B., Barth F.G., Fratzl P., Politi Y., 2014. Multiscale structural gradients enhance the biomechanical functionality of the spider fang. *Nature Communications* 5, 3894.
- [4] Marcus M.A., Amini S., Stiffler C.A., Sun C.Y., Tamura N., Bechtel H.A., Parkinson D.Y., Barnard H.S., Zhang X.X.X., Chua J.Q.I., Miserez A., Gilbert P.U.P.A., 2017. Parrotfish teeth: Stiff biominerals whose microstructure makes them tough and abrasion-resistant to bite stony corals. *ACS Nano* 11, 11856.

- [5] An B., Wang R., Arola D., Zhang D., 2012. The role of property gradients on the mechanical behavior of human enamel. *Journal of the Mechanical Behavior of Biomedical Materials* 9, 63.
- [6] Bentov S., Zaslansky P., Al-Sawalmih A., Masic A., Fratzl P., Sagi A., Berman A., Aichmayer B., 2012. Enamel-like apatite crown covering amorphous mineral in a crayfish mandible. *Nature Communications* 3, 839.
- [7] Liu Z., Zhu Y., Jiao D., Weng Z., Zhang Z., Ritchie R.O., 2016. Enhanced protective role in materials with gradient structural orientations: Lessons from Nature. *Acta Biomaterialia* 44, 31.
- [8] Liu Z., Meyers M.A., Zhang Z., Ritchie R.O., 2017. Functional gradients and heterogeneities in biological materials: Design principles, functions, and bioinspired applications. *Progress in Materials Science* 88, 467.
- [9] Zhao Z.L., Shu T., Feng Q.T., 2016. Study of biomechanical, anatomical, and physiological properties of scorpion stingers for developing biomimetic materials. *Materials Science and Engineering C* 58, 1112.
- [10] Suresh S., 2001. Graded materials for resistance to contact deformation and damage. *Science* 292, 2447.
- [11] Chi S.H., Chung Y.L., 2006. Mechanical behavior of functionally graded material plates under transverse load Part I: Analysis. *International Journal of Solids and Structures* 43, 3657.
- [12] Carpinteri A., Pugno N.M., 2006. Thermal loading in multi-layered and/or functionally graded materials: Residual stress field, delamination, fatigue and related size effects. *International Journal of Solids and Structures* 43, 828.
- [13] Carpinteri A., Pugno N.M., 2009. Extension of the de Saint Venant and Kirchhoff theories to functionally graded materials. *Strength, Fracture and Complexity* 5, 53.
- [14] Erdogan F., 1995. Fracture mechanics of functionally graded materials. *Composites Engineering* 5, 753.
- [15] Jin Z.H., Batra L.C., 1996. Some basic fracture mechanics concepts in functionally graded materials. *Journal of the Mechanics and Physics of Solids* 44, 1221.
- [16] Yildirim B., Dag S., Erdogan F., 2005. Three dimensional fracture analysis of FGM coatings under thermomechanical loading. *International Journal of Fracture* 132, 371.
- [17] Carpinteri A., Pugno N.M., 2006. Cracks and re-entrant corners in functionally graded materials. *Engineering Fracture Mechanics* 73, 1279.

- [18] Carpinteri A., Paggi M., Pugno N.M., 2006. An analytical approach for fracture and fatigue in functionally graded materials. *International Journal of Fracture* 141, 535.
- [19] Vakis A.I., Yastrebov V.A., Scheibert J., Minfray C., Nicola L., Dini D., Almqvist A., Paggi M., Lee S., Limbert G., Molinari J.F., Aghababaei R., Echeverri Restrepo S., Papangelo A., Cammarata A., Nicolini P., Putignano C., Carbone G., Stupkiewicz S., Lengiewicz J., Costagliola G., Bosia F., Guarino R., Pugno N.M., Mser M.H., Ciavarella M., 2018. Modeling and simulation for tribology across scales: An overview. *Tribology International* 125, 169.
- [20] Giannakopoulos A.E., Suresh S., 1997. Indentation of solids with gradients in elastic properties: Part I. Point force. *International Journal of Solids and Structures* 34, 2357.
- [21] Giannakopoulos A.E., Suresh S., 1997. Indentation of solids with gradients in elastic properties: Part II. Axisymmetric indentors. *International Journal of Solids and Structures* 34, 2393.
- [22] Giannakopoulos A.E., Pallot P., 2000. Two-dimensional contact analysis of elastic graded materials. *Journal of the Mechanics and Physics of Solids* 48, 1597.
- [23] Virdee S.S., Wang F.C., Xu H., Jin Z.M., 2003. Elastohydrodynamic lubrication analysis of a functionally graded layered bearing surface, with particular reference to 'cushion form bearings' for artificial knee joints. *Proceedings of the Institution of Mechanical Engineers, Part H: Journal of Engineering in Medicine* 217, 191.
- [24] Popov V.L., Hess M., 2015. *Method of Dimensionality Reduction in Contact Mechanics and Friction*. Springer, Berlin, Germany.
- [25] Hess M., Popov V.L., 2016. Method of dimensionality reduction in contact mechanics and friction: A users handbook. II. Power-Law graded materials. *Facta Universitatis, Series: Mechanical Engineering* 14, 251.
- [26] Hess M., 2016. A simple method for solving adhesive and non-adhesive axisymmetric contact problems of elastically graded materials. *International Journal of Engineering Science* 104, 20.
- [27] Popov V.L., 2018. Contact properties and adhesion of incompressible power-law gradient media with high gradients. *Physical Mesomechanics* 21, 76.
- [28] Dag S., Guler M.A., Yildirim B., Ozatag A.C., 2009. Sliding frictional contact between a rigid punch and a laterally graded elastic medium. *International Journal of Solids and Structures* 46, 4038.

- [29] Dag S., Guler M.A., Yildirim B., Ozatag A.C., 2013. Frictional Hertzian contact between a laterally graded elastic medium and a rigid circular stamp. *Acta Mechanica* 224, 1773.
- [30] Costagliola G., Bosia F., Pugno N.M., 2017. Tuning friction with composite hierarchical surfaces. *Tribology International* 115, 261.
- [31] Costagliola G., Bosia F., Pugno N.M., 2016. Static and dynamic friction of hierarchical surfaces. *Physical Review E* 94, 063003.
- [32] Costagliola G., Bosia F., Pugno N.M., 2018. A 2-D model for friction of complex anisotropic surfaces. *Journal of the Mechanics and Physics of Solids* 112, 50.
- [33] Braun O.M., Barel I., Urbakh M., 2009. Dynamics of transition from static to dynamic friction. *Physical Review Letters* 103, 194301.
- [34] Trømborg J.K., Scheibert J., Amundsen D.S., Thøgersen K., Malthe-Sørensen A., 2011. Transition from static to dynamic friction: Insights from a 2D model. *Physical Review Letters* 107, 074301.
- [35] Pugno N.M., Yin Q., Shi X., Capozza R., 2013. A generalization of the Coulombs friction law: from graphene to macroscale. *Meccanica* 48, 8.
- [36] Trømborg J.K., Sveinsson H.A., Scheibert J., Thøgersen K., Amundsen D.S., Malthe-Sørensen A., 2014. Slow slip and the transition from fast to slow fronts in the rupture of frictional interfaces. *Proceedings of the National Academy of Sciences of the United States of America* 111, 8764.
- [37] Absi E., Prager W., 1975. A comparison of equivalence and finite element methods. *Computer Methods in Applied Mechanics and Engineering* 6, 59.
- [38] Oden J.T., Martins J.A.C., 1985. Models and computational methods for dynamic friction phenomena. *Computer Methods in Applied Mechanics and Engineering* 52, 527.
- [39] Wriggers P., 2006. *Computational Contact Mechanics*. Springer, Berlin, Germany.
- [40] Baum M.J., Heppe L., Fadeeva E., Gorb S.N., 2014. Dry friction of microstructured polymer surfaces inspired by snake skin. *Beilstein Journal of Nanotechnology* 5, 1091.
- [41] Li N., Xu E., Liu Z., Wang X., Liu L., 2016. Tuning apparent friction coefficient by controlled patterning bulk metallic glasses surfaces. *Scientific Reports* 6, 39388.

- [42] Rubinstein S.M., Cohen G., Fineberg J., 2004. Detachment fronts and the onset of dynamic friction. *Nature* 430, 1005.
- [43] Johnson K.L., 1985. *Contact Mechanics*. Cambridge University Press, Cambridge, United Kingdom.
- [44] Popov V.L., 2010. *Contact Mechanics and Friction - Physical principles and applications*. Springer, Berlin, Germany.

Chapter 4

Third-body friction between wavy surfaces

4.1 Introduction

The tribological properties of surfaces can be significantly influenced by the presence of third bodies [1]. In the classical Godet's view of wear [2,3], any contact condition involving more than two interacting surfaces can be considered as a three-body contact. The most simple case is represented by the fluid film lubrication, which is perfectly formalized through the Reynolds' equation, deriving from the well-known Navier-Stokes' equations [4]. Instead, when solid particles are present between two surfaces, the three-body interaction becomes more complex.

Many times, third bodies are generated within the contact region and their existence is, in general, not predictable. It is the case of wear, which, through different processes depending on load, surface chemistry, material properties, etc., can generate debris that remain trapped in the interface [5-7]. Wear debris can even have a beneficial effect, in fact in some cases they can lower the coefficient of friction and extend the life of tribo-contacts

[8].

In other circumstances, the presence of third bodies is specifically designed, as during the surface finishing of metals or in the case of solid lubricants. In fact, when the contact conditions do not permit the standard fluid lubrication (e.g., in the case of extreme temperatures and pressures), particulate materials are used. A distinction is usually made between powder and granular lubricants: while the former are soft cohesive particles that deform under the application of load, granular materials are hard cohesionless particles that generate a load-carrying capacity through collisions and maintaining their geometry [9].

Several approaches have been followed to study the behaviour of particles in confined geometries, e.g., theories derived from the kinetic theory of gases [10] or from the conservation laws of fluid mechanics [11,12], micromechanical contact models [13,14] or even atomistic simulations [15]. More in general, a distinction between continuum and discrete approaches is usually made [16].

The mechanics of three-body contacts is further complicated by the roughness of the surfaces, which determines not only the interactions between asperities but can affect also the kinetics of the particles. It is demonstrated that the surface roughness has a fundamental impact on wear, adhesion, contact mechanics and friction. Despite several studies were able to correlate the roughness to the contact mechanics [17,18] or the coefficient of friction [19] between sliding surfaces, the concomitant effect of roughness and presence of particles is still not well understood.

In this Chapter, we present a systematic analysis of the influence of the surface roughness on third-body friction. By employing the discrete element method (DEM), we interpose viscoelastic spherical particles between

two sliding surfaces with a sinusoidal profile, and compute the global coefficient of friction. Furthermore, we carry out sensitivity analyses based on some contact parameters, which determine the particle-particle and particle-surface interactions, and other operational conditions, i.e., the applied normal pressure and the sliding velocity.

4.2 Methods

4.2.1 The discrete element method

The DEM [20] allows to compute the behaviour of an assembly of particles obeying to the Newton's second law of motion and interacting through specific contact models. For each particle i in contact with a particle j , the translational and rotational equations of motion, denoting with \mathbf{x}_i and $\boldsymbol{\theta}_i$ the respective degrees of freedom, are:

$$m_i \ddot{\mathbf{x}}_i = \sum_j \mathbf{F}_{ij,n} + \sum_j \mathbf{F}_{ij,t} \quad (4.1a)$$

$$I_i \ddot{\boldsymbol{\theta}}_i = \sum_j \mathbf{r}_i \times \mathbf{F}_{ij,t} + \mathbf{T}_i \quad (4.1b)$$

where m_i is the mass of the particle, I_i its moment of inertia, $\mathbf{r}_i \times \mathbf{F}_{ij,t}$ the torque exerted by the tangential force and \mathbf{T}_i the torque due to the rolling friction.

In the DEM approach, the particles are allowed to overlap and the resulting interaction forces are given by:

$$\mathbf{F}_{ij,n} = -k_n \boldsymbol{\delta}_n + \gamma_n \Delta \mathbf{u}_{ij,n} \quad (4.2a)$$

$$\mathbf{F}_{ij,t} = \min \{ | -k_t \boldsymbol{\delta}_t + \gamma_t \Delta \mathbf{u}_{ij,t} |, \mu_m \mathbf{F}_{ij,n} \} \quad (4.2b)$$

where $\boldsymbol{\delta}$ is the overlap, $\Delta \mathbf{u}_{ij}$ the relative impact velocity, μ_m the local coefficient of friction and the subscripts n and t refer to normal and tangential,

respectively. The stiffnesses k and the damping coefficients γ are, in general, nonlinear with δ : by varying their values, it is possible to implement different contact models [21,22]. The value of γ , specifically, is a measure of the elasticity of the collisions and depends on the coefficient of restitution e , which is related to the material properties and the relative impact velocities [23,24]. The contribution of the rolling friction can be included as well, e.g., in order to simulate the effects of a non-spherical particle shape [25,26].

The numerical integration of the equations of motion (4.1) is carried out through a velocity Verlet algorithm [27].

4.2.2 Modelling details

In this study, the particle-particle and particle-wall collisions are modelled through a Hertz's contact law [21,18], which defines the normal and tangential stiffnesses as reported in Appendix B. The rolling friction, when present, is treated instead through an elastic-plastic spring-dashpot model (see [26] for details).

The choice of the time step is critical in DEM simulations: a too large value does not allow to capture all the interactions at the particle level, while a too small time step increases the computational time. Here this choice is carried out considering the main dynamic effects characterising the collisions. The characteristic time of an elastic impact between two bodies is defined by the Hertz's time [28]:

$$\Delta t_H \approx 2.87 \left(\frac{m_{eq}}{R_{eq} E_{eq}^2 \Delta u_{ij,max}} \right)^{1/5} \quad (4.3)$$

being $\Delta u_{ij,max}$ the maximum relative impact velocity and m_{eq} , R_{eq} and E_{eq} the equivalent mass, radius and Young's modulus of the particles as defined

in Appendix B. The characteristic time of propagation of a surface wave in an elastic contact, instead, is defined by the Reyleigh's time [28,29]:

$$\Delta t_R \approx \frac{\pi D/2}{0.8766 + 0.163\nu} \left(\frac{\rho}{G}\right)^{1/2} \quad (4.4)$$

being ρ the material density, ν the Poisson's ratio, G the shear modulus and D the particle diameter. In addition, a time step lower than the Verlet's time:

$$\Delta t_V \approx 2/\omega \quad (4.5)$$

ensures the stability of the integration algorithm. ω is the natural frequency of an equivalent harmonic oscillator and here it is assumed $\omega \approx \sqrt{k_n/m}$.

Therefore, we choose the suitable time step according to:

$$\Delta t = \min \{\eta \Delta t_V, \eta \Delta t_H, \eta \Delta t_R\} \quad (4.6)$$

with $\eta = 0.4$ chosen as "safety factor".

All the length quantities are nondimensionalised with respect to the reference length scale $l_{\text{ref}} = 1 \mu\text{m}$. The time quantities, instead, are expressed with respect to the reference time scale $t_{\text{ref}} = 1 \mu\text{s}$. Then, we define the reference velocity and kinetic energy scales, respectively, as $v_{\text{ref}} = l_{\text{ref}}/t_{\text{ref}} = 1 \mu\text{m}/\mu\text{s}$ and $k_{\text{ref}} = \rho l_{\text{ref}}^3 v_{\text{ref}}^2 = 1 \cdot 10^{-15} \text{ J}$.

4.2.3 Geometry and extraction of the coefficient of friction

The first objective of this Chapter is to study the effect of the surface roughness on the frictional properties of the system. Therefore, we choose to model the walls with a sinusoidal profile with given amplitude A and wavelength λ . The lower and the upper surfaces are described, respectively,

by the following equations:

$$y_l(x, t) = A \sin\left(\frac{2\pi}{\lambda}x + vt\right) \quad (4.7a)$$

$$y_u(x, t) = y_u(x) = A \sin\left(\frac{2\pi}{\lambda}x\right) + c \quad (4.7b)$$

where c is the clearance and v the sliding velocity of the lower surface. Between the two surfaces, we interpose monodisperse spherical particles with diameter $D/l_{\text{ref}} = 2$, as schematised in Figure 4.1. All the simulations are 3D and periodic boundary conditions in the sliding direction are achieved, with a good approximation, by considering an annular shear cell (see Appendix B for details).

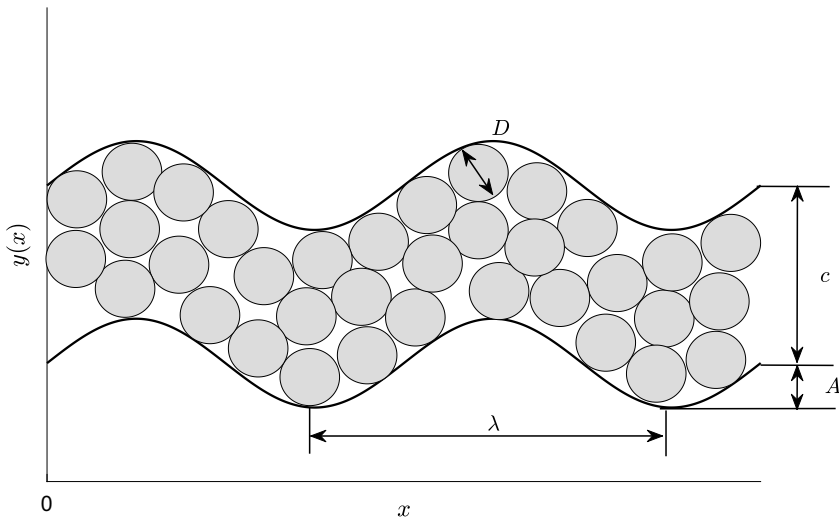


Figure 4.1: 2D view of the computational domain and main geometric parameters.

We assign the same material properties both to the particles and to the

walls, choosing $\rho = 1000.0 \text{ kg m}^{-3}$, $E = 100.0 \text{ GPa}$ and $\nu = 0.3$. With these values, from Equation (4.6) we get a "safe" time step $\Delta t/t_{\text{ref}} = 1 \cdot 10^{-4}$.

Each simulation is composed of two subsequent steps:

Step 1. a compression phase, during which a constant pressure p_a is applied on the upper surface in order to pack the particles until equilibrium is reached;

Step 2. a sliding phase, during which the lower surface is moved with a constant velocity keeping constant the pressure applied on the upper surface.

The equilibrium at the Step 1 above is evaluated by monitoring the total normal pressure exerted by the particle packing on the upper surface: when this value equals the applied normal pressure, then the compression is considered complete. Here we choose $T_c/t_{\text{ref}} = 8$ as the duration of the compression phase and $T_s/t_{\text{ref}} = 8$ of the sliding phase, for a total simulated time $T_{\text{tot}}/t_{\text{ref}} = T_c/t_{\text{ref}} + T_s/t_{\text{ref}} = 16$.

The main quantities extracted during the simulations are the normal and tangential mean (i.e., space-averaged) stresses as function of time, $p(t)$ and $\tau(t)$ respectively, exerted by the particle packing on the upper surface. Thus, we define the global dynamic coefficient of friction as the ratio between the corresponding time-averaged quantities:

$$\mu = \frac{\bar{\tau}}{\bar{p}} \quad (4.8)$$

In addition, we compute the total translational kinetic energy of the particles as:

$$K(t) = \frac{1}{2} \sum_{i=1}^N m_i u_i(t)^2 = \frac{1}{2} N m \sum_{i=1}^N u_i(t)^2 \quad (4.9)$$

where the last equality is valid if all the N particles have the same mass, as in our case.

The time averaging of $p(t)$, $\tau(t)$ and $K(t)$ is performed from $t/t_{\text{ref}} = 10$ to $t = T_{\text{tot}}$, in order to exclude the initial transient of the sliding phase.

In Table [4.2.3](#) we list all the simulation cases considered in this work. For each value of the operational conditions and the contact parameters, we perform a sensitivity analysis on all the geometric quantities. A different number of particles is used to vary the clearance. Anyway, the value of c cannot be determined *a priori*, because it depends on the applied pressure and on the surface roughness, both influencing the packing. Hereafter with "small clearance" we refer to the case $N = 12000$ and with "large clearance" to the case $N = 24000$. In a first approximation, for $p_a/E = 0.01$ the corresponding values of the clearance are $c/l_{\text{ref}} \approx 10$ and $c/l_{\text{ref}} \approx 20$, respectively. In addition to the values of A and λ reported in the Table, the case of smooth surfaces (i.e., $A/l_{\text{ref}} = 0$) is also taken into account.

For each case we run three simulations with different starting positions of the particles, which are inserted randomly in the computational domain. Therefore, all the results are presented with a mean value and a standard deviation. The latter results to be higher for higher N , because the global behaviour of the system becomes more sensitive to the (random) starting positions of the particles.

4.3 Results and discussion

4.3.1 Forces and kinetic energies

The typical time evolution of the normal and tangential stresses is shown in Figure 4.2. Before the end of the compression phase, the total normal

Geometric parameters		
surface amplitude	A/l_{ref}	0.5
		1.0
		1.5
		2.0
		2.5
		3.0
surface wavelength	λ/l_{ref}	2π
		4π
		6π
		8π
clearance	c	small
		large
Operational conditions		
applied pressure	p_a/E	0.0001
		0.001
		0.01*
		0.1
sliding velocity	v/v_{ref}	0.5
		5*
		50
		500
Contact parameters		
coefficient of restitution	e	0.3
		0.5*
		0.7
		0.9
local coefficient of friction	μ_m	0.1*
		0.3
		0.5
		0.7
		0.9
coefficient of rolling friction	μ_r	0.0*
		0.1
		0.5

Table 4.1: Simulation cases: sensitivity analysis on the geometric parameters and other simulation settings. The values marked with * represent the reference simulation settings. For all the simulations $\rho = 1000.0 \text{ kg m}^{-3}$, $E = 100.0 \text{ GPa}$, $\nu = 0.3$, $D/l_{\text{ref}} = 2$ and $\Delta t/t_{\text{ref}} = 1 \cdot 10^{-4}$.

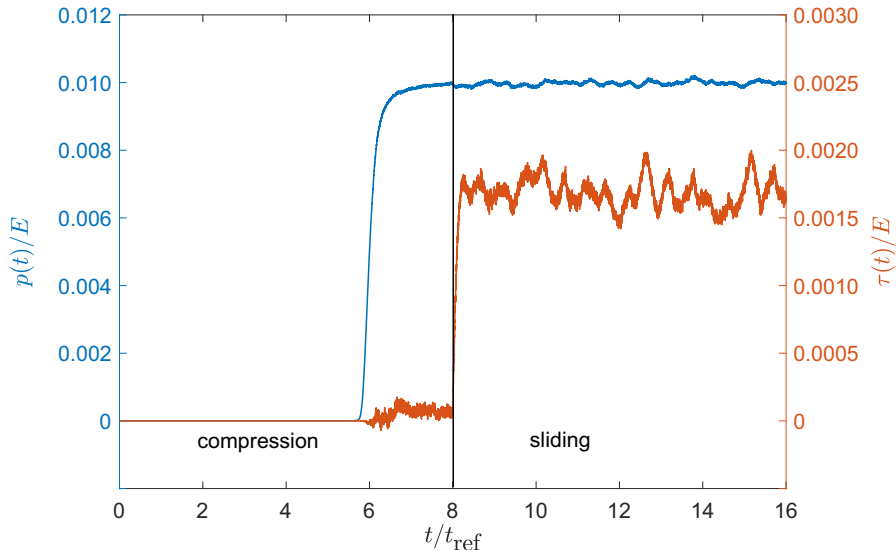


Figure 4.2: Time evolution of the normal and tangential stresses for the reference simulation case ($D = l_{\text{ref}} = 2$, $p_a = E = 0.01$, $v = v_{\text{ref}} = 5$, $e = 0.5$, $\mu_m = 0.1$, $\mu_r = 0.0$), small c , $A/l_{\text{ref}} = 2.5$ and $\lambda/l_{\text{ref}} = 4$. The vertical dashed line separates the compression and the sliding phases.

pressure exerted by the particle packing on the upper surface equals the applied pressure, i.e., the system reaches equilibrium as defined before. Then, during the sliding phase, the tangential stress oscillates around an average value, after an initial transient. From the curves in the Figure, we can assume that $\bar{p} \approx p_a$ during the whole duration of the sliding phase.

In general, in the tangential stress curve it is hard to identify a peak corresponding to the static friction. In fact, being the static friction related to an initial "stick" phase, before the "slip" of the interacting surfaces, here we can conclude that a complete stick never happens. The particles are always in motion, as demonstrated by the time evolution of the total kinetic en-

ergy, which never goes identically to zero. Hence, the system evolves from a condition of partial slip at the beginning of the sliding phase, to a complete slip during the steady-state motion. Therefore, the global coefficient defined in Equation (4.8) and used hereafter must be considered as a dynamic (or kinetic) coefficient of friction.

The period of the oscillations of both $p(t)$ and $\tau(t)$, is in general independent of the amplitude of the surface roughness, but it is rather related to the wavelength. Also a change in the sliding velocity modifies the period. A frequency-domain analysis of the signal, in fact, validates these properties (see Appendix B). The periodic oscillations can be related to the creation and subsequent breakup of force chains connecting the asperities of the surfaces. The creation of "bridges" connecting the asperities has been suggested also by other authors (see [16] and references therein). This phenomenon is also reported by Aharonov and Sparks [30], who attribute to the force network the overall system dynamics, and in particular the transition from sliding to stick-slip motion and *vice versa* (depending on the combination between confining load and sliding velocity). An in-depth analysis of these phenomena is, however, beyond the scope of the present work.

The total kinetic energy as function of time is shown in Appendix B. Again, a clear distinction between the compression and the sliding phase is present. The increase in the value of $K(t)$ at around half of the compression phase is due to a sudden increase in the motion of the particles, which move to the final packing positions, corresponding to the lowest value at around $t/t_{\text{ref}} = 5.5$. As mentioned above, this "residual" kinetic energy could be responsible for the absence of a static friction. After the beginning of the sliding phase, the total kinetic energy reaches a steady-state value.

4.3.2 Reference simulation case

The simulation case taken as reference has the parameters highlighted in Table 4.1. In particular, we choose $e = 0.5$, $\mu_m = 0.1$ and no rolling friction (i.e., $\mu_r = 0$) as contact parameters, and apply a constant normal pressure $p_a/E = 0.01$ and a constant sliding velocity $v/v_{\text{ref}} = 5$. In Figure 4.3 the global coefficient of friction is plotted as function of A , λ and c .

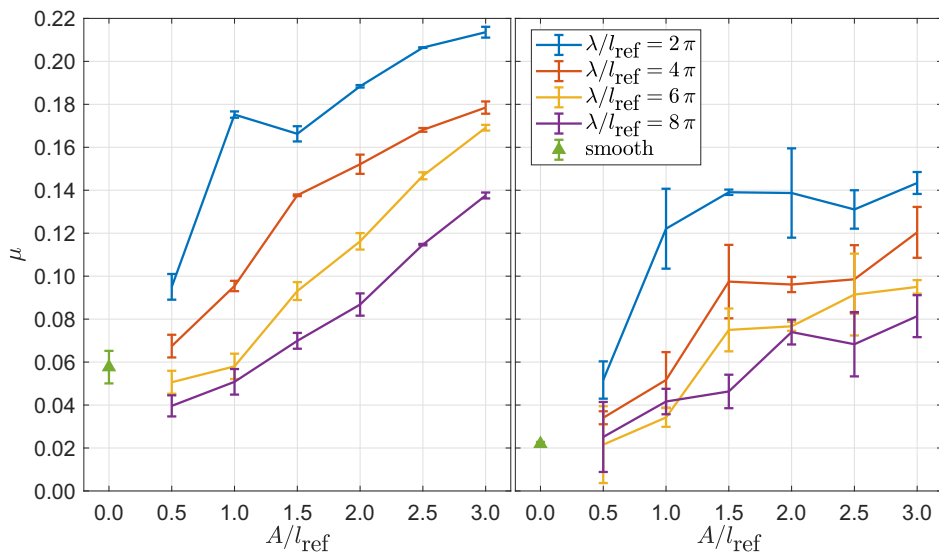


Figure 4.3: Global coefficient of friction as function of A and λ , for the reference simulation case ($D = l_{\text{ref}} = 2$, $p_a = E = 0.01$, $v = v_{\text{ref}} = 5$, $e = 0.5$, $\mu_m = 0.1$, $\mu_r = 0.0$). Left: small c . Right: large c .

In general, we observe that μ increases for increasing amplitudes and decreases for increasing wavelengths, for a fixed value of the clearance. Instead, μ decreases with increasing c , for a given amplitude and wavelength. This is due to the fact that higher A and lower λ and c reduce the magnitude of

the force chains between the surfaces, while the particles are able to form a sort of a "fluid-like" layer in the opposite case. All the curves converge towards the point corresponding to the case of smooth surfaces. However, in this case the computed value of μ is slightly higher than expected and closer to μ_m : we believe it is due to the particle-wall slip, which is governed by the local coefficient of friction and is promoted by higher values of the applied pressure. In fact, this phenomenon is reduced for larger c , since a smaller fraction of the total number of particles is in contact with the walls.

The observed trend in the global coefficient of friction can be qualitatively explained through the Prandtl-Tomlinson's model, which describes the behaviour of a point mass particle pulled in a periodic potential [31,32] and is generally applied to nanoscale systems, e.g., atomic force microscopy [33]. It is found that the frictional force scales as $F_t \propto A/\lambda$, for a given sliding velocity [33]. Hence, we attempt to fit the data from the simulations with functions of the type $\mu = \mu(A, \lambda)$.

The solution of the Prandtl-Tomlinson's model suggests the following best-fit:

$$\mu = \beta_{11} \frac{A}{\lambda} + \beta_{12} \quad (4.10)$$

Since the computed R^2 value is lower than 0.7, we propose a slightly modified version of Equation (4.10):

$$\mu = \beta_{21} \left(\frac{A}{\lambda} \right)^{\beta_{22}} + \beta_{23} \quad (4.11)$$

from which we find $R^2 > 0.9$. The fitting parameters β_{ij} for the cases of small and large clearance are reported in Table 4.2.

In addition, it is interesting to evaluate if a system made of two rough surfaces can be represented by an equivalent system with one smooth and one rough surface, as done in classical contact mechanics [28,34]. For

	small c	large c
Equation (4.10)	$\beta_{11} = -0.0038$ $\beta_{12} = 0.173$ $R^2 = 0.6902$	$\beta_{11} = -0.0027$ $\beta_{12} = 0.116$ $R^2 = 0.6644$
Equation (4.11)	$\beta_{21} = -4.847$ $\beta_{22} = 0.0125$ $\beta_{23} = 5.109$ $R^2 = 0.9402$	$\beta_{21} = -1.966$ $\beta_{22} = 0.0214$ $\beta_{23} = 2.143$ $R^2 = 0.9099$

Table 4.2: Surface best fits of the type (4.10) and (4.11) for the reference simulation case: fitting parameters β_{ij} and R^2 values.

this purpose, we consider a lower surface with an equivalent roughness obtained by summing the amplitudes of the starting profiles, i.e., $y_l(x, t) = 2A \sin\left(\frac{2\pi}{\lambda}x + vt\right)$, and a smooth upper surface, i.e., $y_u(x, t) = y_u(x) = c$. The results confirm that the assumed equivalence is not valid. In our case, the particle-wall slip on the smooth surface and the modification of the force chains defining the interactions between the asperities, contribute to further invalidate the assumption.

The trend of the time-averaged kinetic energy \bar{K} , instead, is depicted in Figure 4.4. We observe that the order of magnitude of \bar{K}/k_{ref} is in the range $\sim 10^6 \div 10^7$, which is the same of the quantity Nmv^2 . However, due to the contact with the asperities on the static (i.e., upper) surface, not all the N particles are able to acquire the sliding velocity v , but only a fraction N' . Consequently, the difference:

$$\bar{K}'(A, \lambda) = \frac{1}{2}Nmv^2 - \bar{K}(A, \lambda) \quad (4.12)$$

quantifies the amount of translational kinetic energy in directions other than

that of the sliding motion.

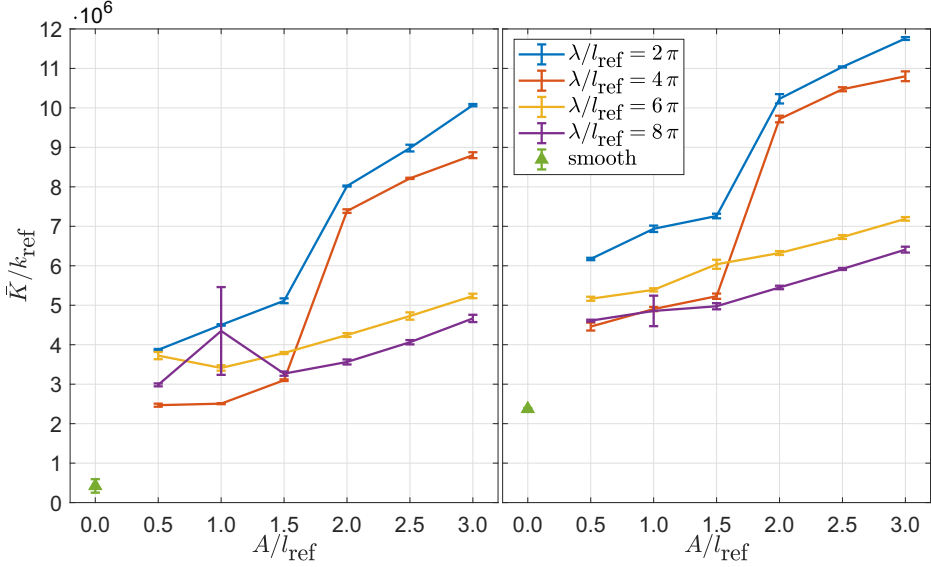


Figure 4.4: Total time-averaged kinetic energy as function of A and λ , for the reference simulation case ($D = l_{\text{ref}} = 2$, $p_a = E = 0.01$, $v = v_{\text{ref}} = 5$, $e = 0.5$, $\mu_m = 0.1$, $\mu_r = 0.0$). Left: small c . Right: large c .

In addition, we observe that the total kinetic energy of the particles increases for increasing amplitudes, since a larger fraction of N is able to acquire the lateral momentum exerted by the sliding wall. This result is qualitatively in agreement with the kinetic theory of granular flows [10,35], where the so-called granular temperature (i.e., the fluctuating component of the translational kinetic energy) increases for an increasing lateral momentum imparted by the walls.

Again, the curves do not converge towards the case of smooth surfaces, since the particle-wall slip contributes to lower the particle velocity and thus the

total kinetic energy.

4.3.3 Effect of operational conditions

To show the effect of the applied normal pressure on the frictional response of the system, we have varied p_a/E over four orders of magnitude, keeping constant the sliding velocity. In Figure 4.5 the time-averaged tangential stress $\bar{\tau}/E$ is plotted as function of \bar{p}/E for an example case.

A linear fit of the type:

$$\bar{\tau} = \tau_0 + \mu \bar{p} \quad (4.13)$$

with τ_0 and μ as fitting parameters, shows a perfect agreement with the classical Coulomb's law of friction [36]. Therefore, τ_0 and μ effectively represent the cohesion of the granular material and the global coefficient of friction, respectively. In particular, given the negligible value of τ_0 with respect to \bar{p} for the reference simulation case, the value of μ extracted from the best-fit (4.13) is practically equal to that computed through Equation (4.8).

The case $p_a/E = 0.1$ is excluded from the best fit, because a lower global coefficient of friction, and thus a deviation from linearity expressed by Equation (4.13), is observed. We attempt to explain this phenomenon following two main mechanisms. Firstly, we find an average kinetic energy two orders of magnitude greater than that computed for smaller applied pressures. Since we keep constant the sliding velocity, from the quantity (4.12) we may conclude that a larger normal load increases the other components of the translational velocity of the particles and/or their vibrational energy. Secondly, for the highest value of the applied pressure, we report the occurrence of slip avalanches, highlighted by an abrupt increase in the total kinetic energy. Correspondingly, the instantaneous value of the tangential stress decreases, contributing to further lower its time-averaged value and

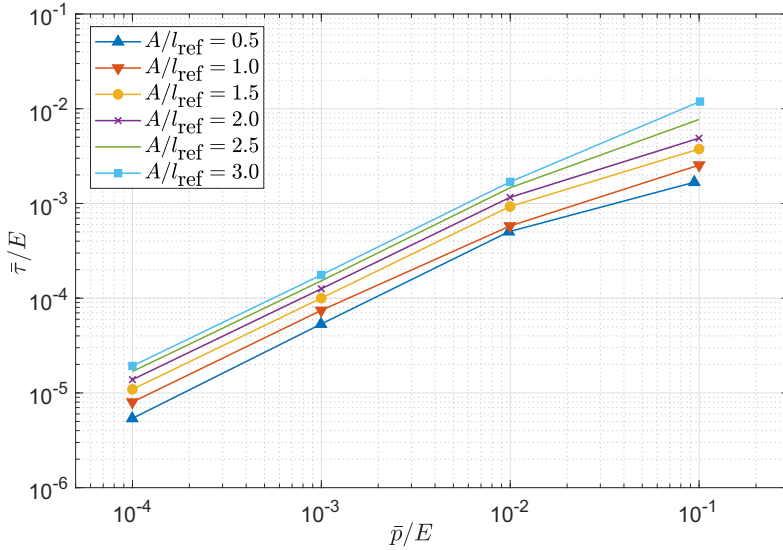


Figure 4.5: Time-averaged tangential vs. normal stress as function of the surface amplitude, for four simulation cases with different applied pressures ($D = l_{\text{ref}} = 2$, $v = v_{\text{ref}} = 5$, $e = 0.5$, $\mu_m = 0.1$, $\mu_r = 0.0$), small c and $\lambda/l_{\text{ref}} = 3\pi$.

thus the global coefficient of friction. This phenomenon is represented qualitatively in Figure 4.6: despite also $p(t)$ is affected by the slip avalanches, its time-averaged value remains $\bar{p} \approx p_a$; thus we can ascribe the lower coefficient of friction solely to a lower $\bar{\tau}$.

The decrease in the coefficient of friction for higher applied normal stresses is observed also in experimental works in granular lubrication (see, e.g., [37]). Strictly speaking, the authors correlate the increase in the normal stress to the increase in the solid fraction, i.e., the ratio between the volume occupied by the particles and the total volume, and then the solid fraction to the decrease in the coefficient of friction. Since the observed behaviour

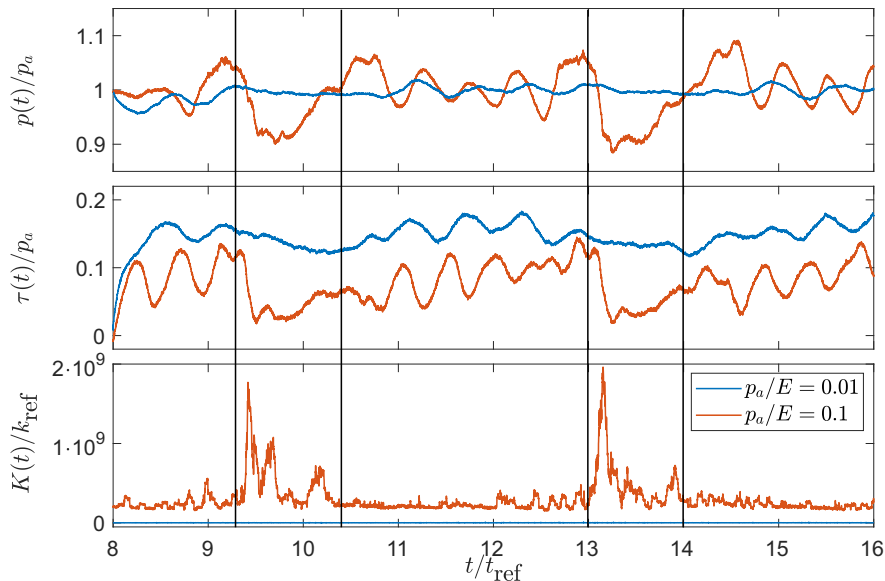


Figure 4.6: Normal stress (top), tangential stress (centre) and total kinetic energy (bottom) as function of time for two simulation cases with different applied pressures ($D = l_{\text{ref}} = 2$, $v = v_{\text{ref}} = 5$, $e = 0.5$, $\mu_m = 0.1$, $\mu_r = 0.0$), small c , $A/l_{\text{ref}} = 2.5$ and $\lambda/l_{\text{ref}} = 6\pi$. The occurrence of slip avalanches is highlighted in two time intervals (between the vertical lines).

cannot be predicted by theory, the authors suppose that the measured reduction in μ can be due to "the formation of the internal microstructures" [37], which now we can suggest to attribute to the two mechanisms mentioned above.

The effect of the sliding velocity of the lower wall is shown in Figure 4.7 for an example case. Again, we vary v over four orders of magnitude, keeping constant the applied normal pressure. The observed trend of the global coefficient of friction can be fitted through:

$$\mu = \beta_3 + \beta_4 \ln v \quad (4.14)$$

where β_3 and β_4 are fitting parameters. A similar dependence on the sliding velocity is observed in experimental works on rock friction, where the so-called rate/state-variable constitutive laws apply, such as the Dieterich-Ruina's expression [38]. Anyway, granular materials under very high shear rates can show a deviation from this logarithmic law [39].

Note that also the above-mentioned Prandtl-Tomlinson's model predicts a logarithmic dependence of the frictional force on the sliding velocity [40].

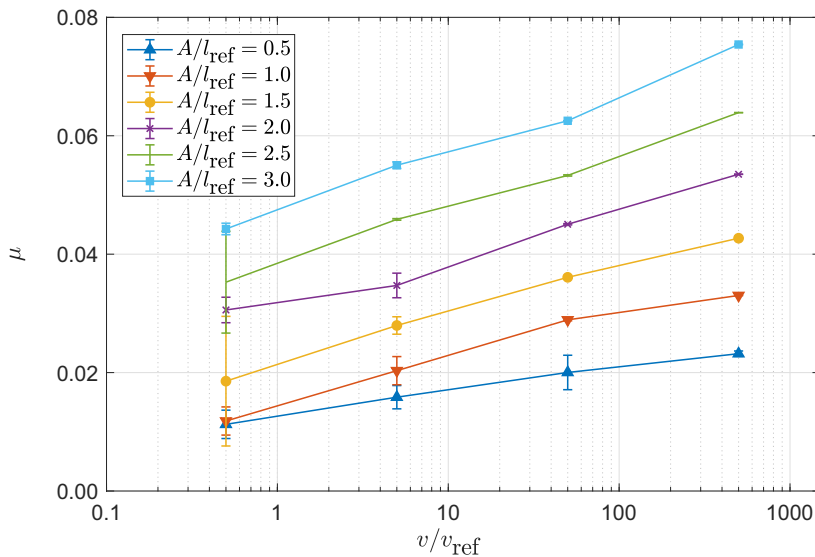


Figure 4.7: Global coefficient of friction vs. sliding velocity as function of the surface amplitude, for four simulation cases with different sliding velocities ($D = l_{\text{ref}} = 2$, $p_a/E = 0.01$, $e = 0.5$, $\mu_m = 0.1$, $\mu_r = 0.0$), small c and $\lambda/l_{\text{ref}} = 8\pi$. The occurrence of slip avalanches is highlighted in two time intervals (between the vertical lines).

4.3.4 Effect of contact parameters

Despite the contact parameters determine the particle interactions, we demonstrate that they have a poor influence on the overall behaviour of the system, i.e., on the global coefficient of friction. In Appendix B we show how the local coefficient of friction, the coefficient of restitution and the rolling friction affect μ .

We notice that the local coefficient of friction has almost no influence on the global response of the system. This result is in agreement with numerical simulations of dense granular flows in confined and open geometries [40], where the effect of μ_m is relevant only when it is vanishingly small, i.e., smaller than 0.1.

Similarly, the coefficient of restitution has no effect for $e \geq 0.5$, i.e., when the collisions are more "elastic" (or, equivalently, with reduced dissipation). A smaller value of μ , instead, is found for $e = 0.3$, which can be due to an unphysical behaviour emerging for very high damping [24].

The presence of rolling friction influences μ only for high values of μ_r : for $\mu_r = 0.5$ we observe a reduction in the global coefficient of friction. This result can be explained by a rearrangement of the stress distribution in the particle packing: the rolling resistance reduces the amount of normal stress transferred laterally and enlarges the angular distribution of the contact forces [41].

4.4 Conclusions

In this Chapter we have presented a DEM-based approach to third-body friction, focused on a systematic analysis of the effect of surface roughness. The main quantities describing our roughness model (i.e., amplitude, wavelength and clearance) are demonstrated to have a deep influence on the

global coefficient of friction. A best-fit suggested by the classical Prandtl-Tomlinson's model, describes well the observed trends.

In addition, we have varied two macroscopic operational conditions:

- the applied normal pressure, whose effect is perfectly described by the Coulomb's law, except for very high pressures, where the increase in the total kinetic energy and the occurrence of slip avalanches contribute to lower the global coefficient of friction;
- the sliding velocity, which affects μ through a logarithmic law, as observed in experimental works and predicted, again, by the Prandtl-Tomlinson's model.

These results suggest that, in principle, the Prandtl-Tomlinson's model could be even extended to the viscoelastic dynamics of a macroscopic particle on a periodic profile.

Finally, we have demonstrated that the global coefficient of friction is nearly independent from the contact parameters, which define the particle-particle and particle-wall interactions.

A limit of the presented model is represented by the use of rigid walls, whose elastic deformations can be taken into account only through more advanced approaches, e.g., coupling the DEM to the finite element method (FEM). Future researches should be addressed to the evaluation of more complex surface profiles and of non-constant (e.g., Gaussian) particle size distributions. We believe the results of the present work could be of interest towards the design of new tribo-materials and surfaces with enhanced and precisely engineered performance.

References

- [1] Singer I.L., 1998. How third-body processes affect friction and wear. *MRS Bulletin* 23, 37.
- [2] Godet M., 1984. The third-body approach: a mechanical view of wear. *Wear* 100, 437.
- [3] Godet M., 1990. Third-bodies in tribology. *Wear* 136, 29.
- [4] Hamrock B.J., Schmid S.R., Jacobson B.O., 2004. *Fundamentals of Fluid Film Lubrication*. Marcel Dekker, New York, United States of America.
- [5] Diomidis N., Mischler S., 2011. Third body effects on friction and wear during fretting of steel contacts. *Tribology International* 44, 1452.
- [6] Sherrington I., Hayhurst P., 2001. Simultaneous observation of the evolution of debris density and friction coefficient in dry sliding steel contacts. *Wear* 249, 182.
- [7] Singer I.L., Mogne T.L., Donnet C., Martin J.M. 1996. Third body formation and friction reduction on Mo/SiC sliding in reactive gases. *Tribology Series* 31, 79.
- [8] Singer I.L., Dvorak S.D., Wahl K.J., Scharf T.W., 2003. Role of third bodies in friction and wear of protective coatings. *Journal of Vacuum Science & Technology A: Vacuum, Surfaces, and Films* 21, S232.
- [9] Worniyoh E.Y.A., Jasti V.K., Higgs C.F., 2007. A review of dry particulate lubrication: powder and granular materials. *Journal of Tribology, Transactions ASME* 129, 438.
- [10] Lun C.K.K., Savage S.B., 1987. A simple kinetic theory for granular flow of rough, inelastic, spherical particles. *Journal of Applied Mechanics, Transactions ASME* 54, 47.
- [11] Haff P.K., 1983. Grain flow as a fluid-mechanical phenomenon. *Journal of Fluid Mechanics* 134, 401.
- [12] Jang J.Y., Khonsari M.M., 2005. On the granular lubrication theory. *Proceedings of the Royal Society of London A: Mathematical, Physical and Engineering Sciences* 461, 3255.
- [13] Horng J.H., Wei C.C., Tsai H.J., Shiu B.C., 2009. A study of surface friction and particle friction between rough surfaces. *Wear* 267, 1257.
- [14] Ghaednia H., Jackson R.L., 2013. The effect of nanoparticles on the real area of contact, friction, and wear. *Journal of Tribology, Transactions ASME* 135, 041603.

- [15] Bai L., Srikanth N., Kang G., Zhou K., 2016. Influence of third particle on the tribological behaviors of diamond-like carbon films. *Scientific Reports* 6, 38279.
- [16] Iordano I., Berthier Y., Descartes S., Heshmat H., 2002. A review of recent approaches for modeling solid third bodies. *Journal of Tribology, Transactions ASME* 124, 725.
- [17] Persson B.N J., Albohr O., Tartaglino U., Volokitin A.I., Tosatti E., 2005. On the nature of surface roughness with application to contact mechanics, sealing, rubber friction and adhesion. *Journal of Physics: Condensed Matter* 17, R1.
- [18] Pohrt R., Popov V.L., 2012. Normal contact stiffness of elastic solids with fractal rough surfaces. *Physical Review Letters* 108, 104301.
- [19] Spagni A., Berardo A., Marchetto D., Gualtieri E., Pugno N.M., Valeri S., 2016. Friction of rough surfaces on ice: Experiments and modeling. *Wear* 368-369, 258.
- [20] Cundall P.A., Strack O.D.L., 1979. A discrete numerical model for granular assemblies. *Géotechnique* 29, 47.
- [21] Di Renzo A., Di Maio F.P., 2004. Comparison of contact-force models for the simulation of collisions in DEM-based granular flow codes. *Chemical Engineering Science* 59, 525.
- [22] Brilliantov N.V., Spahn F., Hertzsch J.M., Pöschel T., 1996. Model for collisions in granular gases. *Physical Review E* 53, 5382.
- [23] Thornton C., 1997. Coefficient of restitution for collinear collisions of elastic-perfectly plastic spheres. *Journal of Applied Mechanics, Transactions ASME* 64, 383.
- [24] Schwager T., Pöschel T., 2007. Coefficient of restitution and linear-dashpot model revisited. *Granular Matter* 9, 465.
- [25] Wensrich C.M., Katterfeld A., 2012. Rolling friction as a technique for modelling particle shape in DEM. *Powder Technology* 217, 409.
- [26] Ai J., Chen J.F., Rotter J.M., Ooi J.Y., 2011. Assessment of rolling resistance models in discrete element simulations. *Powder Technology* 206, 269.
- [27] Verlet L., 1967. Computer "experiments" on classical fluids. I. Thermodynamic properties of Lennard-Jones molecules. *Physical Review* 159, 98.
- [28] Johnson K.L., 1985. *Contact Mechanics*. Cambridge University Press, Cambridge, United Kingdom.

- [29] Li Y., Xu Y., Thornton C., 2005. A comparison of discrete element simulations and experiments for sandpiles composed of spherical particles. *Powder Technology* 160, 219.
- [30] Aharonov E., Sparks D., 2004. Stick-slip motion in simulated granular layers. *Journal of Geophysical Research* 109, B09306.
- [31] Prandtl L., 1928. Ein gedankenmodell zur kinetischen theorie der festen k orper. *ZAMM - Journal of Applied Mathematics and Mechanics / Zeitschrift fur Angewandte Mathematik und Mechanik* 8, 85.
- [32] Tomlinson G.A., 1929. A molecular theory of friction. *Philosophical Magazine* 7, 905.
- [33] Popov V.L., Gray J.A.T., 2012. Prandtl-Tomlinson model: history and applications in friction, plasticity, and nanotechnologies. *ZAMM - Journal of Applied Mathematics and Mechanics / Zeitschrift fur Angewandte Mathematik und Mechanik* 92, 683.
- [34] Greenwood J.A., Williamson J.B.P., 1966. Contact of nominally flat surfaces. *Proceedings of the Royal Society of London A: Mathematical, Physical and Engineering Sciences* 295, 300.
- [35] Higgs C.F., Tichy J., 2004. Granular flow lubrication: continuum modeling of shear behavior. *Journal of Tribology, Transactions ASME* 126, 499.
- [36] Popova E., Popov V.L., 2015. The research works of Coulomb and Amontons and generalized laws of friction. *Friction* 3, 183.
- [37] Yu C.M., Tichy J., 1996. Granular collisional lubrication: effect of surface roughness, particle size and solids fraction. *Tribology Transactions* 39, 537.
- [38] Sholz C.H., 1998. Earthquakes and friction laws. *Nature* 391, 37.
- [39] Hatano T., 2007. Power-law friction in closely packed granular materials. *Physical Review E* 75, 060301.
- [40] MiDi, 2004. On dense granular flows. *The European Physical Journal E* 14, 341.
- [41] Fukumoto Y., Sakaguchi H., Murakami A., 2013. The role of rolling friction in granular packing. *Granular Matter* 15, 175.
- [42] Silbert L.E., Ertas D., Grest G.S., Halsey T.C., Levine D., Plimpton S.J., 2001. Granular flow down an inclined plane: Bagnold scaling and rheology. *Physical Review E* 64, 051302.

Chapter 5

Frictional penetration in granular media

5.1 Introduction

Soil exploration is one of the activities most practiced by humans for natural resources research, civil construction, geotechnical studies, etc. For addressing such issues, different ways are being used, such as drilling, excavation, subsurface sounding tests and geophysical methods [1,2]. Drilling is a perforation process that exploits a motor (heat, hydraulic, pneumatic or electric motor) for pushing a drill bit (cutter) into the soil and making a hole. It is the most used method for extraction of water, petroleum, and natural gases; its application is so wide that it has been extended to the space exploration [3-6]. Excavation, instead, is an ancient method used for making wells by means of hoes, shovels, earthmovers, etc. It is employed for water harvesting and building construction, but also for archaeological studies and soil inspection [1,2,7]. The remaining two methods, namely subsurface sounding tests and geophysical methods, are mainly exploited in geotechnical studies. Subsurface sounding tests, in particular, allow mea-

asuring soil strength and explore soil profile by pushing a probe into the soil. The typical probing tests are Standard Penetration Test (SPT) and Cone Penetration Test (CPT). In SPT, a thick-walled sample tube is driven into the ground at the bottom of a borehole by blows from a slide hammer; whereas, in CPT, a cone penetrometer is pushed into the soil by applying, from the top, static (hammer blow) or dynamic loads (hydraulic actuators) [1,8-13].

The last exploration solution, i.e., geophysical methods, is a family of solutions used to study the soil and subsoil profile. The most exploited techniques are based on seismic reflection and electro-resistivity measurements. In the first case, the reflection response of controlled seismic waves is detected to get information about the earth's subsurface properties. In the second technique, the electrical resistivity of soil is measured for imaging sub-surface structures [14-19]. Although all the four above mentioned exploration techniques are widely used, they present some limitations. The main important limitations are: the most successful penetration method (drilling) requires high energetic costs, bulky infrastructure, and high impact on natural environments (not only soil destruction but also damage to surrounding natural areas); the less invasive measurement techniques (geophysical methods) present several drawbacks (e.g., in the electrical resistivity method, the reliability is affected by metal pipes, electrical conductors, and sloping of strata); in the case of seismic survey, instead, it is quite accurate for horizontal layers structure but requires large source-receiver offsets [1,3].

Looking at Nature, there are many living beings, such as earthworms, wasps, clams, siphons, moles, etc., that can perform penetration and perception tasks in soil [3,5,20-24]. Among digging organisms, plants are particularly efficient in terms of perforation performance and are able to reach

considerable depths (i.e., up to 100 m [25]). The key features that make plant roots so efficient are: (i) minimal friction strategy, (ii) crack propagation exploitation and (iii) high structural stability. (i) Plants adopt an efficient strategy for moving in soil based on a growth from the tip. In fact, plant roots overcome and survive into high frictional and abrasive soil environments by pushing only the apical part while the whole structure remains stationary and in contact with the surrounding medium (soil). This strategy, together with mucus exudation and sloughing cells release, allows plants to create low-friction channels and increases the penetration efficiency [26-28]. In addition to such peculiarity, plants are also able (ii) to generate lateral expansion for making cracks and going through (reducing significantly the penetration efforts); and (iii) to improve the anchorage developing hairs and lateral roots [29-31].

The first attempt of taking inspiration from plant roots to conceive innovative digging artificial solutions is described in [32]. In this work, a mechatronic system for soil exploration is proposed. The system can steer in all directions and can perform gravitropism and hydrotropism movements (i.e., the ability to follow the gravity and moisture, respectively). In [33], instead, the authors proposed a device inspired by the role of sloughing cells and root hairs in plants, demonstrating that this approach allows reducing penetration force by 30% in a granular soil medium. Further investigations on plant root mechanisms for soil penetration allowed the same authors to develop a plant-inspired robot able to grow in soil from its tip using an additive layer technique [34,35]. This system, which implements the plant growth strategy, has shown a reduction in energy consumption by 70% with respect to an analogous artificial solution pushed in soil from the top.

A study on the influence of probe's morphology in penetration efficiency was presented by Tonazzini *et al.* [36], who compared different shapes of tips

in an artificial soil to select that better accomplishing penetration tasks. The results showed that a conical shape represents the best solution for penetration in glass bead environment.

As further improvement of these previous works, in this Chapter we investigate the contribution of root-like probe morphology, especially of its apical region that represents the dynamic element of the system, in soil penetration. Specifically, we developed probes with different diameters and different shapes and compared their performance with a root-like probe in real soils, such as sandy loam. In summary, here we describe the method developed for extracting the root tip morphology, the fabrication technique used for making a bio-inspired artificial prototype, discrete element simulations of probes with different shapes to correlate the experimental results, and the experimental setup used for evaluating achievable performance in soil penetration.

5.2 Methods

5.2.1 Gross morphology of a plant root

Root is a plant organ that generally lies below the surface of soil (Figure 5.1) and consists of a root cap and a meristematic, elongation, and mature zone.

The root cap (CAP) is the most apical part of a root and has a covering role in protecting the meristematic zone from abrasion phenomena, bacteria, and microorganisms. The cap is also fundamental for reducing the soil penetration resistance by releasing sloughing cells and mucilage exudation. The meristematic zone (MER) is the root region where undifferentiated cells are located. Therefore, this portion is fundamental for providing new cells for root growth. The elongation zone (EL) is located just above to the

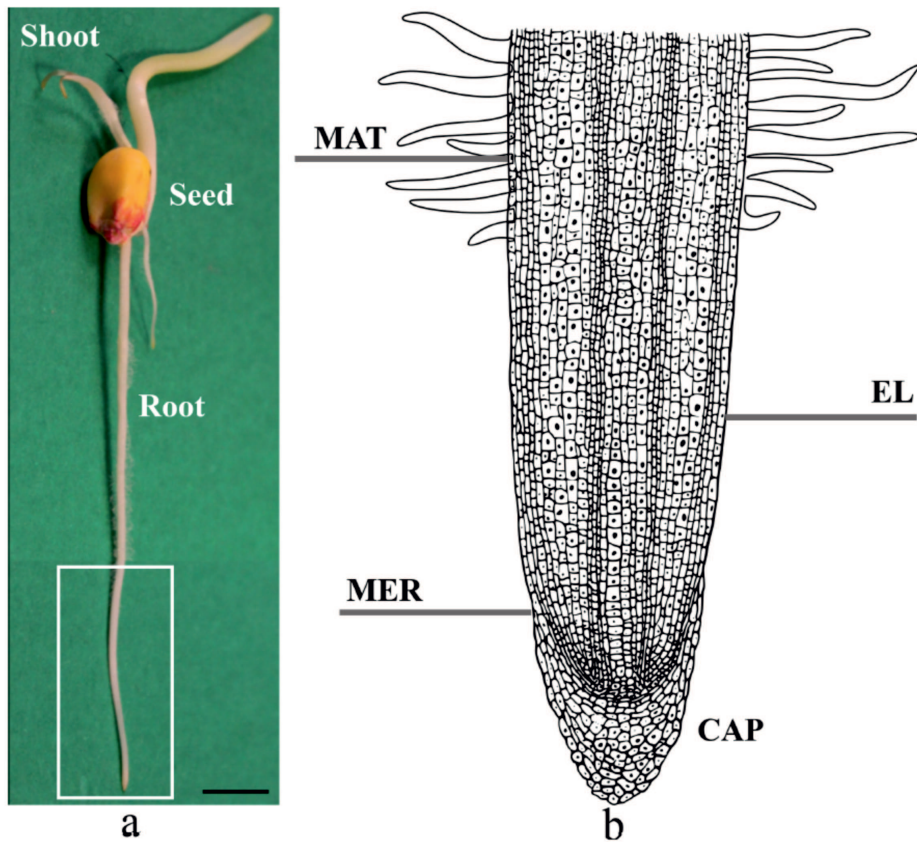


Figure 5.1: (a) 3-day old plant root. Photograph of a *Zea mays* plant with the seed, the shoot (aerial part of the plant), and the primary root (underground part of the plant). The scale bar is equal to 10 mm. (b) Structure of the plant root. Enlargement of the white box in (a), with the mature zone (MAT), the elongation zone (EL), the meristematic zone (MER) and the root cap (CAP).

meristematic zone. In this region, cells divide and elongate up to ten times of their original size and play a fundamental role in crack propagation inside the soil (for *Zea mays*; axial pressure up to 1.4 MPa and radial pressure

up to 0.6 MPa can be generated [29,37]). The mature zone (MAT) is a stationary root portion where all the cells are matured. It is characterised by the presence of lateral hairs and plays an important role in anchorage [34,38].

5.2.2 Seed germination and microscope analysis

We used maize (*Zea mays*, wild type, Ver. Kubrick Società Italiana Sementi SpA, Italy) seeds as a model in this study. The seeds were sterilized putting them in a flax with a solution of 50% of bleach and 50% of deionized water on magnetic stir for 15 minutes for two times. Afterwards, the seeds were covered with wet blotting papers and kept for 3 days in a growing chamber (Seed germinator SG 15, Nuova Criotecnica Amcota, Italy) without any obstacle at a temperature of 25°C and a humidity of 60% [39]. After 3 days of germination, we carried out a morphometric analysis (described in the following section) of root tip ($N = 11$) analysing the pictures captured with an optical digital microscope (KH-7700 Hirox Co Ltd, Japan, with AD5040HIS lens).

5.2.3 Morphometric analysis

We used a morphometric analysis to define two crucial features: the tip axial-transverse ratio and the tip profile. The first parameter refers to the ratio between the measured tip length and tip diameter, as shown in Figure 5.2. We detected the tip profile by image processing and fitting techniques, as schematised in Figure 5.3. Then, we acquired the microscope images in MATLAB R2012a (Images Processing Toolbox release 2012a, MathWorks Inc, United States). They were first aligned and then processed with the Image Processing Toolbox. This phase is fundamental for making root profile evident and proceeds with a fitting phase. Different mathematical functions

were used to find the function that better follows the tip morphology, such as gaussian, exponential, power, and polynomial functions.

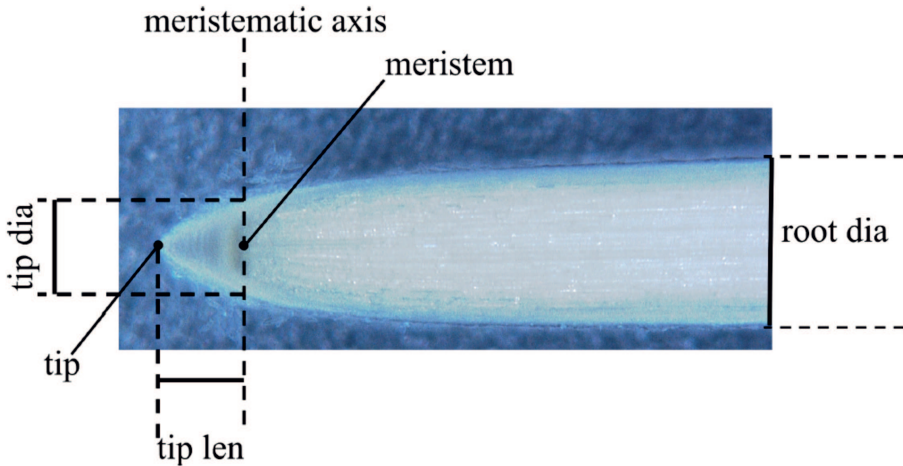


Figure 5.2: Morphometric analysis of a *Zea mays* root tip: "meristematic axis" is the transversal axis that passes throughout the meristem, which is the root zone where growth takes place, "tip dia" the root tip diameter, "tip len" the root tip length, "root dia" the root diameter in correspondence of the mature region.

5.2.4 Design and 3D printing of probes

We used the morphology of *Zea mays* root tip for designing the model of a bio-inspired by computer aided design (CAD). The artificial prototypes were then built in FullCure720 (for details refer to [40]) by 3D printing.

In order to estimate soil penetration performance (e.g., force and expended work) of the bio-inspired probe, we also manufactured other artificial probes by maintaining the same general features of the root (in particular, tip diameter and tip length) but modifying the standard tip profile (i.e.,

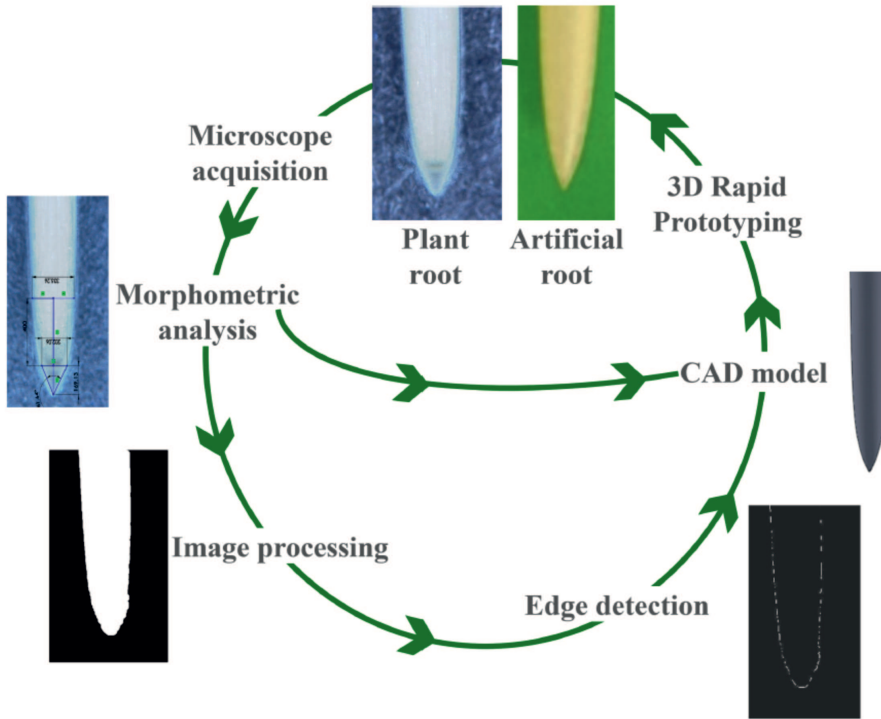


Figure 5.3: From a primary plant root to an artificial probe: schematic view of the translation method from the natural system to the artificial (i.e., bio-inspired) one.

conical, cylindrical, parabolic and elliptical), as shown in Figure 5.4.

The scale effect in soil perforation was quantified by comparing the performance of each artificial probe shape at different diameters (11, 9, 7, 5 and 3 mm). All the experimental data were analysed using ANOVA single factor method to evaluate possible differences among probes results.

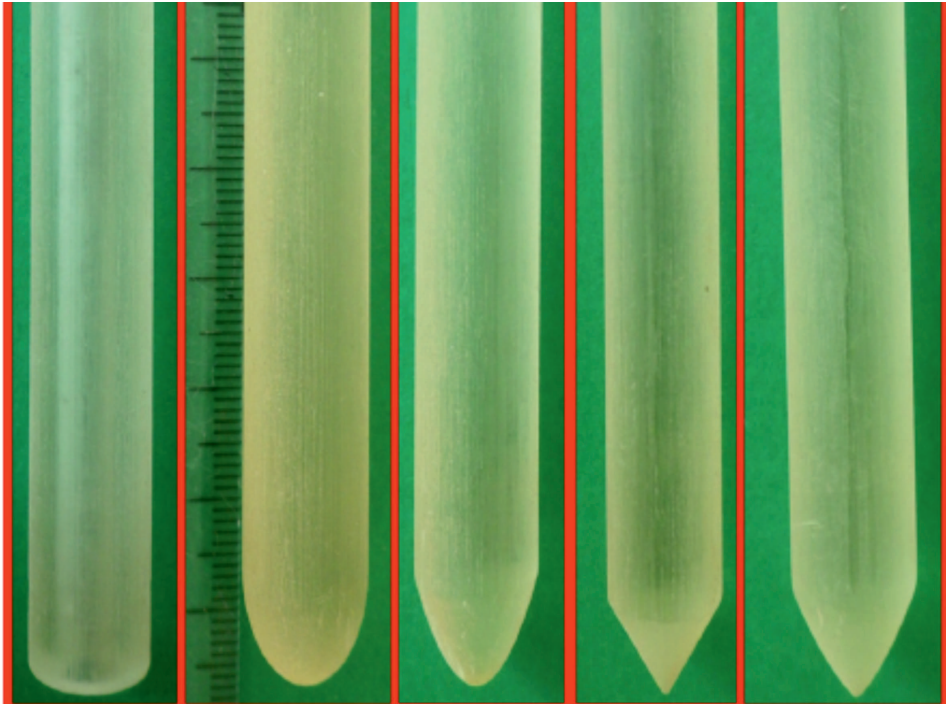


Figure 5.4: Fabricated artificial probes with 11 mm diameter. From left to right: cylindrical, elliptical, parabolic, conical and root-like geometry.

5.2.5 Penetration experiments

Penetration tests were carried out in soil by a Universal Testing Machine UTM Z005 (ZwickRoell Ltd, United Kingdom). We selected sandy loam soil and, before carrying out tests, it was kept under the sun to dry for two weeks, and then sieved to obtain homogeneous soil. After the sieving, the soil was characterized as sandy loam with 19.3% of silt, 12.0% clay and 68.7% sand. At this stage, it was kept inside an oven at 105°C for 10 hours to remove moisture. The dried soil was put in an elliptical plastic container with dimensions 22x16x20 cm for the penetration experiments. The bulk

density of the obtained medium (i.e., 1.56 g cm^{-3}) was measured as:

$$d_b = \frac{W_{ds}}{V_c} \quad (5.1)$$

where d_b is the soil bulk density, W_{ds} the weight of dried soil in the container and V_c the volume of the container occupied by soil. In order to avoid that the container size affects the results of the penetration tests, we always used a container diameter (D_c) always more than 20 times of the probe diameter (D_p) [41].

During the experiments, all the developed probes were pushed in soil at 10 mm min^{-1} speed and up to 100 mm depth from their top using a UTM cross head. The resistance force was acquired by two types of load cells, $\pm 1 \text{ kN}$ and $\pm 50 \text{ N}$ with 0.001% of resolution. The probe was directly connected to load cell, where load cell was fixed on the cross head of UTM, as schematised in Figure 5.5.

The soil was taken out from the container and refilled after each trial to maintain constant test conditions (i.e., impedance, consistency, etc.) and to avoid particle jamming patterns [42].

5.2.6 Numerical simulations

Numerical simulations were carried out by employing the Discrete Element Method (DEM) [43]. The particles were randomly packed under the action of gravity in a cylindrical volume, constrained by frictional walls, while the probes were imported as Standard Triangulation Language (STL) meshes. The particle-particle and particle-wall collisions were modelled through a Hertz's contact law [44]. Each simulation is composed of two distinct steps: the packing of the particles, until a quasi-stationary state is reached, and the subsequent penetration of the probe at a constant velocity. In addition, we carried out five simulations with different random starting positions of

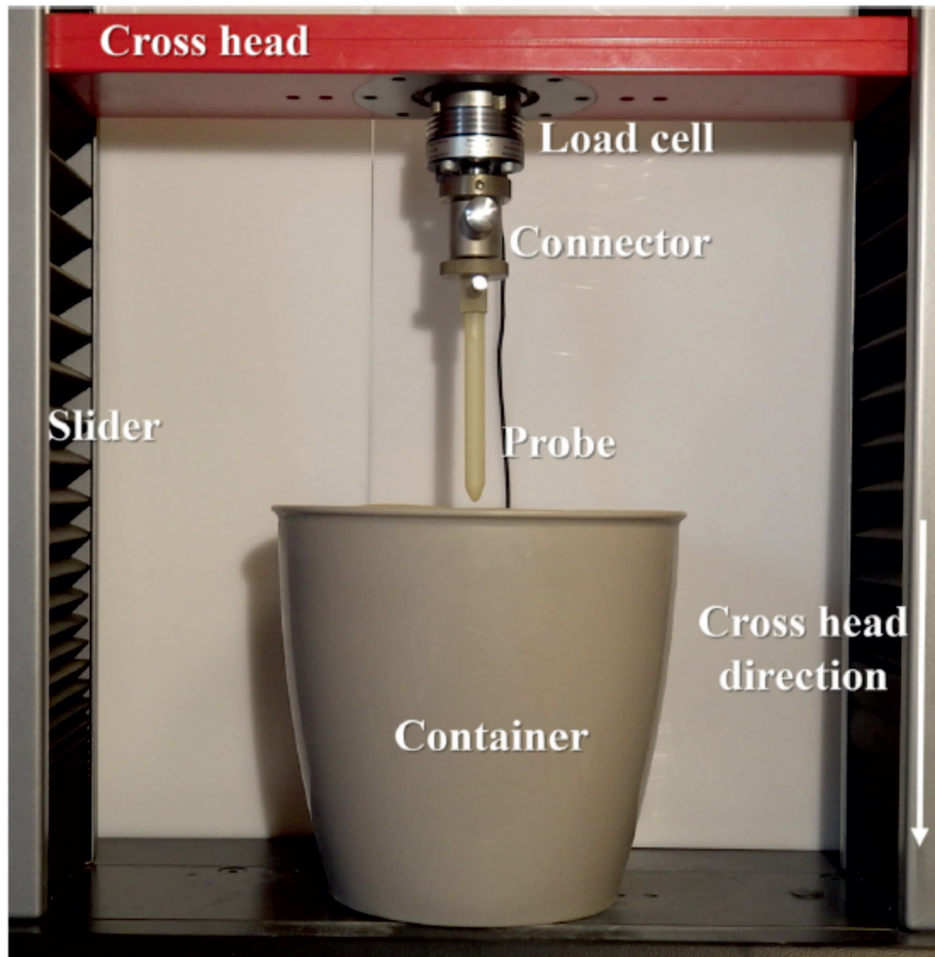


Figure 5.5: Experimental setup used for the penetration experiments.

the particles, thus all the results are presented with an average value and a standard deviation.

DEM simulations of large systems are extremely expensive from the computational point of view, thus here only the probes with diameter $D_p = 3$ mm were simulated, in order to reduce the computational volume. For the

same reason, the considered container is smaller than that used in experiments. Both choices, anyway, are not expected to affect the order relation among the different probe geometries. The effect of the probe diameter, in fact, as shown later for the experiments, has impact only on the absolute value of the forces, which scale roughly linearly with D_p . The effect of the container walls, instead, is discussed in detail in Appendix C.

The soil was approximated with a monodisperse distribution of spherical particles with an arbitrary choice of their diameter d , with $d \ll D_p$. The objective of the simulations carried out here, in fact, is to discriminate among the different probe shapes, whose order relation is not expected to change with the soil properties. Moreover, a similar DEM representation of soil has already been used in the literature, e.g., for the study of soil-tool interaction [45-47].

We assigned to the particles the typical mechanical properties of sand, while the choice of the microscale contact parameters is arbitrary and in the usual range of values employed in DEM studies. The probes were modelled as rigid bodies, thus neglecting elastic deformations. The chosen penetration speed (i.e., $v = 10 \text{ mm s}^{-1}$) is larger than the experimental value in order to reduce the duration of the simulations, since the total penetration force can be assumed to be nearly independent from v for small penetration velocities [42]. Additional details on the DEM simulations are reported in Appendix C. The study of the soil dynamics, which is anyway of little importance for quasi-static penetrations as in our case, is not an objective of the present work since it is not expected to change the qualitative performance and the differences among the considered probe geometries.

5.3 Results and discussion

5.3.1 Experimental penetration curves

The three-day old *Zea mays* roots, grown in air, showed a length of 81.62 ± 10.12 mm, a tip diameter of 0.88 ± 0.1 mm, and a root diameter of 1.19 ± 0.1 mm. The characteristic tip ratio is equal to 1.12 ± 0.07 .

After a fitting analysis, the function that better replicates the root tip morphology was a power law of the type ax^b , with $a = 2040$ and $b = -0.59$ (R²-value 0.9974). This mathematical function, together with the characteristic tip ratio, was used to design the CAD model of the bio-inspired probe.

Figure 5.6 shows a comparison of force penetration among different tip shapes with 7 mm diameter. During soil penetration, the graphs showed that the root-like probe needs 72%, 59%, 44% and 30% force less than the cylindrical, elliptical, parabolic and conical tips, respectively. The cylindrical probe showed the highest measured forces for all the different diameters, ranging from 96.18 to 8.28 N for probe diameters ranging from 11 to 3 mm, respectively. The root-like probe showed the lowest force for all the diameter probes tested, ranging from 71.98 to 6.02 N for probe diameters ranging from 11 to 3 mm of diameter probe, respectively.

As mentioned above, an ANOVA analysis was carried out to compare the gathered data. A statistically significant difference (p-value < 0.05) was found among the five artificial probes in correspondence of all the probe diameters.

A measure of the work needed for the penetration was also calculated as:

$$E = \int F(s)ds \quad (5.2)$$

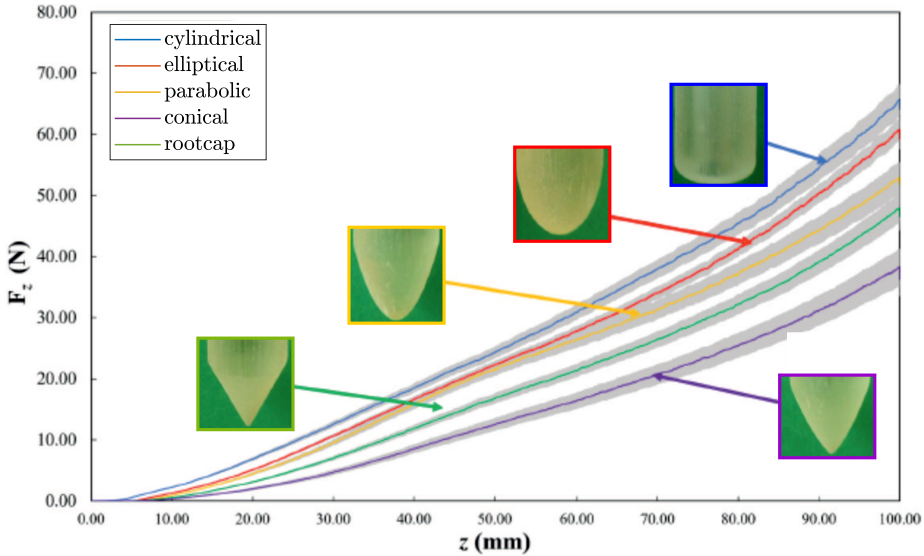


Figure 5.6: Experimental force-displacement curves for the 7 mm diameter probes, with maximum depth 100 mm and penetration speed 10 mm/min.

The cylindrical tip showed the worst performance in terms of expended work, ranging from 4.27 to 0.36 J for probe diameters ranging from 11 to 3 mm, respectively. Also, from an energetic point of view, the root-like probe expended the lowest work for penetration, ranging from 2.91 to 0.26 J for probe diameters ranging from 11 to 3 mm, respectively. Comparing the different probes, for example, in the example case of 7 mm diameter, root-like probe expended 89%, 67%, 54% and 35% less work than the cylindrical, elliptical, parabolic and conical probe, respectively.

5.3.2 Numerical penetration curves

Figure 5.7 presents the penetration curves, obtained by numerical simulations, of the considered probes up to 15 mm penetration depth. The results

are in good agreement with the experimental data, which return larger penetration forces for the cylindrical, elliptical and parabolic probes, in this order, while the conical and root-like probes present the smallest values.

The penetration depth shown in Figure 5.7 can be corrected to take into account the effect of the lateral walls: then the soil penetration curves can be rescaled as explained in Appendix C.

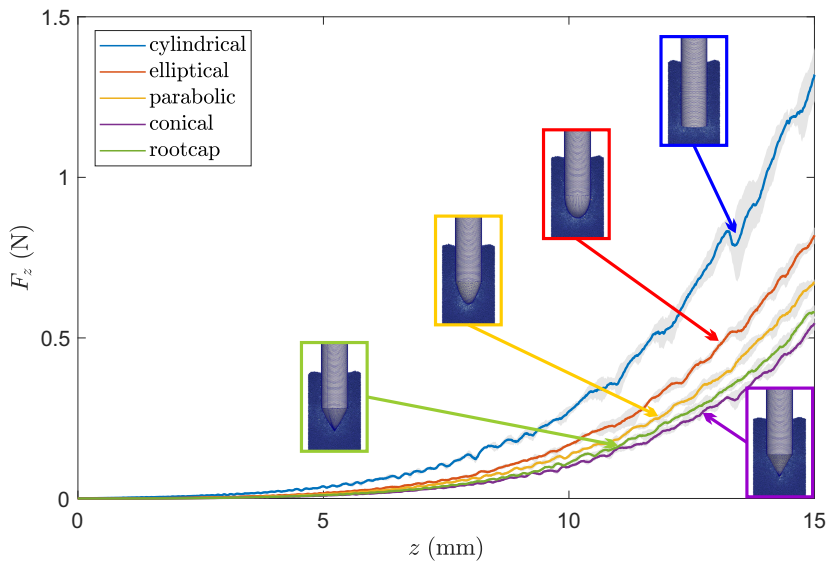


Figure 5.7: Numerical force-displacement curves for the 3 mm diameter probes, with maximum depth 15 mm and penetration speed 10 mm s^{-1} . The solid lines refer to the average values of five random simulations, the shaded areas to the standard deviations.

Table 5.1 reports the numerical values of the penetration force and the expended penetration work at 15 mm penetration depth, compared with the experimental data. Except for the parabolic probe, also the simulated

	Simulations	Experiments
Penetration force (N)		
Cylindrical	1.320 ± 0.083	0.752
Elliptical	0.819 ± 0.025	0.628
Parabolic	0.672 ± 0.009	0.608
Conical	0.545 ± 0.021	0.446
Root-like	0.581 ± 0.020	0.305
Expended penetration work (mJ)		
Cylindrical	4.03 ± 0.07	4.89
Elliptical	2.46 ± 0.04	3.90
Parabolic	2.01 ± 0.04	4.14
Conical	1.52 ± 0.01	1.58
Root-like	1.27 ± 0.01	1.28

Table 5.1: Comparison between the numerical and the experimental results: penetration forces and expended penetration works at 15 mm penetration depth.

values of the penetration work are in good agreement with those observed experimentally and fall in the same order of magnitude. Differences can be explained in the approximations introduced through numerical simulations, above all the description of the soil with spherical particles and the arbitrary values assigned to the microscale contact parameters, which can be tuned adequately to compensate the different considered volume.

5.3.3 Additional comments

The present Chapter aims at highlighting how the tip morphology of a penetrometer can affect its performance in real soil penetration. In particular, our study proves that an artificial probewith a plant root-like shape is more

efficient in terms of penetration force and expended work compared with standard shape probes (cylindrical, parabolic, elliptical or conical tip) at different sizes. Among the considered tip morphologies, as we expected, cylindrical probes showed, for all the five diameters tested, the worst performance. The root-like probes showed less penetration force, namely 34%, 49%, 72%, 38% and 37% with respect to a cylindrical tip in correspondence of 11, 9, 7, 5 and 3 mm probe diameters. Similarly, the root-like probes expended less work, namely 46%, 67%, 89%, 52% and 38%, in comparison with the cylindrical probes. Moreover, with the study of different diameters of the probe, we concluded that it varies linearly and could be used to select the probe size and shape for designing the robot for soil exploration according to soil types. Despite this performance, selected material for probe showed buckling behaviour for smaller diameters (i.e., ≤ 3 mm). Further studies will be dedicated to unveiling the importance of materials in these penetration tasks and to identify materials that are not affected by buckling behaviour. With this study, we demonstrated that the role of tip morphology is crucial for the penetration efficiency and provide an important cue of inspiration for future penetration systems. Also, our numerical simulations showed good agreement with the experimental data. Although the numerical simulations were not able to discriminate between conical and root-like probes because of the very small geometric difference and the considered particle diameter, the main result that the conical and root-like shapes are the optimal ones is retrieved.

Moreover, we found that the geometries with larger penetration forces present also higher values of the average contact number, i.e. the number of particles simultaneously in contact with a given central particle (see Appendix C). This result suggests that the local density of the granular medium, which can be related to the average contact number, might be one

of the key parameters controlling the penetration process. Therefore, the numerical simulations are potentially a useful tool for designing and optimizing new bio-inspired probe geometries.

Future research work in this direction should be addressed to the determination of the optimal parameters for simulating penetration mechanics in granular matter.

5.4 Conclusions

The methodological approach described in this Chapter can encourage a new research trend in the investigation of a possible correlation between root tip morphology and different plants habitat. In this study, we investigated *Zea mays*, one of the three most important cereal crops, together with wheat and rice. *Zea mays* can be found all over the world for its capability to grow in well-drained light (sandy), medium (loamy), and heavy (clay) soils. This versatility represents the first reason for which we have focused our studies on this plant. Its exceptional capability to penetrate various kinds of soil can, in fact, represent an amazing source of inspiration for artificial prototypes. Nevertheless, further studies on different plants, living in a different habitat, are required to shed light on the possibility to find *ad hoc* tip morphologies for each kind of soil and can provide exceptional design cues for developing innovative artificial prototypes.

Our findings can also contribute, beyond to the probe design benchmarks, to open discussion on the energetic efficiency issue in soil penetration, not still completely understood. Most of the existing studies in this field refer to the analysis of a projectile penetration in a solid medium: different geometries of the projectile have been investigated using empirical and semi-empirical models to predict the penetration depth [48-50]. Some other studies have

mainly been focused on the energetic analysis during static or dynamic penetration tests in geological strata. Guirgis *et al.* [51] have proposed an energy approach to study the penetration and an energy transfer to the rod by hammer using SPT. CPT or other dynamic penetration test methods have been investigated by other researchers [52-56]. Among all these studies, none has ever investigated the morphological features of plant roots in the penetration tasks.

References

- [1] Blake L.S., 2013. *Civil Engineer's Reference Book*. Elsevier, Amsterdam, The Netherlands.
- [2] Clayton C.R.I., Simons N.E., Matthews M.C., 1982. *Site Investigation*. Halsted Press, New York, United States of America.
- [3] Bar-Cohen Y., Zacny K., 2009. *Drilling in Extreme Environments - Penetration and sampling on Earth and other planets*. John Wiley & Sons, New York, United States of America.
- [4] Zacny K., Paulsen G., Chu P., Avanesyan A., Craft J., Szwarc T., 2012. Mars drill for the Mars sample return mission with a brushing and abrading bit, regolith and powder bit, core PreView Bit and a coring bit. *IEEE Aerospace Conference*, Big Sky, MT.
- [5] Gao Y., Ellery A., Jaddou M., Vincent J., Eckersley S., 2005. A novel penetration system for in situ astrobiological studies. *International Journal of Advanced Robotic Systems* 2, 281.
- [6] Zacny K., Bar-Cohen Y., Brennan M., Briggs G., Cooper G., Davis K., Dolgin B., Glaser D., Glass B., Gorevan S., Guerrero J., McKay C., Paulsen G., Stanley S., Stoker C., 2008. Drilling systems for extraterrestrial subsurface exploration. *Astrobiology* 8, 665.
- [7] Peck R.B., Hanson W.E., Thornburn T.H., 1974. *Foundation Engineering*. John Wiley & Sons, New York, United States of America.
- [8] Sanglerat G., 2012. *The Penetrometer and Soil Exploration*. Elsevier, Amsterdam, The Netherlands.

- [9] Rogers J.D., 2006. Subsurface exploration using the standard penetration test and the cone penetrometer test. *Environmental & Engineering Geoscience* 12, 161.
- [10] Wang Y., Huang K., Cao Z., 2013. Probabilistic identification of underground soil stratification using cone penetration tests. *Canadian Geotechnical Journal* 50, 766.
- [11] Robertson P., 1990. Soil classification using the cone penetration test. *Canadian Geotechnical Journal* 27, 151.
- [12] Jorat M., Kreiter S., Morz T., Moon V., de Lange W., 2014. Utilizing cone penetration tests for landslide evaluation. In Krastel S., Behrmann J.H., Volker D., Stipp M., Berndt C., Urgeles R., Chaytor J., Huhn K., Strasser M., Harbitz C.B. (eds) *Submarine Mass Movements and Their Consequences* Springer, Berlin, Germany.
- [13] Clayton C.R.I., 1995. The standard penetration test (SPT): methods and use. *Construction Industry Research and Information Association*.
- [14] Hunter J., Pullan S., Burns R., Gagne R., Good R., 1984. Shallow seismic reflection mapping of the overburden/bedrock interface with the engineering seismograph-some simple techniques. *Geophysics* 49, 1381.
- [15] Davis J., Annan A., 1989. Ground penetrating radar for high-resolution mapping of soil and rock stratigraphy. *Geophysical Prospecting* 37, 531.
- [16] Samouelian A., Cousin I., Tabbagh A., Bruand A., Richard G., 2005. Electrical resistivity survey in soil science: a review. *Soil and tillage research* 83, 173.
- [17] Bar-Cohen Y., Sherrit S., Dolgin B.P., Bao X., Chang Z., Pal D.S., Krahe R., Kroh J., Du S., Peterson T., 2001. Ultrasonic/sonic drilling/coring (USDC) for planetary applications. *SPIE Proceedings* 4327.
- [18] Tabbagh A., Dabas M., Hesse A., Panissod C., 2000. Soil resistivity: a non-invasive tool to map soil structure horizonation. *Geoderma* 97, 393.
- [19] Capetillo R.F., Sanchez J.R.V., Castro G.P., Perez A.E.O., Rivera F.C., Guillen R.C., Avila Luna F.A., Garcia M.V., 2014. Deep groundwater prospecting in Mexico City through seismic-reflection methodology. *The Leading Edge* 33, 758.
- [20] Yang S.Y., O’Cearbhaill E.D., Sisk G.C., Park K.M., Cho W.K., Villiger M., Bouma B.E., Pomahac B., Karp J.M., 2013. A bio-inspired swellable microneedle adhesive for mechanical interlocking with tissue. *Nature Communications* 4, 1702.

- [21] Thakoor S., 2000. Bio-inspired engineering of exploration systems. *Journal of Space Mission Architecture* 2, 49.
- [22] Moon S., Hwang S., Yoon S., Huh J., Hong D., 2013. Bio-inspired burrowing mechanism for underground locomotion control. *30th International Symposium on Automation and Robotics in Construction and Mining*.
- [23] Gouache T., Gao Y., Gourinat Y., Coste P., 2010. Wood wasp inspired space and earth drill. In Mukherjee D. (ed), *Biomimetics Learning from Nature*. InTech, Rijeka, Croatia.
- [24] Winter A.G., 2011. Biologically inspired mechanisms for burrowing in undersea substrates. PhD thesis, Massachusetts Institute of Technology.
- [25] Stone E.L., Kalisz P.J., 1991. On the maximum extent of tree roots. *Forest Ecology and Management* 46, 59.
- [26] Bengough A., McKenzie B., 1997. Sloughing of root cap cells decreases the frictional resistance to maize (*Zea mays L.*) root growth. *Journal of Experimental Botany* 48, 885.
- [27] Iijima M., Higuchi T., Barlow P.W., 2004. Contribution of root cap mucilage and presence of an intact root cap in maize (*Zea mays*) to the reduction of soil mechanical impedance. *Annals of Botany* 94, 473.
- [28] Iijima M., Morita S., Barlow P.W., 2008. Structure and function of the root cap. *Plant Production Science* 11, 17.
- [29] Bengough A.G., 2012. Root elongation is restricted by axial but not by radial pressures: so what happens in field soil?. *Plant and Soil* 360, 15.
- [30] Bengough A.G., Mullins C., 1990. Mechanical impedance to root growth: a review of experimental techniques and root growth responses. *Journal of Soil Science* 41, 341.
- [31] Abdalla A., Hettiaratchi D., Reece A., 1969. The mechanics of root growth in granular media. *Journal of Agricultural Engineering Research* 14, 236.
- [32] Mazzolai B., Mondini A., Corradi P., Laschi C., Mattoli V., Sinibaldi E., Dario P., 2011. A miniaturized mechatronic system inspired by plant roots for soil exploration. *Mechatronics - Transactions of IEEE/ASME* 16, 201.
- [33] Sadeghi A., Tonazzini A., Popova L., Mazzolai B., 2013. Robotic mechanism for soil penetration inspired by plant root. *IEEE International Conference on Robotics and Automation*.
- [34] Sadeghi A., Tonazzini A., Popova L., Mazzolai B., 2014. A novel growing device inspired by plant root soil penetration behaviors. *PLoS ONE* 9, e90139.

- [35] Sadeghi A., Mondini A., Mazzolai B., 2017. Toward self-growing soft robots inspired by plant roots and based on additive manufacturing technologies. *Soft Robotics* 4, 211.
- [36] Tonazzini A., Popova L., Mattioli F., Mazzolai B., 2012. Analysis and characterization of a robotic probe inspired by the plant root apex. *IEEE International Conference on Biomedical Robotics and Biomechanics*.
- [37] Misra R., Dexter A., Alston A., 1986. Maximum axial and radial growth pressures of plant roots. *Plant and Soil* 95, 315.
- [38] Schiefelbein J.W., 2000. Constructing a plant cell. The genetic control of root hair development. *Plant Physiology* 124, 1525.
- [39] Popova L., Russino A., Ascrizzi A., Mazzolai B., 2012. Analysis of movement in primary maize roots. *Biologia* 67, 517.
- [40] Creabis, 2016. Probe material properties used for fabrication by 3D printer.
- [41] Gui M.W., Bolton M., Garnier J., Corte J., Bagge G., Laue J., Renzi R., 1998. Guidelines for cone penetration tests in sand. *Centrifuge 98 International Conference*.
- [42] Stone M., Barry R., Bernstein D., Pelc M., Tsui Y., Schiffer P., 2004. Local jamming via penetration of a granular medium. *Physical Review E* 70, 041301.
- [43] Cundall P.A., Strack O.D.L., 1979. A discrete numerical model for granular assemblies. *Géotechnique* 29, 47.
- [44] Johnson K.L., 1985. *Contact Mechanics*. Cambridge University Press, Cambridge, United Kingdom.
- [45] Asaf Z., Rubinstein D., Shmulevich I., 2007. Determination of discrete element model parameters required for soil tillage. *Soil and Tillage Research* 92, 227.
- [46] Mak J., Chen Y., Sadek M., 2012. Determining parameters of a discrete element model for soil-tool interaction. *Soil and Tillage Research* 118, 117.
- [47] Tamas K., Jori I.J., Mouazen A.M., 2013. Modelling soil-sweep interaction with discrete element method. *Soil and Tillage Research* 134, 223.
- [48] Forrestal M., Altman B., Cargile J., Hanchak S., 1994. An empirical equation for penetration depth of ogive-nose projectiles into concrete targets. *International Journal of Impact Engineering* 15, 395.
- [49] Yankelevsky D.Z., Adin M.A., 1980. A simplified analytical method for soil penetration analysis. *International Journal for Numerical and Analytical Methods in Geomechanics* 4, 233.

- [50] Lixin Q., Yunbin Y., Tong L., 2000. A semi-analytical model for truncated-ogive-nose projectiles penetration into semi-infinite concrete targets. *International Journal of Impact Engineering* 24, 947.
- [51] Guirgis S., Guirgis E., 2009. An energy approach study of the penetration of concrete by rigid missiles. *Nuclear Engineering and Design* 239, 819.
- [52] Zarzojus G., Kelevisius K., Amsiejus J., 2013. Energy transfer measuring in dynamic probing test in layered geological strata. *Procedia Engineering* 57, 1302.
- [53] Odebrecht E., Schnaid F., Rocha M.M., de Paula Bernardes G., 2005. Energy efficiency for standard penetration tests. *Journal of Geotechnical and Geoenvironmental Engineering* 131, 1252.
- [54] Schnaid F., Odebrecht E., Rocha M.M., 2007. On the mechanics of dynamic penetration tests. *Geomechanics and Geoengineering* 2, 137.
- [55] Schnaid F., Odebrecht E., Rocha M.M., de Paula Bernardes G., 2009. Prediction of soil properties from the concepts of energy transfer in dynamic penetration tests. *Journal of Geotechnical and Geoenvironmental Engineering* 135, 1092.
- [56] Matsumoto T., Phan L.T., Oshima A., Shimono S., 2015. Measurements of driving energy in SPT and various dynamic cone penetration tests. *Soils and Foundations* 55, 201.

Chapter 6

Numerical analysis and optimisation of biosensors

6.1 Introduction

Spiders present a very complex and advanced sensing system, which allow them to accurately monitor and interact with the external environment. Spiders exploit their receptors to perform a variety of tasks, including catching preys [1-3], escaping from predators, detecting potential partners [4], laying their cocoon [5], etc. Several typologies of biosensors are present on a spider's exoskeleton and they can be divided in: mechanical (or tactile) [6-9], chemical [10,11] and air-flow [12-16] receptors. Hairs can interact with mechanical or aerodynamic excitations from the surrounding environment, providing the animal with accurate and real-time information. Specifically, the hair sensilla acting as air-flow sensors in arthropods are also known as trichobothria and they represent one of the most sensitive biosensors in Nature [17], being able to detect a minimum external work in the order of 10^{-21} J [18]. Klopsch *et al.* [19,20] have studied the flow perturbation generated by flying preys, demonstrating that their flight can be detected

by the spiders' trichobothria and thus induce the spider to jump toward the prey.

The transducing mechanism of spiders' receptors is very advanced [21] and a schematic view is shown in Figure 6.1, where the interaction with the substrate is schematised through a spring-dashpot model.

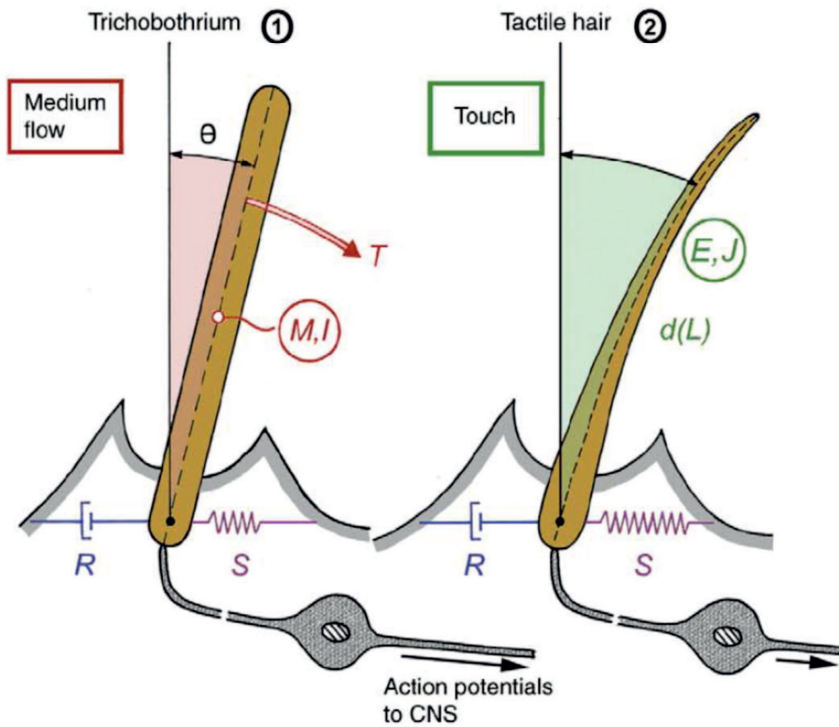


Figure 6.1: Schematic view of the working mechanism of an air flow-sensing hair (left) and of a tactile mechanoreceptor (right), with highlighted the viscoelastic spring-dashpot model. R represents the viscosity, S the stiffness, T the applied torque and E , M , d , L , J and I are the beam Young's modulus, mass, thickness, length and moments of inertia, respectively. Adapted from [8].

In the last decade, the observation of sensing systems in Nature has also inspired the development of bio-inspired sensors based, e.g., on micro electro-mechanical systems (MEMS) [22-26]. Several numerical simulation studies are available in the literature, mainly focused on the prediction of the sensor response or its vibrational properties (see, e.g., [27]).

However, numerical simulations of the actual biological structures, despite they can be extremely useful to get insight into the biosensor behaviour and performance, are still poorly addressed. Therefore, in this work we employ fluid-structure interaction (FSI) numerical simulations to study the properties of spiders' hairs in an air flow. We take the actual material properties of the trichobothria of a *Theraphosa stirmi* [28] of our collection and assume a simplified hair geometry. By varying the flow velocity and the longitudinal and transversal spacing of the hairs, we investigate the effects of the air flow and the geometry on the sensing capabilities. Results show that a linear response is obtained, verified also through simple analytical calculations. A brief dissertation on the optimal distribution of the hairs is also presented, thus paving the way towards more efficient and smart bio-inspired air-flow sensors.

6.2 Methods

6.2.1 Morphology and mechanical properties

The hairs are obtained from an exoskeleton of *Theraphosa stirmi* kept under controlled feeding and environmental conditions. The tested samples are prepared following the same procedure reported by Blackledge *et al.* [29]. We stick the hair samples on a paper frame provided with a square window of 5 mm side. The hair sample is fixed on the paper frame with a double-sided tape coupled with a glue.

For the morphology characterization by SEM, we use a Zeiss Supra 40 (Carl Zeiss AG, Germany) at 2.30 kV. The metallization is made by using a sputtering machine Q150T (Quorum Technologies Ltd, United Kingdom) and the sputtering mode is Pt/Pd 80:20 for 5 minutes. In addition, we employ optical microscopy (Carl Zeiss AG, Germany) at 10x magnification for the extraction of an average value of the hair diameter.

For the mechanical characterization, we use a T150 UTM nanotensile machine (Agilent Technologies Inc, United States of America) with a 500 mN load cell. The displacement speed is $10 \mu\text{m s}^{-1}$ with the frequency load at 20 Hz. The declared sensitivity of the machine is 10 nN for the load and 1 \AA for the displacement in the dynamic configuration.

6.2.2 Computational model

The FSI numerical simulations are carried out in COMSOL Multiphysics® (version 5.2a, COMSOL AB, Sweden). A two-way coupling algorithm is implemented here, in order to have a comprehensive understanding of the interaction between fluid flow and mechanical displacements [30]. Here, we consider three independent sensitivity analyses: (a) a single hair invested by a varying flow velocity, (b) two hairs at different longitudinal spacings and invested by a constant flow velocity, and (c) two hairs at different transversal spacings and, again, invested by a constant flow velocity.

Each hair has a complex geometry that here is approximated with a truncated cone of height $L = 1000 \mu\text{m}$, base diameter $D_b = 30 \mu\text{m}$ and tip diameter $D_t = 15 \mu\text{m}$, as shown in Figure 6.2. The computational domain for the fluid flow is composed of a three-dimensional box of width $100 \mu\text{m}$ and height $1200 \mu\text{m}$, with inlet and outlet positioned $1000 \mu\text{m}$ before and after the closest hair, respectively (i.e., a total length of $2L$). Moreover, a chitin of thickness $h = 100 \mu\text{m}$ is considered below the hair.

For convenience, here we assign linear elastic material properties, using a Young's modulus in the order of the measured values, i.e. $E = 600$ MPa. The Poisson's ratio and the material density, instead, are not available experimentally and therefore we take values close to those of chitin [31], i.e. $\nu = 0.25$ and $\rho_h = 1425$ kg m⁻³, respectively. The considered fluid is air at a temperature of 300 K, presenting density $\rho_a = 1.177$ kg m⁻³ and dynamic viscosity $\mu_a = 1.85 \cdot 10^{-5}$ kg m⁻¹s⁻¹ [32]. A constant fluid velocity is imposed at the inlet and the domain is delimited by walls with full-slip boundary conditions, in order to approximate an infinite transversal extension. The whole domain is discretized with about $4.5 \cdot 10^5$ tetrahedral elements, with a refinement at the base of each hair. For the analysis (a) above, the inlet flow velocity is chosen from 0.1 to 1 m s⁻¹ (with 0.1 m s⁻¹ steps), which is in the range of the velocity field measured around flying insects, thus can be representative of a real environmental condition. The analysis (b), instead, is performed by assuming a constant inlet velocity of 1 m s⁻¹ and considering two hairs separated by longitudinal distances Δs_l equal to 50, 100, 250, 500 and 1000 μm . Finally, the analysis (c) introduced above is carried out by imposing, again, a constant inlet velocity $u_{avg} = 1$ m s⁻¹ and considering two hairs located at a fixed longitudinal distance of 500 μm , but with transversal spacings Δs_t of 2.5, 5 and 10 μm . The effect of the air flow on the hair is quantified by monitoring the maximum hair tip displacement δ_{max} and the corresponding maximum von Mises stress σ_{max} , located at the hair base. In the analyses (b) and (c), the differences in σ_{max} and δ_{max} between the two hairs are computed. In these cases, the computational domain in Figure 2 is modified by assuming a total length of $2L + \Delta s_l$.

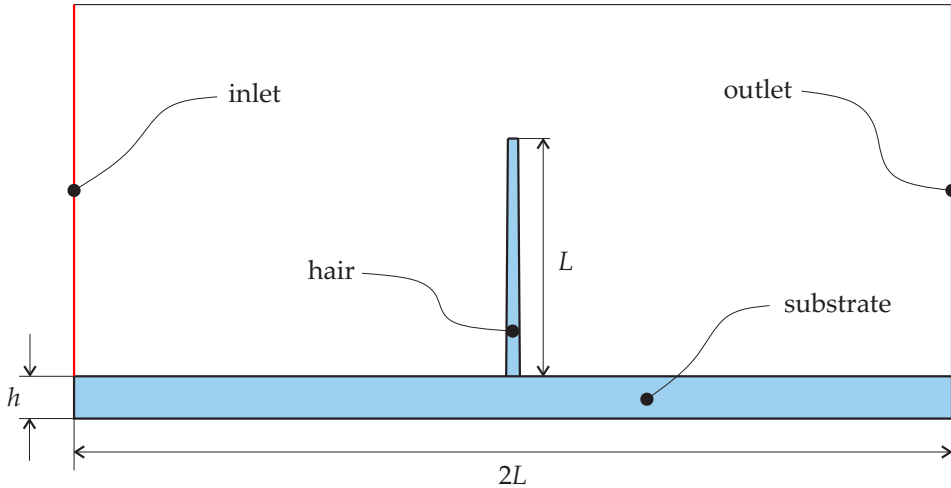


Figure 6.2: Lateral view of the 3D computational model considered in this study, with highlighted the fluid (white) and the solid (light blue) domains, as well as the inlet and outlet boundaries for the fluid flow.

6.3 Results and discussion

6.3.1 Hair properties

The SEM images of different hair typologies found on the spiders' exoskeleton are shown in Appendix D. We can observe a typical length from a few hundreds of μm to 1 – 2 mm and a variable diameter, with a tip size usually in the range $1 \div 20 \mu\text{m}$ and an average base diameter in the order of $30 \mu\text{m}$. The typical hair spacing is a few mm, i.e., in the order of the hair length. Usually, shorter hairs not involved in flow-sensing are also present on the spider's cuticle and are not shown here, for brevity.

The stress-strain curves extracted from the nanotensile test on different hairs are also shown in Appendix D. The mechanical properties of the hairs are intrinsically variable, because of their biological nature, and we have

measured an initial Young's modulus in the range $500 \div 800$ MPa using linear regression, with a fracture strain in the order of 0.5 mm mm^{-1} .

6.3.2 Effect of a varying flow velocity

Figure 6.3 shows the values of σ_{max} and δ_{max} as function of the mean inlet velocity, as well as the von Mises stress distribution together with qualitative flow streamlines. Both the stress and the displacement scale almost linearly with u_{avg} and the two curves can be fitted by the following laws:

$$\delta_{max} = K_{\delta} u_{avg} \quad (6.1a)$$

$$\sigma_{max} = K_{\sigma} u_{avg} \quad (6.1b)$$

for the maximum displacement and the maximum von Mises stress, respectively. We obtain the following values of the fitting parameters: $K_{\delta} \approx 1.943 \cdot 10^{-6} \text{ s}$ (R²-value 0.9944) and $K_{\sigma} \approx 67840 \text{ kg m}^{-2}\text{s}^{-1}$ (R²-value 0.9917). Note that also a more general power law can be used for fitting, e.g. $\delta_{max} = K_{\delta 1} u_{avg}^{K_{\delta 2}}$ for the displacement. From this latter equation, we get $K_{\delta 1} = 2.014 \text{ m}^{-0.119}\text{s}^{1.119}$ and the fitting exponent $K_{\delta 2} = 1.119$ (R²-value 1), thus the linear trend assumed above can be considered sufficiently precise. Similarly, considering a law of the type $\sigma_{max} = K_{\sigma 1} u_{avg}^{K_{\sigma 2}}$ for the stress, we get $K_{\sigma 1} = 70940 \text{ kg m}^{-2.149}\text{s}^{-0.815}$ and $K_{\sigma 2} = 1.149$ (R²-value 1), confirming the goodness of the linear assumption. Note that, interestingly, we find $K_{\delta 2} \approx K_{\sigma 2}$ and therefore the proportionality between the maximum stress and the maximum displacement is confirmed, i.e. $\sigma_{max} \approx \frac{K_{\sigma 1}}{K_{\delta 1}} \delta_{max}$.

Equations (6.1) can be derived analytically considering the mechanical loads exerted by the flow. For simplicity, here we approximate the truncated cone geometry of the hair by a cylindrical beam, with constant diameter $D_{avg} = (D_b + D_t)/2$, clamped at one end. We believe that neglecting the

compliance of the substrate does not influences heavily the results: specifically, in this way we are overestimating the maximum von Mises stress and underestimating the maximum displacement, as will be demonstrated later.

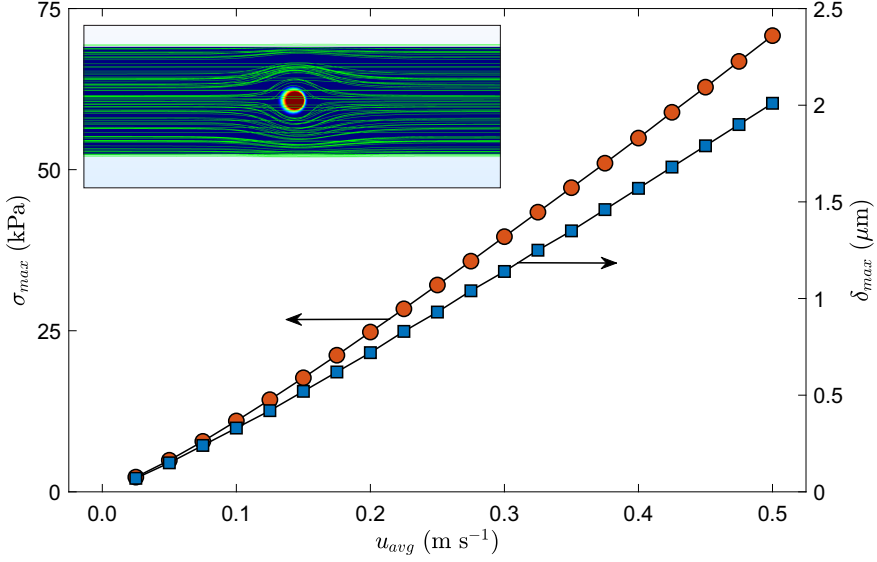


Figure 6.3: Maximum von Mises stress (red dots) and maximum displacement (blue squares) as function of the inlet velocity. Inset: Top view of the qualitative streamlines and displacement field of a hair.

The flow can be assumed, in a first approximation, to exert a constant drag force per unit length of the beam given by:

$$f_D = \frac{1}{2} C_D \rho_a D_{avg} u_{avg}^2 \quad (6.2)$$

being C_D the (dimensionless) drag coefficient.

Neglecting the shear deformation, the displacement at the hair tip is given

by:

$$\delta_{max} \approx \frac{f_D L^4}{8EI} = \frac{4\rho_a C_D L^4}{\pi E D_{avg}^3} u_{avg}^2 \quad (6.3)$$

where we have used the expression of the maximum bending moment, equal to $f_D L^2/2$, and the moment of inertia of the section, i.e. $I = \pi D_{avg}^4/64$. For a cylinder immersed in a laminar flow, considering low Reynolds numbers Re and constant fluid properties, the drag coefficient depends on the flow velocity as [33]:

$$C_D = C_D(u_{avg}) = K' Re^{-1} = K' \frac{\mu_a}{\rho_a u_{avg} D_{avg}} \quad (6.4)$$

being K' a constant of proportionality. Therefore, inserting Equation (6.4) into Equation (6.3), we retrieve the observed quasi-linear relation between maximum displacement and inlet velocity.

An analogous reasoning can be made on the von Mises stress. Considering, again, only bending and neglecting shear stresses, we can assume:

$$\sigma_{max} \approx \frac{f_D L^2}{2I} \frac{D_{avg}}{2} = \frac{8\rho_a C_D L^2}{\pi D_{avg}^2} u_{avg}^2 \quad (6.5)$$

Inserting Equation (6.4) into Equation (6.5), we retrieve again the linear law in Equations (6.1).

Comparing Equations (6.3) and (6.5) with Equations (6.1), we can write the explicit expressions of the fitting parameters introduced above, respectively:

$$K_\delta \approx \frac{4\mu_a L^4}{\pi E D_{avg}^4} K'_\delta \quad (6.6a)$$

$$K_\sigma \approx \frac{8\mu_a L^2}{\pi D_{avg}^3} K'_\sigma \quad (6.6b)$$

where K'_δ and K'_σ are the constants of proportionality between C_D and Re^{-1} , as in Equation (6.4), for displacements and stresses, respectively.

Computing K'_δ and K'_σ from Equations (6.6), we get the following estimations of the drag coefficient:

$$C_D^{(min)} = K'_\delta \text{Re}^{-1} \approx 12.7 \text{Re}^{-1} \quad (6.7a)$$

$$C_D^{(max)} = K'_\sigma \text{Re}^{-1} \approx 16.4 \text{Re}^{-1} \quad (6.7b)$$

which represent, respectively, a lower bound from the (underestimated) maximum displacement and an upper bound from the (overestimated) maximum von Mises stress. This result is consistent with the reasoning anticipated above and the computed constants of proportionality fall within the range of the data available in the literature, e.g., for perfect spheres or cylinders [33]. Differences can be attributed to the introduced approximations, i.e., the cylindrical instead of the conical geometry and the finite-length body.

6.3.3 Effect of a varying hair spacing

Figure 6.4 shows the effect of a varying longitudinal spacing on the hair response, quantified through the variations $\Delta\sigma_{max}/\sigma_{1,max}$ and $\Delta\delta_{max}/\delta_{1,max}$, being $\Delta\sigma_{max}$ and $\Delta\delta_{max}$ the differences in maximum stresses and displacements between the first (i.e., the closest to the inlet) and the second hair, and $\sigma_{1,max}$ and $\delta_{1,max}$ the maximum stress and maximum displacement, respectively, related to the first hair.

For small values of Δs_l the aerodynamic wake behind the first hair reduces the stresses and displacements to which the second hair is subjected. Therefore, for small longitudinal spacings there is a significant variation in σ_{max} and δ_{max} , while this difference becomes considerably smaller (i.e., below 10%, which could be considered acceptable for the sensing system) when Δs_l is in the order of half-length of the hair (i.e., around 500 μm for

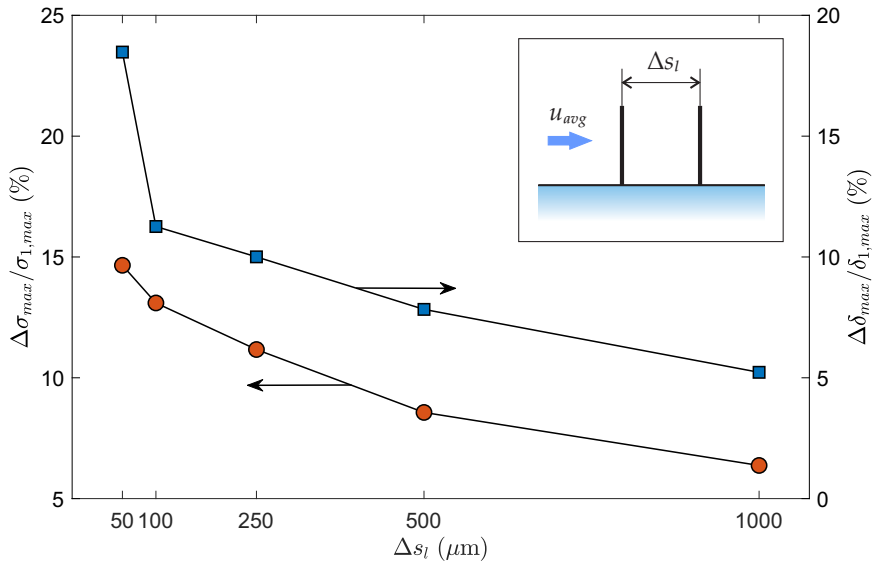


Figure 6.4: Difference in the maximum von Mises stresses and maximum displacements between the first and the second hair, as function of the longitudinal spacing. Inset: Schematic lateral view of the considered arrangement of the hairs, with the light blue area representing the spider's exoskeleton.

the two 1000 μm hairs considered here). Note that this result has been obtained considering the maximum inlet flow velocity, i.e. $u_{avg} = 1 \text{ m s}^{-1}$. For smaller values of u_{avg} , $\Delta\sigma_{max}$ and $\Delta\delta_{max}$ are expected to be lower due to a shorter aerodynamic wake, thus the sensing system is effective also for smaller values of the longitudinal spacing.

For the example case $\Delta s_l = 100 \mu\text{m}$, Figure 6.5 shows the displacement field and the von Mises stresses of two trichobothria, highlighting the influence of the first hair on the second one.

Figure 6.6, instead, reports the effect of a varying transversal spacing, quantified again in terms of $\Delta\sigma_{max}/\sigma_{1,max}$ and $\Delta\delta_{max}/\delta_{1,max}$ between the

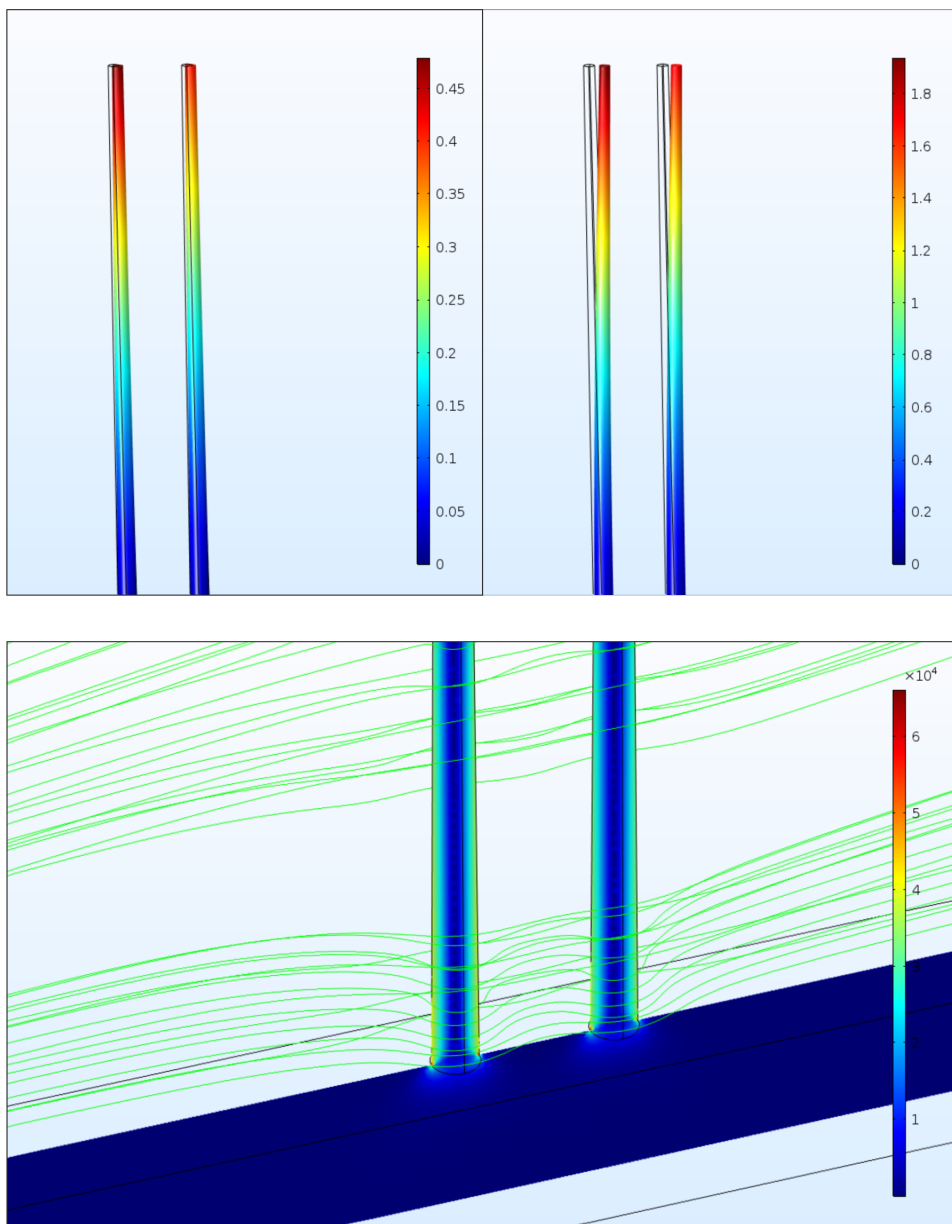


Figure 6.5: Displacement and stress fields for two trichobothria with $\Delta s_l = 100 \mu\text{m}$ and $\Delta s_t = 0 \mu\text{m}$. Top: Difference in maximum displacement for $u_{avg} = 0.3 \text{ m s}^{-1}$ (left) and $u_{avg} = 1 \text{ m s}^{-1}$. Dimensions in μm . The displacement is scaled of 10 times for visualization purposes. Bottom: Stress field at the base of the hairs and in the substrate, and flow streamlines for $u_{avg} = 0.3 \text{ m s}^{-1}$.

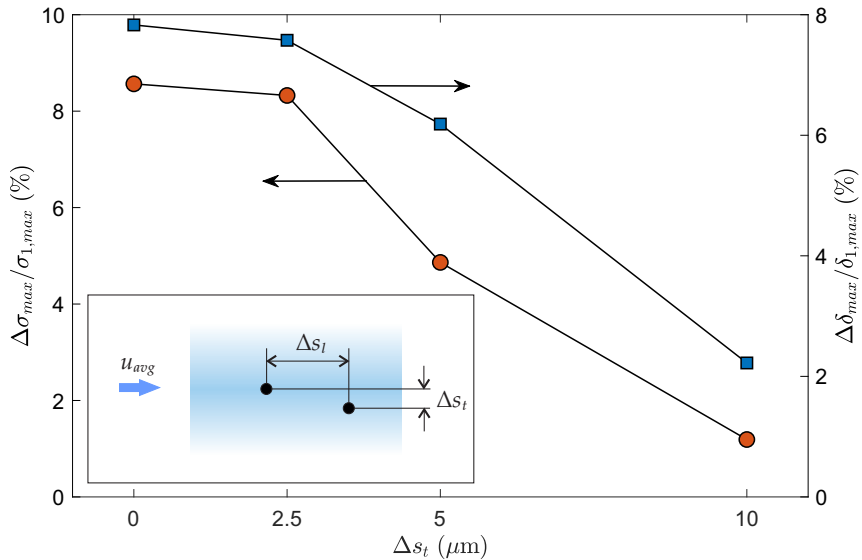


Figure 6.6: Difference in the maximum von Mises stresses and maximum displacements between the first and the second hair, as function of the transversal spacing. Inset: Schematic top view of the considered arrangement of the hairs, with the light blue area representing the spider's exoskeleton.

first and the second hair. Again, smaller spacings lead to greater disturbances between the hairs, anyway the absolute value of the variations is always below 10% and is considerably smaller if considering the effect of the longitudinal spacing discussed above. This means that the transversal position of the hairs does not affect significantly their sensing capabilities, keeping almost the same response in terms of stresses and displacements even when they are perfectly in line (i.e., $\Delta s_t = 0 \mu\text{m}$). Note that also in this case we have considered an example condition of maximum flow velocity and fixed longitudinal spacing: however the results can be representative of a general trend also for different values of u_{avg} and Δs_l .

The results shown in Figures 6.4 and 6.5 suggest that the relative position of flow-sensing hairs is probably dictated by the mutual interference. Therefore, spiders present an optimal configuration to maximize their sensing performance: this happens when there is the maximum density of hairs (i.e. number of hairs per unit area of the substrate) capable of sensing a certain level of stress.

6.3.4 Estimation of the optimal hair density

Here we attempt to derive a simple analytical model to compute the optimal density of spiders' trichobothria. Let us consider a function of the type:

$$\frac{\Delta\sigma_{max}}{\sigma_{1,max}} = e^{-\alpha S^\beta} \quad (6.8)$$

to fit the numerical curve shown in Figure 6.4. α and β are fitting parameters, while $S = \Delta s_l/L$ is the dimensionless longitudinal spacing. Note that Equation (6.8) allows to correctly predict a 100% stress variation for an ideally zero spacing, whereas a negligible variation for a certain critical distance $S^* = 1/\alpha$, i.e., for which the disturbance of the first hair on the second one becomes ideally zero. Considering a certain area A of the spider's exoskeleton, the number of trichobothria on this area can be expressed by the quantity:

$$N = \frac{A}{\Delta s_l^2} = \frac{A}{L^2 S^2} \quad (6.9)$$

Now we define the total sensitivity Γ of the sensing system as the sum of the inverse of the variations:

$$\Gamma = \sum_N \frac{1}{\Delta\sigma_{max}/\sigma_{1,max}} = \frac{N}{\Delta\sigma_{max}/\sigma_{1,max}} = \frac{A e^{\alpha S^\beta}}{L^2 S^2} \quad (6.10)$$

Thus, the maximum sensitivity can be found by equaling to zero the first-order derivative of Equation (6.10) with respect to S , i.e.:

$$S = \frac{2}{\alpha} \frac{1}{\beta} \quad (6.11)$$

The numerical fit of the experimental data shown in Figure 6.5 gives, in Equation (6.8), $\alpha \approx 2.659$ and $\beta \approx 0.1139$, with R^2 -value 0.9998. Consequently, from Equation (6.11), we obtain $S \approx 0.08$: this means that, in principle, spiders trichobothria should be placed at a distance in the order of the 10% of the hair length. This result is in very good agreement with the experimental evidence, since it is possible to observe $S \sim 10^{-1}$ on spiders' legs (see, e.g., Figure 6.1 in [34]). Note that the result is obviously sensitive to the best fit of the numerical (or, if available, experimental) data and to the choice of the function in Equation (6.8): we believe other solutions are possible, anyway without changing the main outcome of this study.

In fact, a possible variation of the fitting parameters in the ranges $\alpha = 1 \div 15$ and $\beta = 0.1 \div 2$, for instance, does not modify heavily the order-of-magnitude estimation of S . Note also that a better estimation could be obtained considering (i) different velocity ranges, since presumably actual spiders' trichobothria must work optimally in any condition (while the results in Figure 6.4, and thus the estimation through Equation (6.11), are related only to $u_{avg} = 1 \text{ m s}^{-1}$), and (ii) more complex phenomena that may arise and are not taken into account in this study, e.g. viscosity-mediated coupling [12,35].

Finally, the simple analytical model we have built shows a very promising potential in capturing the most important factors affecting the sensitivity of spiders' trichobothria and thus in determining optimal configurations in flow-sensing systems.

6.4 Conclusions

We have used FSI numerical simulations to investigate the behavior of *Theraphosa stirmi*'s trichobothria under a fluid flow. We have extracted the morphology and the elastic properties of the hairs from previous experimental tests. By analysing the mechanical response of the hair under a varying flow velocity, we have highlighted that both the maximum hair displacement and the maximum von Mises stress present a linear response for increasing u_{avg} . The considered simplification of the hair geometry has allowed, anyway, to obtain a good representation of the aerodynamic performance, as demonstrated analytically.

From the evaluation of different longitudinal and transversal hair spacings, we have found that the wake behind the first hair affects the sensing capability of the second one. Therefore, this suggests that the optimal hair spacing in spiders might derive from fluid dynamic reasons and from the need of maximizing the sensing performance. A simple model confirms the observations in Nature.

These results can be of interest for the optimal design of novel bio-inspired smart sensors and structures for fluid flow measurements and advanced applications in robotics.

References

- [1] Jackson R.R., Pollard S.D., 1996. Predatory behavior of jumping spiders. *Annual Review of Entomology* 41, 287.
- [2] Nentwig W., 1985. Social spiders catch larger prey: a study of *Anelosimus eximius* (Araneae: Theridiidae). *Behavioral Ecology and Sociobiology* 17, 79.
- [3] Pugno N.M., 2018. Spider weight dragging and lifting mechanics. *Meccanica* 53, 1105.

- [4] Barth F.G., 1993. Sensory guidance in spider pre-copulatory behaviour. *Comparative Biochemistry and Physiology A* 104, 717.
- [5] Chiavazzo E., Isaia M., Mammola S., Lepore E., Ventola L., Asinari P., Pugno N.M., 2015. Cave spiders choose optimal environmental factors with respect to the generated entropy when laying their cocoon. *Scientific Reports* 5, 7611.
- [6] Foelix R.F., Chu-Wang I.W., 1973. The morphology of spider sensilla. I. Mechanoreceptors, *Tissue & Cell* 5, 451.
- [7] Albert J.T., Friedrich O.C., Dechant H.E., Barth F.G., 2001. Arthropod touch reception: spider hair sensilla as rapid touch detectors. *Journal of Computational Physiology A* 187, 303.
- [8] Barth F.G., 2004. Spider mechanoreceptors. *Current Opinion in Neurobiology* 14, 415.
- [9] Fratzl P., Barth F.G., 2009. Biomaterial systems for mechanosensing and actuation. *Nature* 462, 442.
- [10] Foelix R.F., 1970. Chemosensitive hairs in spiders. *Journal of Morphology* 132, 313.
- [11] Foelix R.F., Chu-Wang I.W., 1973. The morphology of spider sensilla. II. Chemoreceptors. *Tissue & Cell* 5, 461.
- [12] Bathellier B., Barth F.G., Albert J.T., Humphrey J.A.C., 2005. Viscosity-mediated motion coupling between pairs of trichobothria on the leg of the spider *Cupennius salei*. *Journal of Computational Physiology A* 191, 733.
- [13] Humphrey J.A.C., Barth F.G., 2007. Medium flow-sensing hairs: biomechanics and models. *Advances in Insect Physiology* 34, 1-80.
- [14] Kant R., Humphrey J.A.C., 2009. Response of cricket and spider motion-sensing hairs to airflow pulsations. *Journal of the Royal Society Interface* 6, 1047.
- [15] Santer R.D., Hebets E.A., 2011. Evidence for air movement signals in the agonistic behaviour of a nocturnal arachnid (order Amblypygi). *PLoS ONE* 6, e22437.
- [16] Bathellier B., Steinmann T., Barth F.G., Casas J., 2012. Air motion sensing hairs of arthropods detect high frequencies at near-maximal mechanical efficiency. *Journal of the Royal Society Interface* 9, 1131.
- [17] Barth F.G., 2002. Spider senses technical perfection and biology. *Zoology* 105, 271.

- [18] Barth F.G., 2000. How to catch the wind: spider hairs specialized for sensing the movement of air. *Naturwissenschaften* 87, 51.
- [19] Klopsch C., Kuhlmann H.C., Barth F.G., 2012. Airflow elicits a spider's jump towards airborne prey. I. Airflow around a flying blowfly. *Journal of the Royal Society Interface* 9, 2591.
- [20] Klopsch C., Kuhlmann H.C., Barth F.G., 2013. Airflow elicits a spider's jump towards airborne prey. II. Flow characteristics guiding behaviour. *Journal of the Royal Society Interface* 10, 20120820.
- [21] P. G orner, 1965. A proposed transducing mechanism for a multiply-innervated mechanoreceptor (trichobothrium) in spiders. *Cold Spring Harbor Symposia on Quantitative Biology* 30, 69.
- [22] Dijkstra M., van Baar J.J., Wiegerink R.J., Lammerink T.S.J., de Boer R.J.H., Krijnen G.J.M., 2005. Artificial sensory hairs based on the flow sensitive receptor hairs of crickets. *Journal of Micromechanics and Microengineering* 15, S132.
- [23] Krijnen G.J.M., Dijkstra M., van Baar J.J., Shankar S.S., Kuipers W.J., de Boer R.J.H., Altpeter D., Lammerink T.S.J., Wiegerink R., 2006. MEMS based hair flow-sensors as model systems for acoustic perception studies. *Nanotechnology* 17, S84.
- [24] Barbier C., Humphrey J.A.C., Paulus J., Appleby M., 2007. Design, fabrication and testing of a bioinspired hybrid hair-like fluid motion sensor array. *Proceedings of IMECE 2007 - ASME International Mechanical Engineering Congress and Exposition* 8, 1319.
- [25] Casas J., Steinmann T., Krijnen G.J.M., 2010. Why do insects have such a high density of flow-sensing hairs? Insights from the hydromechanics of biomimetic MEMS sensors. *Journal of the Royal Society Interface* 7, 1487.
- [26] Abels C., Qualtieri A., Lober T., Mariotti A., Chambers L.D., De Vittorio M., Mengill W.M., Rizzi F., 2019. Bidirectional biomimetic flow sensing with antiparallel and curved artificial hair sensors. *Beilstein Journal of Nanotechnology* 10, 32.
- [27] Yang B., Hu D., Wu L., 2016. Design and analysis of a new hair sensor for multi-physical signal measurement. *Sensors* 16, 1056.
- [28] Guadanucci J.P.L., 2012. Trichobothrial morphology of Theraphosidae and Barychelidae spiders (Araneae, Mygalomorphae). *Zootaxa* 3439, 1.

- [29] Blackledge T.A., Swindeman J.E., Hayashi C.Y., 2005. Quasistatic and continuous dynamic characterization of the mechanical properties of silk from the cobweb of the black widow spider *Latrodectus hesperus*. *Journal of Experimental Biology* 208, 1937.
- [30] Benra F.K., Dohmen H.J., Pei J., Schuster S., Wan B., 2011. A comparison of one-way and two-way coupling methods for numerical analysis of fluid-structure interactions. *Journal of Applied Mathematics* 2011, 853560.
- [31] Fabritius H., Sachs C., Raabe D., Nikolov S., Friák M., Neugebauer J., 2011. Chitin in the exoskeletons of arthropoda: from ancient design to novel materials science, In: Gupta N.S. (ed) *Chitin - Formation and Diagenesis*, Springer, Berlin, Germany.
- [32] Dry Air Properties, 2005. *Engineering ToolBox*.
- [33] Anderson J.D., 1991. *Fundamentals of Aerodynamics*. McGraw-Hill, New York, United States of America.
- [34] McConney M.E., Schaber C.F., Julian M.D., Eberhardt W.C., Humphrey J.A.C., Barth F.G., Tsukruk V.V., 2009. Surface force spectroscopic point load measurements and viscoelastic modelling of the micromechanical properties of air flow sensitive hairs of a spider (*Cupiennius salei*). *Journal of the Royal Society Interface* 6, 681-694.
- [35] Barth F.G., 2014. The slightest whiff of air: Airflow sensing in arthropods. In: Blackmann H., Mogdans J., Coombs S.L. (eds) *Flow Sensing in Air and Water*. Springer, Berlin, Germany.

Chapter 7

Conclusions

In this Doctoral Thesis we have presented the highly multiphysics and multiscale nature of tribological phenomena, where the observed macroscopic properties are governed by interactions over multiple length and time scales [1].

In a recent paper [2], Popov confirms that the current know-how in tribology and contact mechanics have made available modelling and simulation tools that allow a precise description of elastic contacts, despite real-life problems involve the complex interplay of friction, wear, adhesion and lubrication. Therefore, together with the recent rapid advances in life sciences and micro- and nanotechnologies, tribology is going to live a "golden age" in the coming years, with the need of modelling and simulation tools of increasing performance.

The "problem of the third body" is seen as an urgent need in tribology and one of its most important challenges. The characterisation and understanding of third-body friction, in fact, can shed light on how surface topography and the frictional properties evolve over time and thus provide new insights into a series of phenomena such as wear formation, boundary

and solid lubrication, tribochemistry and corrosion, etc. In this Doctoral Thesis, we have attempted to describe third-body frictional sliding, which could be further extended by considering more complex interactions, e.g. by including heat transfer and/or chemical reactions.

However, we believe that the next grand challenge in tribology is the development of smart sliding interfaces with tunable friction. Recent works have shown that some materials (e.g. polymer brushes [3], carbon-based nanomaterials [4,5], hydrogels [6,7]) can be engineered, also by following bio-inspired strategies, to partly switch between small and large-friction states. Within this frame, in this Doctoral Thesis we have demonstrated how to exploit material property gradients, i.e., functionally graded materials, to tune the static and dynamic coefficients of friction [8].

This approach could represent an important breakthrough not only in many industrial applications (e.g., the design of advanced carbon-based coatings for power transmission systems), but also in the design of devices for soft robotics and material penetration [9], of micro electro-mechanical systems (MEMS)-based sensors [10] or of surfaces for fluid-dynamic drag reduction.

Furthermore, we have managed to capture the basic phenomena governing the macroscopic behaviour of tribological systems, essentially by employing similar and relatively simple numerical methods. These are based on few microscale control parameters, but have been demonstrated to be sufficiently powerful for the purpose of the works discussed. This has allowed to predict the performance also of quite different systems, only by changing the geometry or the boundary or initial conditions.

Finally, we can suggest that the coupling of the precise control of the performance of a tribological interface to a bio-inspired optimisation approach, can offer novel possibilities towards the design of advanced and smart solutions for innovative tribo-materials and sliding interfaces.

References

- [1] Vakis A.I., Yastrebov V.A., Scheibert J., Nicola L., Dini D., Minfray C., Almqvist A., Paggi M., Lee S., Limbert G., Molinari J.F., Anciaux G., Aghababaei R., Echeverri Restrepo S., Papangelo A., Cammarata A., Nicolini P., Putignano C., Carbone G., Stupkiewicz S., Lengiewicz J., Costagliola G., Bosia F., Guarino R., Pugno N.M. Müser M.H., Ciavarella M. (2018) Modeling and simulation in tribology across scales: An overview. *Tribology International* 125, 169.
- [2] Popov V.L. (2018) Is tribology approaching its golden age? Grand challenges in engineering education and tribological research. *Frontiers in Mechanical Engineering* 4, 16.
- [3] de Beer S. (2014) Switchable friction using contacts of stimulus-responsive and nonresponding swollen polymer brushes. *Langmuir* 30, 8085.
- [4] Dickrell P.L., Pal K.L., Bourne G.R., Muratore C., Voevodin A.A., Ajayan P.M. Schadler L.S., Sawyer W.G. (2006) Tunable friction behavior of oriented carbon nanotube films. *Tribology Letters* 24, 85.
- [5] Gallagher P., Lee M., Amet F., Maksymovych P., Wang J., Wang S., Lu X., Zhang G., Watanabe K., Taniguchi T., Goldhaber-Gordon D. (2016) Switchable friction enabled by nanoscale self-assembly on graphene. *Nature Communications* 7, 10745.
- [6] Ma S., Scaraggi M., Wang D., Wang X., Liang Y., Liu W., Dini D., Zhou F., 2015. Nanoporous substrate infiltrated hydrogels: a bioinspired regenerable surface for high load bearing and tunable friction. *Advanced Functional Materials* 25, 7366.
- [7] Ma S., Scaraggi M., Lin P., Yu B., Wang D., Dini D., Zhou F., 2017. Nanohydrogel brushes for switchable underwater adhesion. *Journal of Physical Chemistry C* 121, 8452.
- [8] Guarino R., Costagliola G., Bosia F., Pugno N.M. (2018) Evidence of friction reduction in laterally graded materials. *Beilstein Journal of Nanotechnology* 9, 2443.
- [9] Mishra A.K., Tramacere F., Guarino R., Pugno N.M., Mazzolai B. (2018) A study on plant root apex morphology as a model for soft robots moving in soil. *PLoS ONE* 13, e0197411.
- [10] Guarino R., Greco G., Mazzolai B., Pugno N.M. (2019) Fluid-structure interaction study of spider's hair flow-sensing system. *Materials Today: Proceedings* 7, 418.

Appendix A

Details of sliding friction simulations

Computed values of the global static coefficients of friction

Δ	SBM	FEM
-0.4	0.6198	0.7080
-0.3	0.6501	0.7128
-0.2	0.7458	0.7321
-0.1	0.8346	0.8237
0.0	0.9124	0.9124
0.1	0.8336	0.8640
0.2	0.7442	0.7776
0.3	0.6491	0.6835
0.4	0.6212	0.6746

Table A.1: Tables reporting the computed absolute values of the global static coefficient of friction μ_s , as function of Δ and obtained through the SBM and the FEM, for the case of gradients in the local coefficients of friction.

Δ	SBM	FEM
-0.4	0.6725	0.6844
-0.3	0.7236	0.7197
-0.2	0.7789	0.7756
-0.1	0.8509	0.8451
0.0	0.9124	0.9124
0.1	0.8494	0.8325
0.2	0.7808	0.7667
0.3	0.7251	0.7500
0.4	0.6754	0.7278

Table A.2: Tables reporting the computed absolute values of the global static coefficient of friction μ_s , as function of Δ and obtained through the SBM and the FEM, for the case of gradients in the material Young's modulus.

Effect of the FE element type on the surface stress distributions

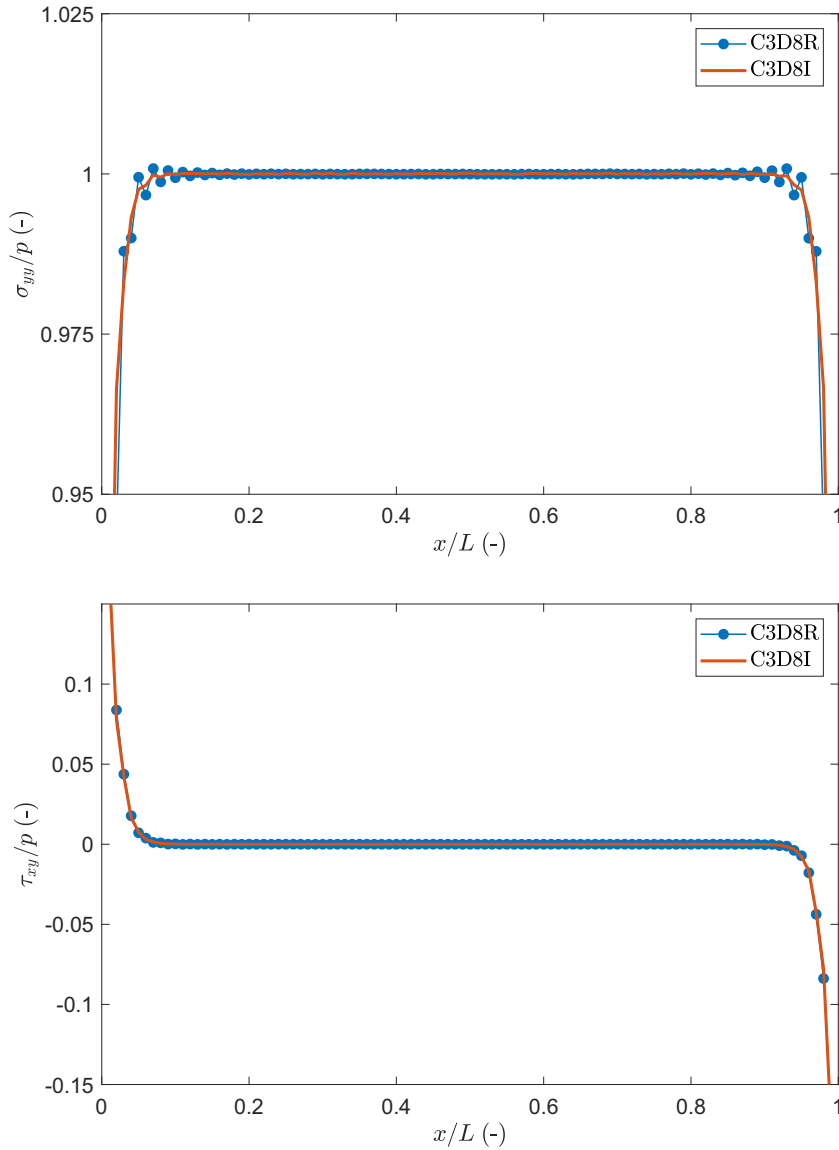


Figure A.1: Normalised normal (top) and tangential (bottom) stresses with respect to the applied pressure p as function of the dimensionless coordinate x/L . C3D8R: 8-node brick with reduced integration, C3D8I: 8-node brick with 8 points of integration and incompatible modes.

Appendix B

Details of third-body friction simulations

Discrete element contact model

The elastic contact of two solids of revolution is described by the Hertz theory, which predicts a circular contact area of radius a , given by [28]:

$$a = \left(\frac{3 F_n R_{eq}}{4 E_{eq}} \right)^{1/3}$$

where F_n is the normal force between the bodies. The corresponding normal displacement and maximum pressure are, respectively [28]:

$$\delta_n = \frac{a^2}{R_{eq}} = \left(\frac{9 F_n^2}{16 R_{eq} E_{eq}^2} \right)^{1/3}$$
$$p_{max} = \frac{3}{2} \frac{F_n}{\pi a^2} = \left(\frac{6 F_n E_{eq}^2}{\pi^3 R_{eq}^2} \right)^{1/3}$$

The relation between the normal force and the normal displacement used in the DEM code, is defined by the normal contact stiffness k_n , which can be easily derived by writing F_n as function of δ_n :

$$k_n = \frac{4}{3} E_{eq} \sqrt{R_{eq} \delta_n}$$

Similarly, the tangential contact stiffness k_t , which describes the relation between the tangential force F_t and the tangential displacement δ_t , is given by [21]:

$$k_t = 8 G_{eq} \sqrt{R_{eq} \delta_t}$$

The dissipative part of the interaction forces is determined by the normal and tangential damping coefficients, respectively given by [42]:

$$\gamma_n = \frac{\ln e}{\sqrt{\ln^2 e + \pi^2}} \sqrt{5 k_n m_{eq}}$$

$$\gamma_t = \frac{\ln e}{\sqrt{\ln^2 e + \pi^2}} \sqrt{\frac{10}{3} k_t m_{eq}}$$

Finally, the equivalent radius, mass and elastic moduli of two contacting bodies i and j are, respectively [21,28]:

$$R_{eq} = \left(\frac{1}{R_i} + \frac{1}{R_j} \right)^{-1}$$

$$m_{eq} = \left(\frac{1}{m_i} + \frac{1}{m_j} \right)^{-1}$$

$$E_{eq} = \left(\frac{1 - \nu_i^2}{E_i} + \frac{1 - \nu_j^2}{E_j} \right)^{-1}$$

$$G_{eq} = \left(\frac{1 - \nu_i}{G_i} + \frac{1 - \nu_j}{G_j} \right)^{-1}$$

3D computational domain

The walls are imported into the DEM environment as STL (Standard Triangulation Language) geometries created in an external CAD (Computer Aided Design) software. Since the DEM software is not able to deal with

walls moving across periodic boundary conditions, we model the 3D computational domain with an annular shear cell.

The external normal pressure p_a is generated by applying a constant force on the upper surface in the $-y$ direction. During the sliding phase, the lower surface is with a constant angular velocity ω along the $+y$ axis. The corresponding sliding velocity v is given by:

$$v = \omega r_m = \frac{2\pi}{T_{rot}} r_m$$

being T_{rot} the period of rotation and r_m the mean radius of the annulus.

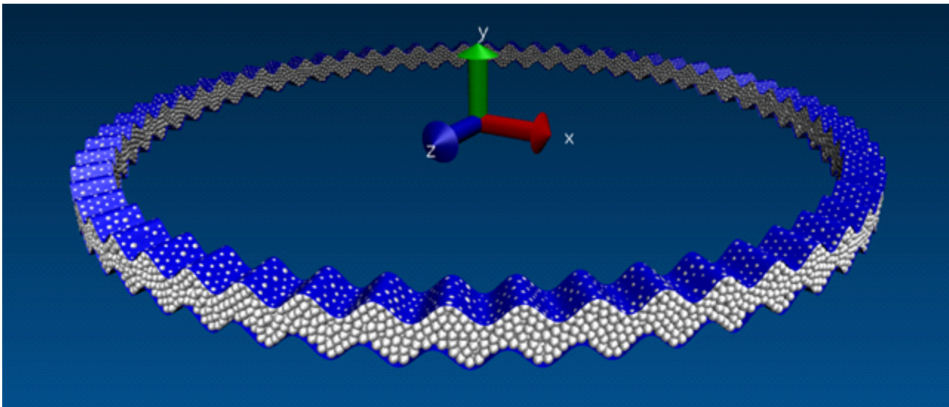


Figure B.1: Annular shear cell used for the 3D DEM simulations and coordinate reference system.

The frictional force $F_t(t)$ is thus obtained by monitoring the torque along the y axis $T_y(t)$, i.e.:

$$F_t(t) = \frac{T_y(t)}{r_m}$$

and the tangential stress is computed as:

$$\tau(t) = \frac{F_t(t)}{\pi(r_e^2 - r_i^2)}$$

with r_e and r_i the external and internal radii, respectively. With this formulation, we are assuming that the shear stress varies linearly in the radial direction, at least in the region $r_i < r < r_e$. Since we have employed very large r_e and r_i (57.5 and 62.5 in units of l_{ref} , respectively), we believe this assumption represents a good approximation. In fact, considering $l_{\text{ref}} = 1.0$ mm, it is roughly the same approximation adopted in the experimental work by Yu and Tichy [37] and in commercial annular shear testers.

Frequency-domain analysis

The periodicity shown by the function $\tau(t)$ is examined by means of a frequency-domain analysis of the signal. We perform a Discrete Fourier Transform (DFT) of $\tau(t)$ by using a Fast Fourier Transform (FFT) algorithm.

We find a first characteristic frequency f_1 nearly independent on the amplitude, but function of the sliding velocity and the wavelength through:

$$f_1 \approx \frac{v}{2\lambda}$$

which is observed more clearly for the largest wavelengths. With increasing amplitude, the energy associated to the high-frequency components of the signal increases as well, thus reflecting an increased particle motion, i.e. a higher total kinetic energy.

Effect of microscale contact parameters

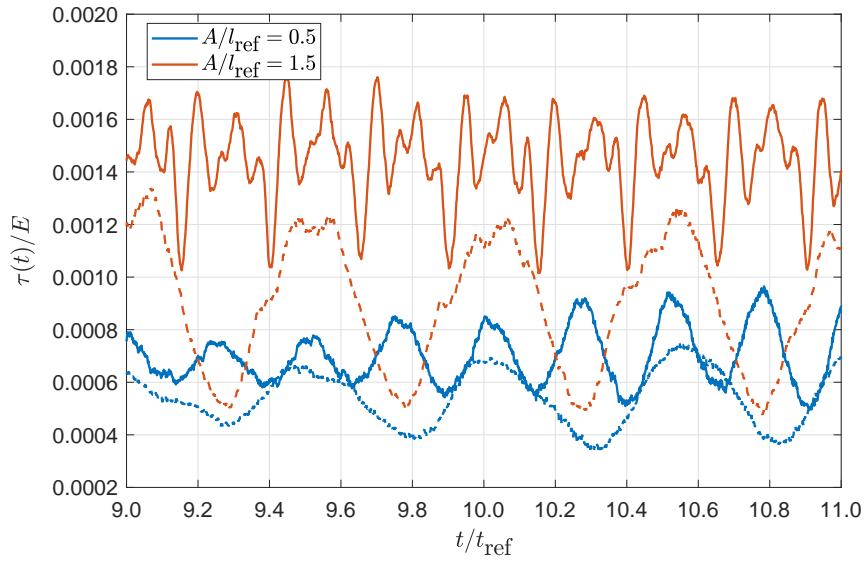


Figure B.2: Time evolution of the tangential stress for two simulation cases with different surface amplitudes ($D/l_{\text{ref}} = 2$, $p_a/E = 0.01$, $v/v_{\text{ref}} = 50$, $e = 0.5$, $\mu_m = 0.1$, $\mu_r = 0.0$), small c , $\lambda/l_{\text{ref}} = 4\pi$ (solid lines) and $\lambda/l_{\text{ref}} = 8\pi$ (dashed lines).

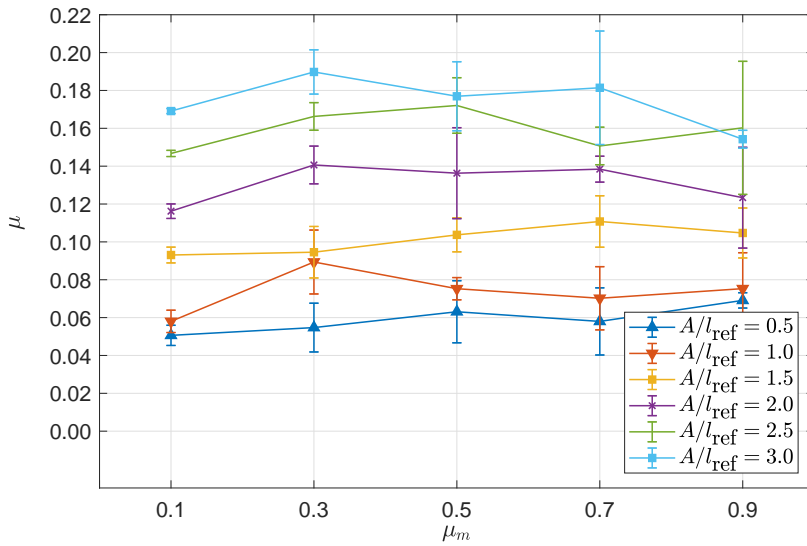


Figure B.3: Global coefficient of friction as function of the local coefficient of friction and the surface amplitude, for the reference simulation case ($D/l_{\text{ref}} = 2$, $p_a/E = 0.01$, $v/v_{\text{ref}} = 5$, $e = 0.5$, $\mu_r = 0.0$), small c and $\lambda/l_{\text{ref}} = 6\pi$.

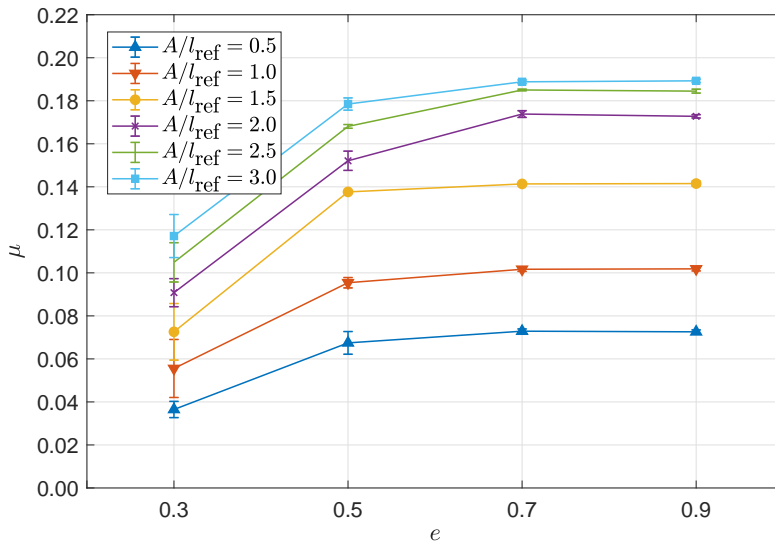


Figure B.4: Global coefficient of friction as function of the coefficient of restitution and the surface amplitude, for the reference simulation case ($D/l_{\text{ref}} = 2$, $p_a/E = 0.01$, $v/v_{\text{ref}} = 5$, $e = 0.5$, $\mu_r = 0.0$), small c and $\lambda/l_{\text{ref}} = 4\pi$.

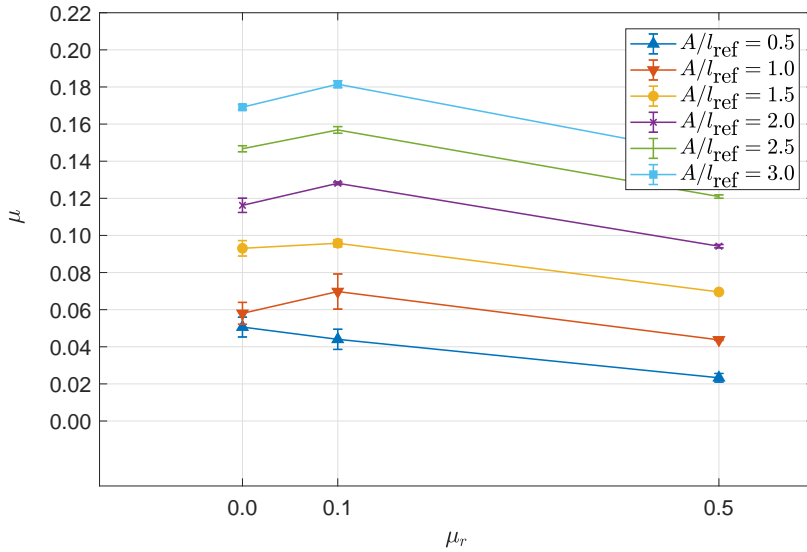


Figure B.5: Global coefficient of friction as function of the coefficient of rolling friction and the surface amplitude, for the reference simulation case ($D/l_{\text{ref}} = 2$, $p_a/E = 0.01$, $v/v_{\text{ref}} = 5$, $e = 0.5$, $\mu_r = 0.0$), small c and $\lambda/l_{\text{ref}} = 6\pi$.

Appendix C

Details of penetration mechanics simulations

Discrete element simulation details

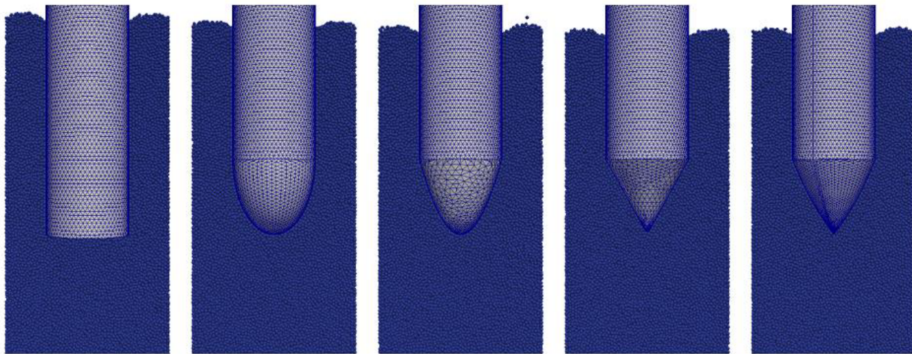


Figure C.1: Simulated probe geometries immersed in the granular packing. From left to right: cylindrical, elliptical, parabolic, conical and root-like probe.

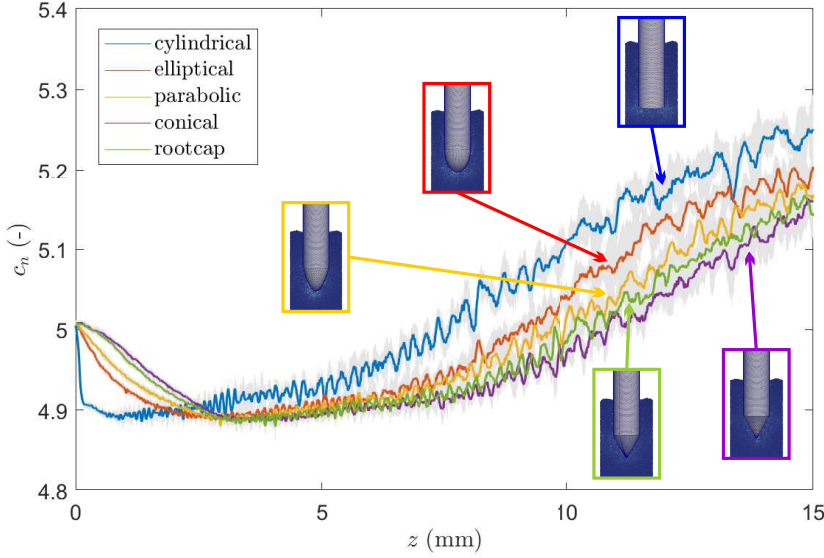


Figure C.2: Contact number curves of five different probes from numerical simulations. The diameter of the tested probes is equal to 3 mm and the maximum reached penetration depth is 15 mm at 10 mm/s speed. The lines refer to the average values of five random simulations, the shaded areas to the standard deviations.

Effective penetration depth

The force-displacement curves obtained through the numerical simulations must be corrected in order to take into account the effective penetration depth of the probe. The presence of the lateral walls, in fact, has the effect of a progressive increase in the height of the particle packing, since particles are displaced from the volume occupied by the probe during penetration.

The volume occupied by the probe V_p changes as function of time as:

$$V_p(t) = \begin{cases} \chi \pi R_p^2 vt & vt \leq H_p \\ \pi R_p^2 vt + \pi R_p^2 H_p (\chi - 1) & vt > H_p \end{cases}$$

Property	Value
sand density	2000 kg/m ³
sand Young's modulus	10 MPa
sand Poisson's ratio	0.3
probe Young's modulus	1 GPa
probe Poisson's ratio	0.3
sand-sand coefficient of friction	0.5
sand-probe coefficient of friction	0.5
sand-sand coefficient of restitution	0.8
sand-probe coefficient of restitution	0.8
particle diameter	0.125 mm
number of particles	40000
penetration velocity	10 mm/s
time step	1 · 10 ⁻⁶ s

Table C.1: Material properties and main discrete-element simulation settings.

where R_p is the probe radius, H_p the tip height and v the penetration speed. χ is a shape factor depending on the probe geometry, i.e.:

$$\chi = \frac{1}{H_p R_p^2} \int_0^{H_p} (f^{-1}(y))^2 dy$$

and $1/3 \leq \chi \leq 1$ with the lowest limit corresponding to the conical probe (i.e., minimum tip volume) and $\chi = 1$ to the cylindrical probe (i.e., maximum tip volume).

If R is the container radius and H the height of the particle packing, its variation during the penetration process is given by:

$$\pi(R^2 - R_p^2) \cdot \Delta H(t) \approx V_p(t)$$

Therefore, the probe displacement $z(t) = vt$ can be corrected by adding $\Delta H(t)$, obtaining the following expression for the effective probe displace-

ment:

$$z_{eff}(t) = \begin{cases} vt \left(1 + \frac{R_p^2}{R^2 - R_p^2} \chi\right) & vt \leq H_p \\ vt + \frac{R_p^2}{R^2 - R_p^2} [vt + H_p(\chi - 1)] & vt > H_p \end{cases}$$

Note that in the case of the experimental tests, the proposed displacement correction is negligible since $R_p/R \ll 1$.

The rescaling of the penetration depth according to the expression above produces lower values of the penetration force. This effect could be compensated by the assumed values for some microscale parameters of the DEM simulations (e.g., the coefficients of friction and of restitution listed in Table C.1), which can be tuned to match precisely the experiments. Since the order relations among the different tip shapes is preserved, here we have considered the nominal penetration depth without the rescaling above derived.

Appendix D

Details of spider's hair properties

SEM morphology

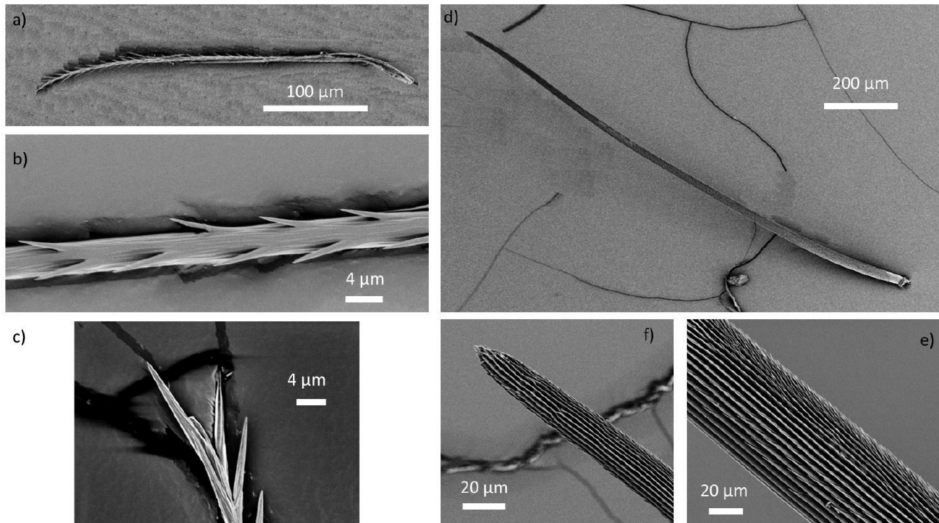


Figure D.1: SEM morphology of different hairs collected on the *Theraphosa stirmi*'s exoskeleton.

Mechanical properties

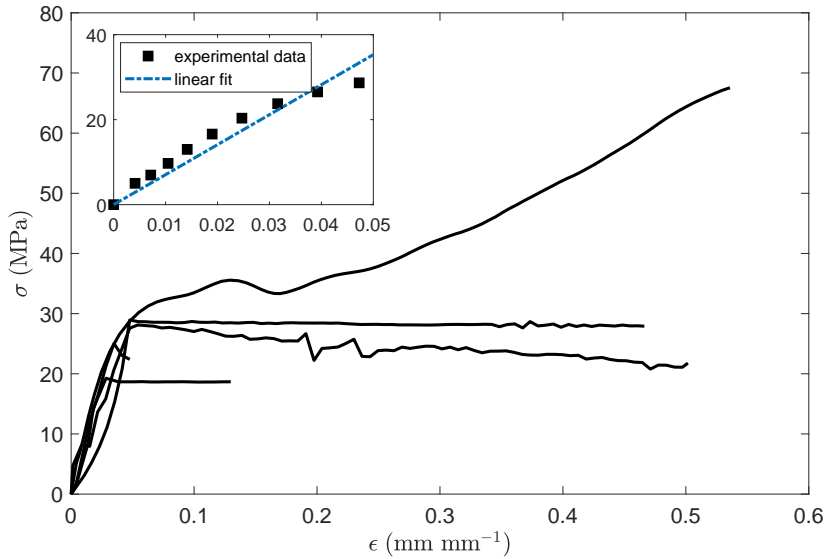


Figure D.2: Example stress-strain curves of different *Theraphosa stirmi*'s hairs obtained through nanotensile tests. Inset: Example linear fit on the first part of a curve, with extracted Young's modulus $E \approx 705.8$ MPa (R2-value 0.921).

Appendix E

Carbon-based coatings for industrial power transmission applications

Introduction

In a vision of reductions of volumes and weights, and thus of performance improvement, recent design concepts in industrial power transmission systems are considering the replacement of bearing elements with sliding contacts with high wear resistance and improved frictional and mechanical stability. Therefore, one solution is the use of carbon-based thin-film coatings for the optimal tribological performance of the new steel sliding components. In particular, diamond-like carbon coatings are known for their enhanced wear resistance and tribological behaviour.

The objective of this study is the morphological, tribological and mechanical characterization of these carbon-based coatings.

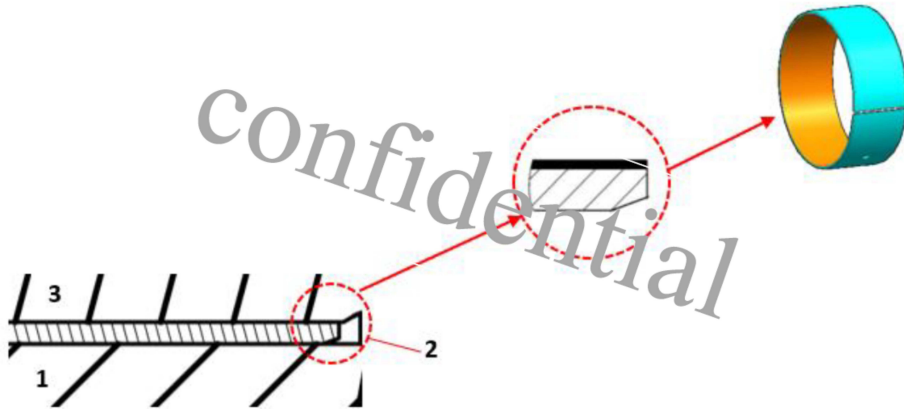


Figure E.1: Design concept of a new sliding contact for industrial power transmission systems: 1) rotating element, 2) sliding contact and 3) fixed element. Courtesy of Bonfiglioli Riduttori SpA.

Description of the samples

Cylindric samples of diameter 20 mm and height 5 mm have been coated through Physical Vapour Deposition (PVD) by Oerlikon Balzers Coating Italy SpA. The base material is a 88MnV8 steel and four different carbon-based coatings have been realised, i.e.:

- a tungsten-doped carbon-based coating with a hardness of about 1500 HV (C1500);
- a "very low temperature" W-doped carbon-based coating (C2VLT), obtained with a coating treatment below 200 °C;
- a tungsten-doped carbon-based coating (CSTAR);
- a diamond-like carbon with an additional CrN substrate (DLCS), made of a hydrogenated amorphous carbon structure (a-C:H).

The tungsten doping leads to the formation of related carbides (WC), which are then present in the lamellar microstructure of the C1500, C2VLT and CSTAR coatings. In the case of CSTAR and DLCS coatings, the additional CrN layer is interposed between the base material and the coating in order to improve the adhesion of the carbon-based coating and thus the strength of the interface.



Figure E.2: Tested uncoated and coated samples. From left to right: uncoated, C1500, C2VLT, CSTAR and DLCS coatings.

Optical microscopy

The samples were cut in two halves and incorporated in an acrylic resin and polished. An etching with a Nital 3% solution was carried out in order to prepare the surfaces for the metallography study. The optical microscopy

was carried out with a ZEISS Imager A1m (Carl Zeiss AG, Germany), and the thickness of the coatings was measured.

In the cross section of the samples, the martensitic structure (presenting globular carbides) of the base steel clearly visible.

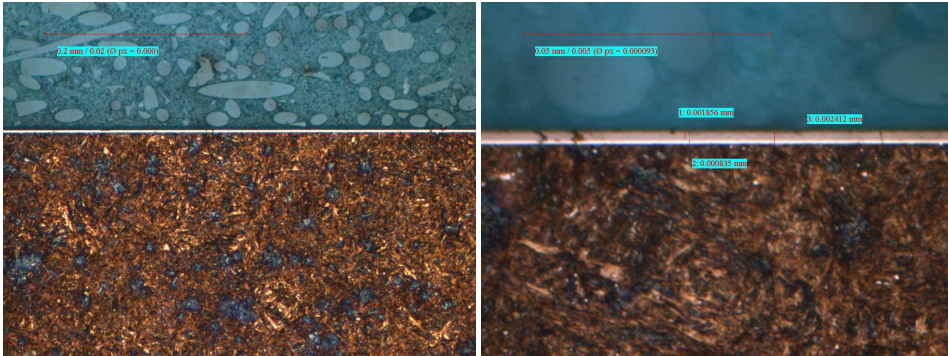


Figure E.3: Optical microscopy of the cross section of the C1500-coated steel sample: 200x (left) and 1000x (right) image.

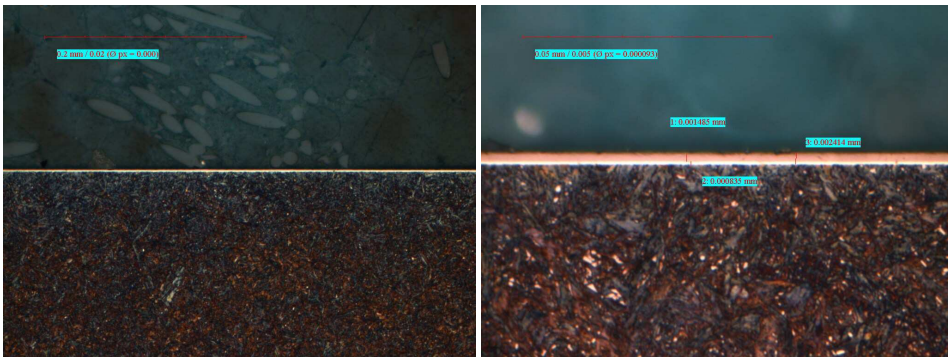


Figure E.4: Optical microscopy of the cross section of the C2VLT-coated steel sample: 200x (left) and 1000x (right) image.

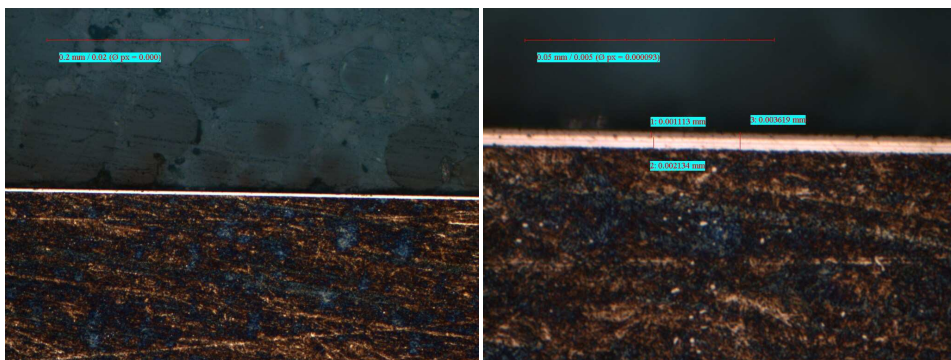


Figure E.5: Optical microscopy of the cross section of the CSTAR-coated steel sample: 200x (left) and 1000x (right) image.

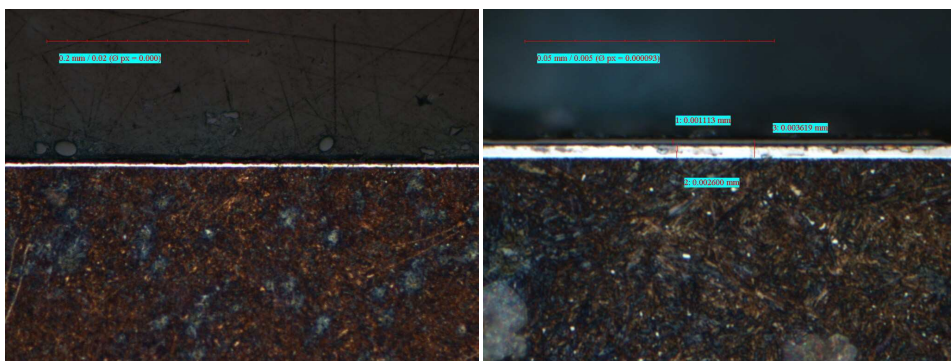


Figure E.6: Optical microscopy of the cross section of the DLCS-coated steel sample: 200x (left) and 1000x (right) image.

Tribometer tests

The tribological characterisation of the coatings was performed with a CSM Instruments standard tribometer 0 – 60 N (Anton Paar GmbH, Austria), in a ball-on-disk configuration. We carried out friction coefficient measurements at four different sliding speeds (i.e., from 5 to 20 cm s⁻¹) and at a single applied normal load (i.e., 0.5 N), with a 30 Hz data acquisition rate.

Each test was interrupted after a total sliding distance of 20 m was reached. The tests were performed in air at about 24 °C, and the surface were cleaned with ethanol before sliding. The ball, with a 6 mm diameter, was made of 100Cr6 steel.

The choice of a small load was due to the need of reducing the ball wear, while the wear of the coatings resulted negligible even with preliminary tests at higher loads, with an almost absent wear track. Therefore, we do not discuss here the wear properties of the coatings, but some indications are available in the literature.

The raw data are smoothed through a Savitzky-Golay filter with decreasing span for an increasing sliding speed (i.e., 30 for 5 cm s⁻¹, 20 for 10 cm s⁻¹, 10 for 15 cm s⁻¹, 5 for 20 cm s⁻¹) and degree 1.

The DLCS coating presents the smallest values of friction coefficient, in agreement with those found in the literature. Also in this case, the dependence on the sliding speed is not clear and it is almost independent.

Nanoindentation tests

Nanoindentation tests were performed through an iNano nanoindenter (Nanomechanics Inc, United States of America), using a Berkovich indenter and a 25 mN load. We performed a total of 20 indentations per sample, arranged in a rectangular array with 30 μm spacings.

The choice of the load allowed to reach always a maximum indentation depth of approximately 0.3 μm, thus around the 10% of the total layer thickness. This allowed to extract solely the mechanical properties of the layer, thus neglecting the influence of the base material.

Coating	Sliding speed (cm s ⁻¹)	Friction coefficient (-)
uncoated	5	1.072 ± 0.049
	10	0.984 ± 0.019
	15	0.959 ± 0.028
	20	0.899 ± 0.073
C1500	5	0.143 ± 0.018
	10	0.154 ± 0.019
	15	0.127 ± 0.021
	20	0.111 ± 0.028
C2VLT	5	0.141 ± 0.029
	10	0.154 ± 0.034
	15	0.145 ± 0.027
	20	0.134 ± 0.021
CSTAR	5	0.156 ± 0.027
	10	0.127 ± 0.020
	15	0.112 ± 0.013
	20	0.110 ± 0.019
DLCS	5	0.101 ± 0.021
	10	0.059 ± 0.011
	15	0.065 ± 0.015
	20	0.069 ± 0.017

Table E.1: Measured friction coefficients (mean values and standard deviations, computed from 10 to 20 m sliding distance) of the uncoated sample and the coatings for the considered sliding speeds.

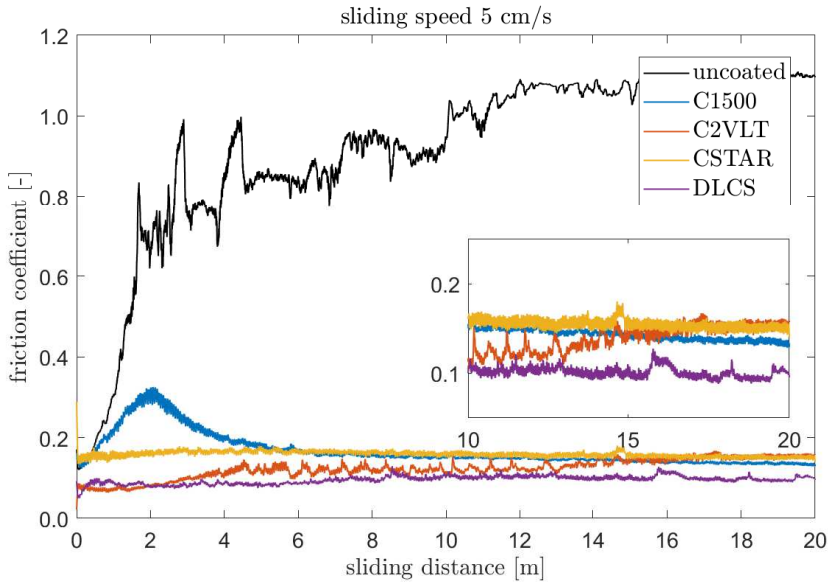


Figure E.7: Ball-on-disk tribometer test on the coated steel samples, with sliding speed 5 cm s^{-1} . Inset: details of the coated samples.

The hardness and the Young's modulus of the coatings are given by, respectively:

$$H = P_{max}/A$$

$$E_r = \frac{\sqrt{\pi}}{2} \frac{S}{\sqrt{A}}$$

where P_{max} is the maximum indentation load, A the projected contact area and $S = dP/dh$ the stiffness of the unloading load-indentation depth curve $P = P(h)$. E_r is the reduced Young's modulus, related to the couple of materials in contact through the following equation:

$$\frac{1}{E_r} = \frac{1 - \nu^2}{E} + \frac{1 - \nu_i^2}{E_i}$$

being E and ν the Young's modulus and the Poisson's ratio of the material and E_i and ν_i the same properties of the indenter.

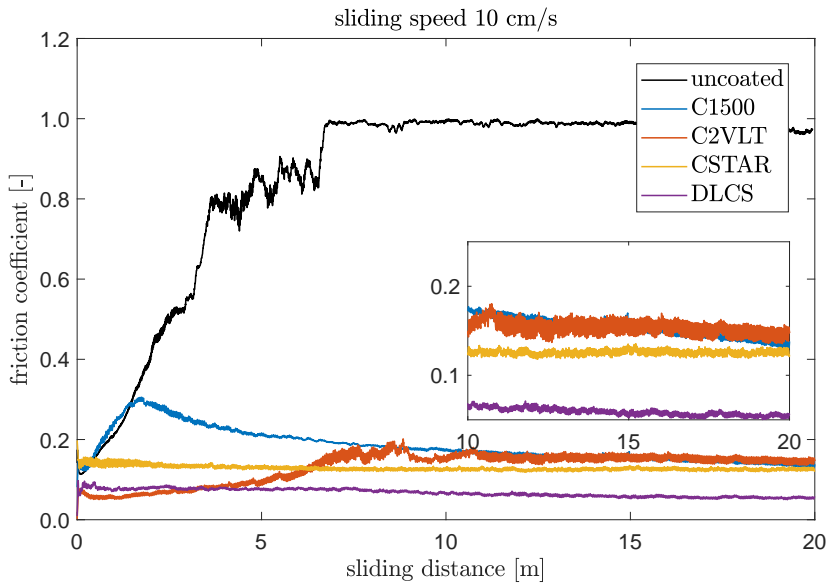


Figure E.8: Ball-on-disk tribometer test on the coated steel samples, with sliding speed 10 cm s^{-1} . Inset: details of the coated samples.

Discussion

Here we report some conclusions summarising the outputs of the optical microscopy activities, the tribometer tests and the nanoindentation tests discussed above.

- All the coatings present a good uniformity in thickness. The total thickness is below $3 \mu\text{m}$ for the C1500 and the C2VLT coatings, while it is about 50% larger for the CSTAR and the DLCS coatings, which present also a thicker bottom layer (probably corresponding to a CrN film, as suggested by the supplier).

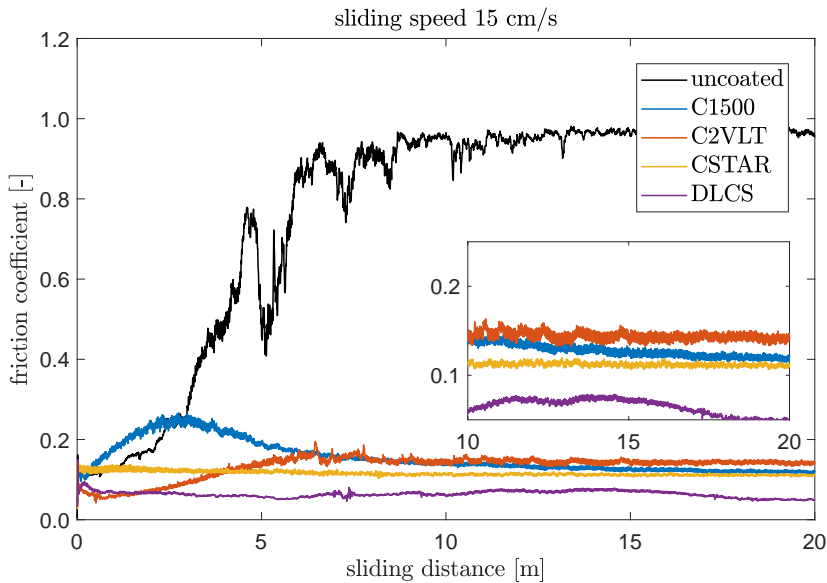


Figure E.9: Ball-on-disk tribometer test on the coated steel samples, with sliding speed 15 cm s^{-1} . Inset: details of the coated samples.

- Under standard ball-on-disk tribometer tests, all the coatings present a much smaller friction coefficient with respect to the uncoated material. The CSTAR and the DLCS coatings offer the best performance in terms of value of the friction coefficient and its stability with time. The DLCS coating presents a friction coefficient around or below 0.1 under various sliding speeds.
- The hardness measurements through nanoindentation tests show a much larger value for the DLCS coating, up to 25 GPa, while the other coatings present a hardness value below 15 GPa.

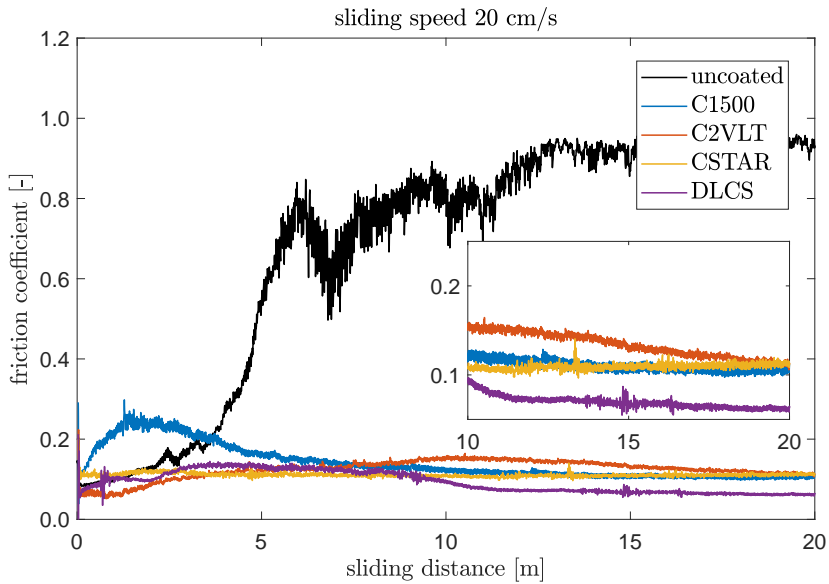


Figure E.10: Ball-on-disk tribometer test on the coated steel samples, with sliding speed 20 cm s^{-1} . Inset: details of the coated samples.

Coating	Maximum depth (μm)	Hardness (GPa)	Young's modulus (GPa)
uncoated	0.328 ± 0.006	9.00 ± 0.060	224.08 ± 8.39
C1500	0.318 ± 0.009	9.95 ± 1.52	122.50 ± 10.83
C2VLT	0.323 ± 0.013	9.16 ± 1.69	126.78 ± 14.06
CSTAR	0.301 ± 0.007	12.97 ± 2.10	142.00 ± 13.78
DLCS	0.244 ± 0.011	25.39 ± 5.66	234.36 ± 39.14

Table E.2: Results of the nanoindentation tests: measured hardness and Young's modulus of the coatings and maximum reached indentation depth.

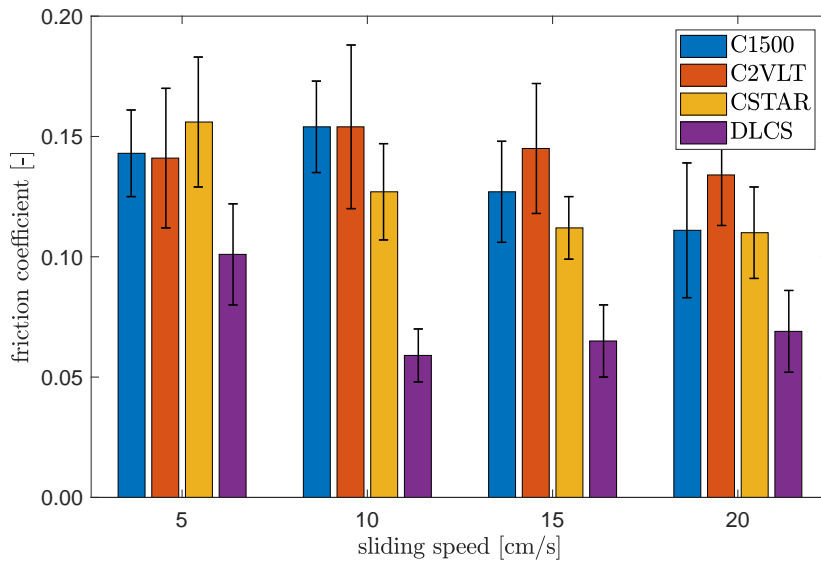


Figure E.11: Graphical representation of the velocity dependence of the friction coefficient of the coatings.

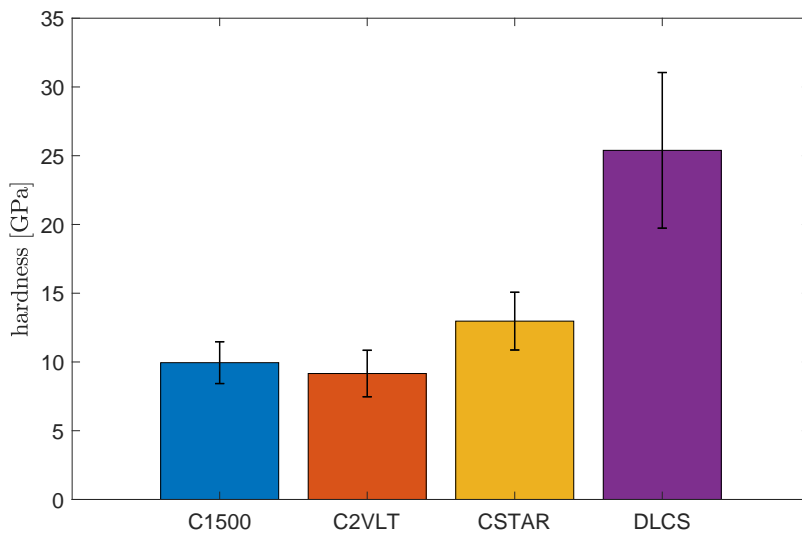


Figure E.12: Graphical representation of the hardness values of the coatings.